

SLURRY BASED STEREOLITHOGRAPHY: A SOLID
FREEFORM FABRICATION METHOD OF CERAMICS AND
COMPOSITES

By

Xuan Song

A Dissertation Presented to the
FACULTY OF THE USC GRADUATE SCHOOL
UNIVERSITY OF SOUTHERN CALIFORNIA
In Partial Fulfillment of the
Requirements for the Degree
DOCTOR OF PHILOSOPHY
(INDUSTRIAL AND SYSTEMS ENGINEERING)

August 2016

Acknowledgements

Since my first day as a PhD student on August 7th, 2011, I have continuously received help, guidance and support for my research from remarkable individuals at USC. As an interdisciplinary research project, this thesis includes the efforts of dozens of persons, whom I would like to thank sincerely.

First of all, I would like to express my deep appreciation and gratitude to Dr. Yong Chen for his advising on this research. Dr. Chen has continued to encourage and inspire me, all the way from when I was applying for his group, to the process of hunting for an academic job. Under Dr. Chen's supervision, I have obtained solid training in teaching, research as well as communication. I am truly fortunate to have had the opportunity to work with him.

I would also like to thank Dr. Berok Khoshnevis for his invaluable assistance and suggestion on my research. It is his initiative and passion in research that believes me in how a researcher can make a meaningful difference to human life. Many thanks go to Dr. Satyandra Kumar Gupta for serving on my thesis committee, to Dr. Qiang Huang, Dr. Qifa Zhou and Dr. Néstor Pérez-Arancibia for serving on my qualifying committee.

Next I'd like to recognize Zeyu Chen, Dr. Yang Yang, Dr. Liwen Lei, Dr. Shanghua Wu, Dr. Kirk Shung, Dr. Steven Nutt, Dr. Will Pannell and Dr. Jay R. Lieberman for the contributions that each of them made to the completion of this work. Special thanks go to Zeyu Chen who has worked with me on fabricating ultrasound transducers using slurry-based stereolithography method (Chapter 5); to Dr. Yang Yang who provided me with the knowledge on advanced materials and helped with the fabrication of high dielectric capacitors (Chapter 4); to Dr. Liwen Lei and Dr. Shanghua Wu for offering generous help and patient guidance in post processing of ceramics; to Dr. Kirk Shung and Dr. Steven Nutt for providing us with

instruments for material preparation and characterization; to Dr. Will Pannell and Dr. Jay R. Lieberman for helping us extend the work to medical research (not included in this thesis).

I am grateful for an opportunity of working at Futurewei as an intern in Summer 2015 under the mentoring of Dr. Jiafeng Zhu and Dr. Masood Mortazavi. They provided me with all the resources that I needed for a robot project and taught me about teamwork and collaboration, which I think will benefit me for the rest of my life.

Others at USC to whom I am grateful are to my lab mates at the additive manufacturing lab: Dr. Chi Zhou, Dr. Yayue Pan, Dr. Yongqiang Li, Dr. Kai Xu, Dr. Jing Zhang, Dongping Deng, Xiao Yuan, Pu Huang, Dr. Matthew Petros, Payman Torabi, Behnam Zahiri, Aref Vali, Amir Mann, Dr. Tsz Ho Kwok, Xiang Gao, Huachao Mao, Xiangjia Li and Jie Jin for sharing many brilliant research ideas and experience with me which have contributed to my intellectual growth.

My gratitude extends to the undergraduate and graduate students who worked with me during the past five years for their enthusiasm and willingness to develop new additive manufacturing processes: Xuan Zheng, Zhuofeng Zhang, Pin-I Wu, Reese Dorrepaal, Kennedy Stine, Tae Woo Lee, Zaid Badwan, Kalline Tong, Andrew Davidson, Gonzalo Gambino, etc. They are extremely helpful in the creation of the prototype systems and basic experiments in this thesis.

This dissertation would not have been possible without funding from the Epstein department of industrial and systems engineering at USC and the National Science Foundation (NSF-CMMI 1335476). Their generous financial support is greatly appreciated.

Finally, I especially thank my wife Mrs. Yiqing Zhu, my parents, my parents-in-law, my sister, my beloved pets and all the other family members in China for their constant support and unconditional love. They have been always sticking by my side whenever I encountered difficulty in the research. It would have been impossible for me to complete what I started without their love and faith in me.

Table of Contents

| | |
|---------------------------------------------------------------------------------------------------|-----|
| Acknowledgements | i |
| List of Tables..... | vi |
| List of Figures | vii |
| Abstract | i |
| Chapter 1 Introduction | 1 |
| 1.1 Additive manufacturing and its material selection..... | 1 |
| 1.2 Ceramic and composite materials..... | 4 |
| 1.3 Stereolithography | 8 |
| 1.4 Problem Formulation..... | 12 |
| 1.4.1 High viscosity..... | 13 |
| 1.4.2 Slurry homogeneity | 15 |
| 1.4.3 Low photosensitivity | 16 |
| 1.4.4 Post processing..... | 17 |
| 1.5 Research Questions, Hypotheses and Contributions | 18 |
| 1.6 Outline of this work..... | 23 |
| Chapter 2 Literature Review: Additive Manufacturing from a material selection perspective..... | 25 |
| 2.1 Composite Fabrication | 25 |
| 2.1.1 Indirect methods..... | 26 |

| | |
|-------------------------------------------------------------------------------------|----|
| 2.1.2 Fused Deposition of Composite (FDC)..... | 27 |
| 2.1.3 Direct Ink Write | 28 |
| 2.1.4 Stereolithography | 31 |
| 2.1.5 Binder/Ink Jetting..... | 33 |
| 2.1.6 Selective Laser Sintering..... | 34 |
| 2.1.7 Laminated Object Manufacturing | 34 |
| 2.2 Ceramic Fabrication | 35 |
| 2.2.1 Extrusion Freeform Fabrication | 35 |
| 2.2.2 Stereolithography | 37 |
| 2.2.3 Binder/Ink Jetting..... | 39 |
| 2.2.4 SLS/SLM..... | 40 |
| 2.2.5 Slurry-layer casting | 42 |
| 2.2.6 LOM..... | 43 |
| 2.2.7 Electrophotographic Printing | 43 |
| 2.3 Summary | 45 |
| Chapter 3 Slurry-based SLA: Fabrication of Polymer-based Composites..... | 46 |
| 3.1 Ceramic composite slurry formulation..... | 46 |
| 3.2 Curing characteristics..... | 48 |
| 3.3 Rheological characteristics..... | 51 |
| 3.4 Bottom-up projection for Stereolithography | 56 |
| 3.5 Tape-casting integrated with Bottom-up Projection based Stereolithography | 57 |

| | |
|--------------------------------------------------------------------------------------|----|
| 3.6 Prototype Design and Process Planning..... | 61 |
| 3.7 Summary | 64 |
| Chapter 4 Process Modeling: Parameter Optimization for Slurry-based SLA process..... | 66 |
| 4.1 Overview | 66 |
| 4.2 Layer recoating via tape casting..... | 66 |
| 4.2.1 Blade height δ_{Blade} | 66 |
| 4.2.2 Recoating speed v_r | 69 |
| 4.2.3 Layer Pressing Speed v_p | 70 |
| 4.3 Layer separation via sliding mechanism | 73 |
| 4.4 Base layers for initial gap compensation..... | 74 |
| 4.5 Material Feeding | 75 |
| 4.5.1 Moving distance of dispenser and its plunger | 75 |
| 4.5.2 Nozzle height..... | 76 |
| 4.6 Case Study I: fabrication of glass reinforced composite components..... | 77 |
| 4.7 Case Study II: fabrication of high dielectric capacitor..... | 79 |
| 4.7.1 Starting Materials | 79 |
| 4.7.2 Results and Discussion..... | 81 |
| 4.8 Summary | 86 |
| Chapter 5 Post Processing for Ceramic Component Fabrication..... | 88 |
| 5.1 Overview | 88 |
| 5.2 Case Study I: Traditional Ceramics for Structural Purpose | 90 |

| | |
|-----------------------------------------------------------------------|-----|
| 5.2.1 Green Part Fabrication..... | 90 |
| 5.2.2 Post Processing..... | 91 |
| 5.2.3 Testing Results of Sintered Samples | 93 |
| 5.3 Case Study II: Piezoelectric Ceramics for Ultrasound Imaging..... | 95 |
| 5.3.1 Introduction to Ultrasound Transducer | 95 |
| 5.3.2 Related Work..... | 96 |
| 5.3.3 Green Part Fabrication..... | 99 |
| 5.3.4 Post Processing of BTO Green Parts..... | 102 |
| 5.3.5 Testing Results of Sintered Samples | 105 |
| 5.4 Summary | 115 |
| Chapter 6 Post Processing for Porous Structure Fabrication..... | 116 |
| 6.1 Introduction | 116 |
| 6.2 Process description..... | 118 |
| 6.3 Main process parameters | 120 |
| 6.4 Sugar removal | 123 |
| 6.5 Test cases..... | 127 |
| 6.5 Summary | 130 |
| Chapter 7 Conclusions and recommendations | 132 |
| 7.1 Answering the Research Questions and Testing Hypothesis | 132 |
| 7.2 Contributions and Intellectual Merit | 134 |
| 7.3 Recommendations for Future Work | 135 |

Reference..... 137

List of Tables

| | |
|--------------------------------------------------------------------------------------------------|-----|
| Table 1.1 AM process classification based on the form of the starting material | 3 |
| Table 1.2 AM process classification based on the type of the starting material | 4 |
| Table 1.3 Examples of Applications of Piezoelectric Ceramics | 5 |
| Table 1.4 Information of EnvisionTec SI500 on ingredients..... | 9 |
| Table 3.1 Physical properties and cure depths of ceramic powders with 65wt% | 49 |
| Table 4.1 Process parameters used in the fabrication process for glass reinforced composite..... | 77 |
| Table 5.1 Process parameters used in the fabrication process for alumina composite | 90 |
| Table 5.2 Parameters used in the fabrication process for piezoelectric composites | 101 |
| Table 5.3 Measured properties of BTO samples fabricated by our process | 107 |
| Table 6.1 Slurry coating with different blade height and solid loadings | 121 |
| Table 6.2 Sample weight changes after boiling | 126 |

List of Figures

| | |
|----------------------------------------------------------------------------------------------------------|----|
| Figure 1.1 Basic principle of additive manufacturing processes..... | 2 |
| Figure 1.2 Applications of Additive Manufacturing..... | 3 |
| Figure 1.3 Traditional Processing Method of Ceramics..... | 6 |
| Figure 1.4 Photopolymerization of a generalized methacrylate monomer..... | 9 |
| Figure 1.5 (a) Laser based SLA (b) Mask image projection based SLA | 10 |
| Figure 1.6 Resin Over-cure in SLA processes | 10 |
| Figure 1.7 Two recoating processes for the top-down projection method..... | 14 |
| Figure 1.8 Deformation of green parts fabricated from diluted slurry after drying | 14 |
| Figure 1.9 Effects of slurry homogeneity..... | 15 |
| Figure 1.10 Light scattering by solid particles in liquid resin..... | 17 |
| Figure 1.11 Related chapters to research questions and hypotheses | 22 |
| Figure 1.12 Overview of the dissertation | 24 |
| Figure 2.1 Schematic of the 3D printer head to produce continuous carbon fiber reinforced composites ... | 28 |
| Figure 2.2 Schematic illustration of extruding fiber reinforced suspension via a nozzle system | 30 |
| Figure 2.3 Lithoz's digital light processing system for photosensitive ceramic slurries | 38 |
| Figure 2.4 Schematic of an electrophotographic printing system | 44 |
| Figure 3.1 Preparation of ceramic composite slurry | 48 |

| | |
|---------------------------------------------------------------------------------------------------------|----|
| Figure 3.2 Viscosity of alumina slurries with different concentrations of dilute solvent | 52 |
| Figure 3.3 Viscosity of alumina slurries with different solid loadings | 52 |
| Figure 3.4 As-cast slurry tapes with different solid loadings, doctor blade height is 200 μ m | 53 |
| Figure 3.5 Projection-based SLA process using the bottom-up projection method..... | 56 |
| Figure 3.6 (a) Schematic of typical tape caster (b) An automatic tape casting coater | 58 |
| Figure 3.7 Green part fabrication using tape casting integrated SLA | 60 |
| Figure 3.8 Process planning for the tape casting integrated SLA process | 60 |
| Figure 3.9 Fabrication machine of projection-based SLA integrated with tape casting | 61 |
| Figure 3.10 A prototype system using the tape casting integrated SLA process | 62 |
| Figure 3.11 Flow chart of the tape-casting-integrated SLA process | 63 |
| Figure 4.1 Tape casting techniques (a) traditional process (b) used in our process | 67 |
| Figure 4.2 The velocity profile in the blade recoating | 68 |
| Figure 4.3 PDMS deformation leads to bigger recoated thickness | 70 |
| Figure 4.4 Measurement of recoated thickness | 72 |
| Figure 4.5 Actual layer thickness versus pressing speed | 72 |
| Figure 4.6 Drag force during the layer detachment..... | 73 |
| Figure 4.7 Parameters in the dispensing system..... | 76 |
| Figure 4.8 A “Hand” model fabricated with glass reinforced composite..... | 78 |
| Figure 4.9 A “Beethoven” model fabricated with glass reinforced composite | 78 |
| Figure 4.10 Scheme of the preparation process of the PZT@Ag nanoassemblies..... | 80 |
| Figure 4.11 Fabricated capacitors | 82 |

| | |
|----------------------------------------------------------------------------------------------------------|-----|
| Figure 4.12 Fabricated capacitors (a) Star structure (b) Bowl structure | 83 |
| Figure 4.13 (a) Dielectric permittivity (b) Loss tangent of composite film | 84 |
| Figure 4.14 Electrochemical measurements for the as-printed capacitors | 85 |
| Figure 5.1 Different methods of bonding ceramic powders in additive manufacturing | 88 |
| Figure 5.2 Schematic of Post Processing for Ceramic Component Fabrication | 89 |
| Figure 5.3 Alumina Green Parts fabricated by the tape-casting-integrated SLA process | 91 |
| Figure 5.4 Post processing of Alumina green parts. (a) De-binding schedule; (b) sintering schedule | 92 |
| Figure 5.5 A test case of a gear model | 93 |
| Figure 5.6 The SEM images of different samples. (a) Alumina green part; (b) sintered Alumina part..... | 94 |
| Figure 5.7 An illustration of ultrasound transducers in an ultrasound system | 96 |
| Figure 5.8 A comparison of piezoelectric component fabrication based on machining and AM processes. | 97 |
| Figure 5.9 Curing characteristic of BTO slurry with varying BTO weight ratios | 100 |
| Figure 5.10 Fabrication result of a 0-3 PZT composite ultrasound transducer array | 101 |
| Figure 5.11 Concave BTO element fabricated by our process..... | 101 |
| Figure 5.12 A 64 element BTO segment annular array fabricated by our process | 102 |
| Figure 5.13 Temperature schedules for debinding and sintering of BTO green parts | 103 |
| Figure 5.14 The concave transducer element: (a) green part; (b)(c) after sintering..... | 104 |
| Figure 5.15 The segment annular transducer array: (a) greenpart ; and (b) after sintering..... | 105 |
| Figure 5.16 Scanning electron microscope images: (a) after debinding; (b) after sintering | 106 |
| Figure 5.17 The X-Ray diffractometer patterns of BTO powders and sintered samples | 107 |
| Figure 5.18 Property measurement of samples sintered at different temperature | 109 |

| | |
|----------------------------------------------------------------------------------------------------|-----|
| Figure 5.19 Polarization–electric field hysteresis loop of sintered BTO samples | 110 |
| Figure 5.20 Application of a BTO sample in an ultrasound transducer..... | 111 |
| Figure 5.21 Initial pulse and echo generated by the printed focused transducer | 111 |
| Figure 5.22 (a) Echo signal; (b) Voltage and lateral resolution of the fabricated transducer | 113 |
| Figure 5.23 Ultrasonic imaging of porcine eyeball..... | 114 |
| Figure 6.1 Applications of various foam structures | 118 |
| Figure 6.2 Schematics of the dynamic sugar templating method based on slurry-based SLA | 119 |
| Figure 6.3 Cure depth with different cure time for different solid loadings | 122 |
| Figure 6.4 Cylinder shell structures with different thickness..... | 124 |
| Figure 6.5 Different support patterns for thin features..... | 125 |
| Figure 6.6 Microscope image after sugar removal..... | 126 |
| Figure 6.7 Increase porosity by the sugar foaming method | 129 |
| Figure 6.8 Glass composite foam structure fabrication by the slurry-based SLA..... | 130 |

Abstract

During the past thirty years, manufacturing community has benefitted from additive manufacturing (AM) technologies, thanks to many of its advantages including the capability of fabricating components directly from three dimensional (3D) computer-aided design (CAD) models. However, although it can build any complex geometry with a relatively rapid speed, its widespread adoption in manufacturing industry is substantially restricted by its limited material selection. Efforts have been made to fabricate advanced materials, such as composites and ceramics, with various AM processes, among which projection-based stereolithography (SLA) process has advantages of faster speed and higher accuracy over the other ones. In an SLA process for composite materials, a slurry mixture of solid filler and photosensitive resin is photo-cured layer by layer to form a green part.

Main challenges in the composite slurry based SLA process include high viscosity, low photosensitivity, homogeneity, etc. Compared with liquid resin that are commonly used, the slurry made by mixing solid particles and liquid resin has an increased viscosity. High viscosity poses a challenge for layer recoating, in which a uniform thin layer needs to be created within a reasonable time. The maximum material viscosity that can be handled by conventional SLA processes is less than 3000mPa•S, whereas composite slurry usually has a viscosity far beyond this limit (e.g. 5~250Pa•S). Another main challenge in the composite slurry based SLA process is the reduced cure depth due to the light scattering of solid particles in the liquid resin. Smaller cure depth not only requires smaller layer thickness to be recoated, which is difficult for the viscous slurry, but also makes newly built layer more easily detach from previous layers due to a smaller bonding force. Furthermore, due to the high surface energy of such small particles, it is extremely easy for the particles in the slurry to aggregate. The inhomogeneous distribution of solid particles in green parts will

lead to non-uniform stress inside the part during the post processing, which will consequently contribute to failure of the post processing, such as cracking and delamination.

To overcome these challenges, we investigated the existing SLA processes, and presented a modified SLA process by integrating tape-casting method. The developed slurry-based SLA process has the capability of recoating uniform thin layer for highly viscous composite suspension. To achieve desired material properties, various approaches for increasing the solid loading of green composite parts are studied, including proper preparation of composite suspension, bottom-up image projection, tape-casting based recoating, a two-channel sliding design for layer separation, etc. Two types of polymer composite materials are tested to demonstrate the functionality of the new process, including glass reinforced composite and polymer-ceramic composite. The glass reinforced composite is fabricated from a slurry mixture of glass microspheres and resin. With glass microsphere as the fillers, the final composite can have improved hardness. In the fabrication of the polymer-ceramic composites, we used silver decorated lead zirconate titanate (PZT) as the fillers to enhance the dielectric properties of the composite materials. According to our measurement, the dielectric permittivity of resin/PZT@Ag composite reaches as high as 120 at 100Hz with 18vol% filler, which is about 30 times higher than that of pure resin. With the resin/PZT@Ag composite slurry, we built capacitors in different complex shapes, and measured their specific capacitance as 63 F/g at the current density of 0.5 A/g.

A promising application of the slurry-based SLA process is to indirectly fabricate ceramic materials: A polymer-ceramic composite part fabricated by the slurry-based SLA process is heated in a furnace to burn out the polymer. Since the polymer in the composite part has a much lower melting point than the ceramics, the ceramic part of interest is left behind and sintered as the final product. The debinding and sintering processes for both aluminum oxide and barium titanate (BTO) were studied. BTO-based ultrasound transducer arrays have been successfully fabricated using the presented methods.

Another post processing method for the slurry-based SLA was also discussed to fabricate porous structures. Porous structure has wide application in industry, thanks to some of its special properties such as

low density, low thermal conductivity, high surface area and efficient stress transmission. Both templating and foaming agent methods are used to fabricate porous structures. However, these methods can only produce simple geometries. In recent years, many research studies have been done to use SLA in the fabrication of porous structure, but the porosity that can be achieved is relatively small due to their limited accuracy in building micro-scale features on a large area. We applied the slurry-based SLA process in the fabrication of porous polymer and composite structures using sugar as the foaming agent. With a solid loading of 50wt% of the sugar in the resin, the method can achieve a porosity over 50%. This method can be used to increase the porosity achieved by current SLA methods by over 100%.

Chapter 1 Introduction

1.1 Additive manufacturing and its material selection

Additive manufacturing (AM) has developed for about thirty years since stereolithography (SLA) was invented in mid 1980s. Over the lifetime of the technical field, numerous terminologies (Bourell, 2009) have been used to describe it: additive fabrication, additive processes, layer manufacturing, freeform fabrication, direct digital manufacturing, rapid manufacturing, additive manufacturing, etc. In 2009, the American Society of the International Association for Testing and Materials (ASTM) founded its committee F42 in order to develop standards for additive manufacturing technologies. In their standard terminology F2792-12a (Standard, 2009), “additive manufacturing” is formally defined as *a process of joining materials to make objects from 3D model data, usually layer upon layer, as opposed to subtractive manufacturing methodologies*. To be consistent with the ASTM terminology standard, the *Roadmap for Additive Manufacturing* (Bourell, 2009) released by established leaders in the field used the same term for all applications of the technologies. Since then, “additive manufacturing” has been commonly taken as the standard term for a wide range of technologies, including selective laser sintering (SLS), fused deposition modeling (FDM), stereolithography apparatus, inkjet printing, etc. In this dissertation, we use the same term to describe all the related processes and technologies.

The basic principles of AM technologies are similar: A three dimensional (3D) *Computer Aided Design* (CAD) model is first sliced into a set of two-dimensional (2D) layers; A 3D solid model can then be obtained by fabricating the 2D layers one by one, as depicted in figure 1.1. Comparing with conventional manufacturing processes, additive manufacturing converts the fabrication of a model from 3D to 2D, therefore it can theoretically build a component of any geometric complexity in a cost-efficient way. The manufacturing cost can thus be dramatically reduced in many traditional industries, including space,

defense, automotive, architecture, etc. Meanwhile, AM allows for wider application of personally customized product in industries, such as medicine, fashion and art. Moreover, with the capability of building shapes of free complexity, AM techniques open the doors for novel structures and provide new design ideas for industries, such as robots, electronics, materials, energy, food, etc. Other unique benefits of AM techniques include no tool change, energy efficient, etc.

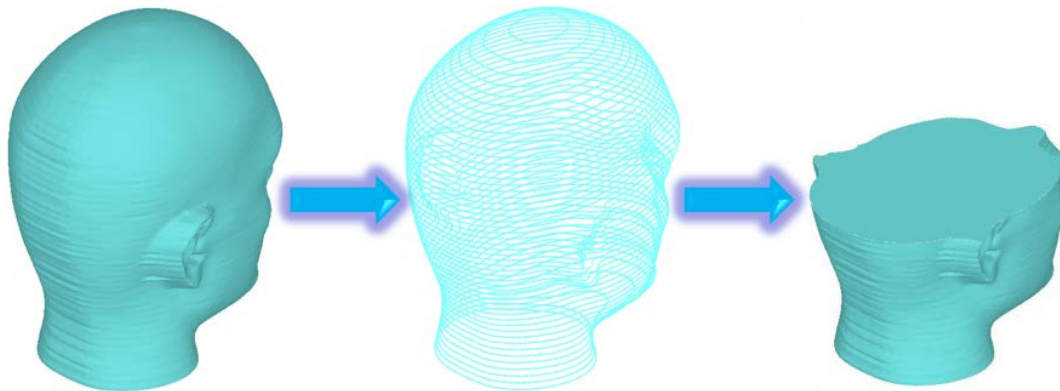


Figure 1.1 Basic principle of additive manufacturing processes

According to the physical principle that is used to fabricate each 2D layer, there are a wide variety of AM processes in the field. In terms of the form of the starting materials, these processes can mainly be classified into four categories, i.e. powder-based, liquid-based, solid-based, slurry-based processes, etc. Table 1.1 lists some typical AM processes for each category. Powder-based AM processes usually use a high energy power source, e.g. laser or electron beam, to sinter or melt powders which will consequently merge into a solid structure. Liquid-based AM processes are based on photo-polymerization of liquid resin, which will be solidified when exposed to ultraviolet (UV) or visible light. Different from powder-based and liquid-based processes, solid-based AM processes fabricate a component from material feedstock in the form of solid, such as laminate and filament. The solid materials are bonded together either by gluing (Feygin, 1999) or heat melting. In addition to these three forms, the feedstock can also be in the form of slurry for some AM processes, in which slurry materials are extruded out through a nozzle and solidified in the air (Lewis, 2006^a).



Figure 1.2 Applications of Additive Manufacturing

Table 1.1 AM process classification based on the form of the starting material

| Classification | Examples of Existing AM Processes |
|----------------|-----------------------------------------------------------------------------------------------------------------------------------------------------------------------------------------------------------------------------------|
| Powder-based | Selective Laser Sintering/Melting (SLS/SLM), Direct Metal Laser Sintering (DMLS), Inkjet 3D Printing (3DP), Electron-beam Melting (EBM), Selective Inhibition Sintering (SIS, Torabi, 2014), Selective Separation Sintering (SSS) |
| Liquid-based | Stereolithography, Multijet Printing |
| Solid-based | Laminated Object Manufacturing (LOM), Fused Deposition Modeling |
| Slurry-based | Direct Ink Writing (DIW) |

Existing AM processes can build objects from a wide range of materials, including polymer, metal, ceramics and composite. Table 1.2 summarizes main AM processes for the fabrication of different types of materials. It can be seen that most of current AM techniques are mainly focused on polymer or metal. Compared to polymer and metal, ceramics and composites are still severely limited for the current AM processes. These two types of materials generally have excellent physical or chemical properties, but are also difficult to produce with traditional manufacturing processes. The goal of this research is to develop a low-cost AM processing method to fabricate ceramic and composite materials.

Table 1.2 AM process classification based on the type of the starting material

| Materials | Existing AM Processes |
|-----------------------|------------------------------------------------------|
| Polymer Fabrication | SLS/SLM, 3DP, SIS, SLA, Multi-jet Printing, LOM, FDM |
| Metal Fabrication | SLS/SLM, DMLS, EBM, SIS, LOM |
| Ceramic Fabrication | SLS/SLM, 3DP, SLA |
| Composite Fabrication | 3DP, DIW, SLA, FDM |

1.2 Ceramic and composite materials

We put a lot of interest in the fabrication of ceramics and composites because of diverse properties that we can get from these materials. In this section, we will briefly discuss the history, applications and traditional manufacturing methods of these materials.

As key engineering materials, ceramics can be found everywhere in our daily life. As early as 24,000BC (Richerson, 2005), people began to mold clay mixed with water into a shape and produce man-made ceramic “earthenware” by firing in kilns at low to moderate temperature. However, traditional

ceramic industries produce ceramic product only for storage, construction or heat resistance. Modern ceramic industries emerge in the second half of the 19th century as people began to understand more about electricity and use ceramic materials for electric insulation. In the first half of the 20th century, numerous efforts were made to learn processing technologies for alumina. Following that, many new ceramics were developed, such as high-temperature ceramics, high-strength ceramics, piezoelectric ceramics, bio-ceramics and so on.

Table 1.3 Examples of Applications of Piezoelectric Ceramics (Richerson, 2005)

| | | |
|--------------------------------------------------|------------------------|-------------------|
| Quartz watches | Charcoal lighters | Smart skis |
| Ultrasonic cleaners | Hydrophone | Sonar |
| Medical ultrasound imaging | Buzzers, alarms | Fish finders |
| Underwater homing beacon | Ocean floor mapping | Emulsifiers |
| Dialysis air bubble detection | Wheel balancers | Motors |
| Nondestructive inspection | Accelerometers | Vibration sensors |
| Ultrasonic physical therapy | Homogenizers | Contact sensors |
| Autofocus camera | Underwater decoy | Impact sensors |
| Precise deflection measurement | Boat speedometers | Loud speakers |
| Zero-vibration tables | Musical greeting cards | Microphones |
| Transformers | Actuators | Printers |
| Telescope mirror distortion correction actuators | Transformers | Igniters |

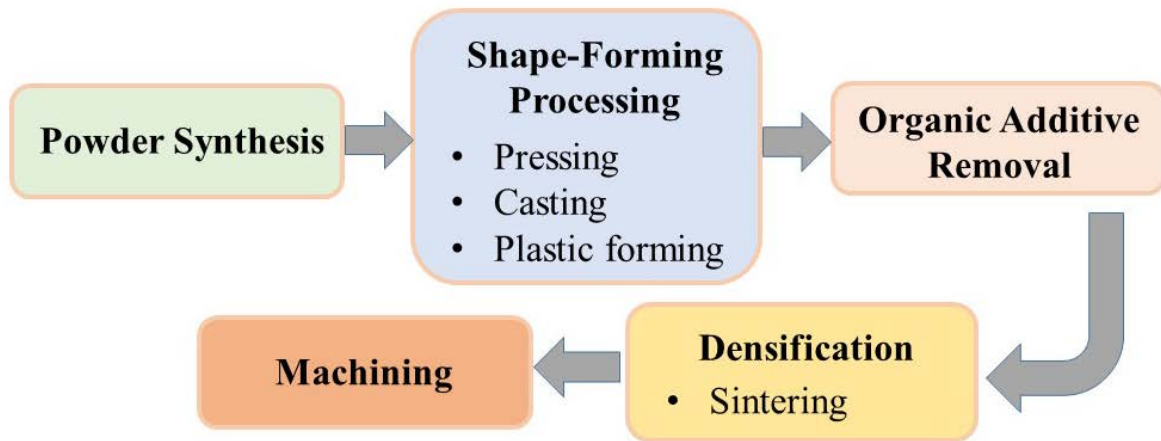


Figure 1.3 Traditional Processing Method of Ceramics

Modern ceramic product has played a critical role in a wide variety of specialty applications: ranging from thermal, electrical, optical, medical to energy and so on. The most common application of ceramics is serving as high temperature insulation components thanks to their high melting point and low thermal conductivity, e.g. in aerospace industry. Furthermore, high hardness and resistance to wear and corrosion make ceramics very suitable materials for cutting tools, valves, bearings, etc. Besides, electrical applications account for the largest economic sector for ceramics (Richerson, 2005), including electrical insulators, piezoelectric ceramics, semiconductors, capacitors, etc. Table 1.3 shows examples of applications of piezoelectric ceramics.

Ceramics are brittle, which pose significant challenges for their fabrication. The fabrication of ceramic components mostly starts with finely ground powder. Fine powders are premixed with other additives, e.g. binders, and are produced into ceramic particulate compacts by shape-forming processes, including pressing, casting and plastic forming. An additive removal step follows in order to obtain pure ceramic compacts. The pure ceramic compact is then densified into strong components through a densification process—sintering. In order to achieve dimensional tolerances and surface finish, machining processes are

required after the densification. Due to the high hardness and brittleness of the materials, machining, usually with diamond tooling, can be very expensive.

In addition to ceramics, composite materials have also attracted a lot of interest in the manufacturing research community in the recent years. Composites are materials containing two or more individual compositions. The individual compositions remain separate within the composites, but yield significantly different physical properties of the combined material. The individual constituents mainly serve as two functions: matrix and reinforcement. The matrix maintains the reinforcement materials in position, while the reinforcement enhances the physical properties of the composite materials. For different applications, various materials can be used as the reinforcement (Gay, 2014), such as glass, carbon, high strength polymers, ceramics, etc. Polymer, carbon, metals can all be selected as matrix, among which polymer are the most popular choice.

The most important purpose for polymeric composite is to improve the properties of polymeric materials, such as thermal stability, stiffness and strength, by incorporating short fibers or ceramic particles (Friedrich, 2005), without sacrificing the weight of the materials. Due to their lightweight and enhanced mechanical properties, polymeric composites have raised many interest in a variety of applications. For example, structural components in automotive industry or wind turbines have been dominated by polymeric composites for decades (Friedrich, 2005).

Another significant use of polymeric composites is to form composites of functional ceramics, e.g. polymer-piezocomposite. In sensors and actuators, a combination of properties such as large piezoelectric coefficient, low density and high mechanical flexibility (Bhimasankaram, 1998) is desired. Pure piezoelectric ceramics have high piezoelectric properties, though, they are brittle and lacking flexibility. Polymeric materials are light and flexible, but hardly generate any piezoelectricity. Even though some polymers have piezoelectric effects, e.g. polyvinylidene difluoride (PVDF), their piezoelectric properties are still very weak. A composite of piezoelectric ceramics and polymeric materials will provide an excellent electromechanical behavior, especially for high frequency applications.

The principal processes for the manufacturing of polymeric composite components include molding, stamping, sheeting forming, etc. During the processes, reinforcement fibers or particles are impregnated or mixed with resin in a lay-up stage. A solidification process is then conducted to harden the polymer matrix. These manufacturing processes achieve a high-throughput composite production but restrict, to some extent, the complexity of product design.

1.3 Stereolithography

SLA was the first additive manufacturing process invented by Charles W. Hull in the mid-1980s (Hull, 1986). It builds a component based on photopolymerization of liquid resin. Liquid resin used in SLA is typically comprised of monomer, photoinitiator, and other additives which induce desired properties. Table 1.4 gives a list of ingredients in photosensitive resin SI500 produced by EnvisionTec (Gladbeck, Germany). When exposed to visible or UV light, the photoinitiator absorbs the light energy of a certain wavelength and generates free radicals in the resin, refer to figure 1.4. The highly reactive free radicals, each of which has an unpaired electron, then attach carbon-carbon double bond contained in a methacrylate monomer (Cai, 2004) by drawing one electron from the bond and leave the other electron in the double bond with a carbon. This reaction produces a carbon radical which will continue to take an electron from monomers until all monomers run out. Through this free radical photopolymerization process, polymer chains can be formed consequently.

In a conventional SLA machine, as shown in figure 1.5a, a tank is filled with liquid photosensitive resin. The fabrication begins when the platform surface is positioned at one layer-thickness under the liquid resin surface. During the fabrication, A UV laser dot is focused on the liquid resin surface and scanning throughout the cross section region of a given 3D model. The position of the UV laser dot is accurately controlled by a two-axis reflecting mirror. As discussed above, when exposed to the UV light energy, the photoinitiator in the liquid resin will decompose into free radicals and cross link the monomers in the liquid to form hardened polymeric material. We call this hardening procedure as *photocuring*. After one layer is

cured, the Z platform moves down for another layer-thickness and a new layer is successively fabricated in the same manner. Since very thin layer thickness (e.g. 25 μm) can be used in laser-based SLA, the surface finish can be very smooth.

Table 1.4 Information of EnvisionTec SI500 on ingredients (EnvisionTec, 2012)

| Components | Approximate % by weight |
|----------------------------|-------------------------|
| 1. Methacrylated monomer | 60-90% |
| 2. 1,6-Hexanediol acrylate | 5-10% |
| 3. Acrylated monomer | 5-15% |
| 4. Titanium Dioxide | 1-2% |
| 5. Photoinitiator | 0.1 - 1% |

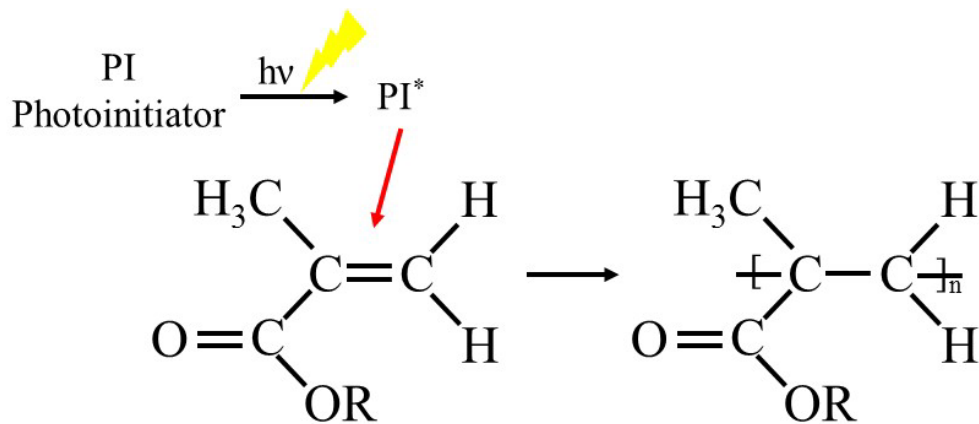


Figure 1.4 Photopolymerization of a generalized methacrylate monomer

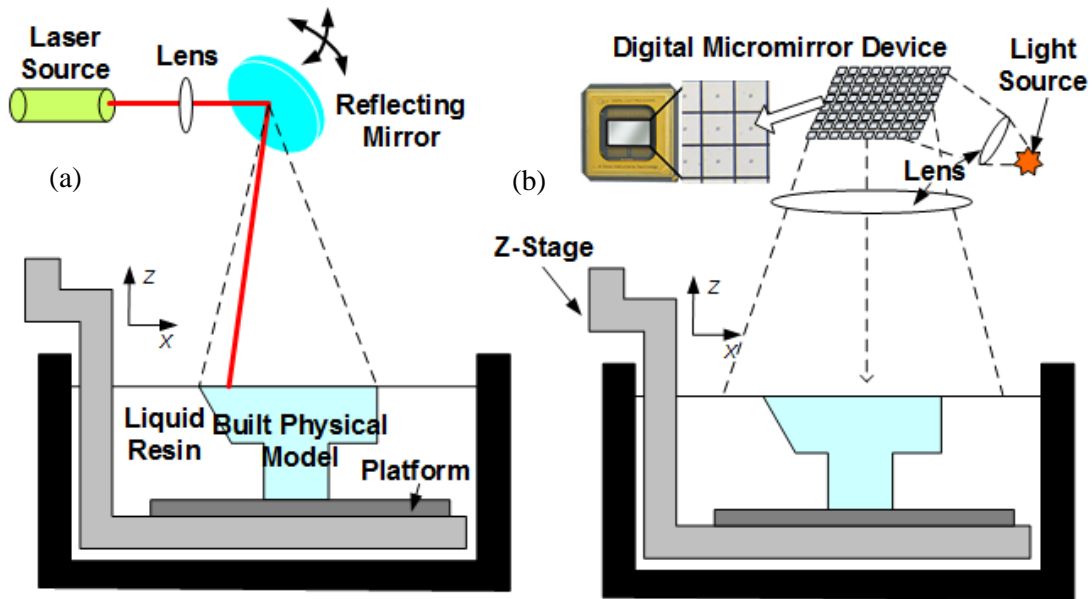


Figure 1.5 (a) Laser based SLA (b) Mask image projection based SLA

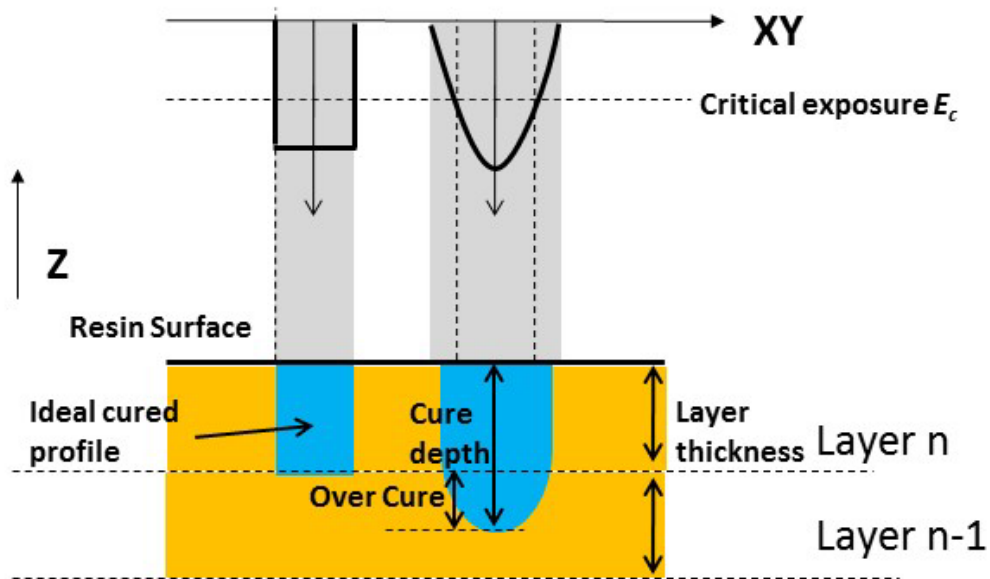


Figure 1.6 Resin Over-cure in SLA processes

The SLA process can use other lighting approaches instead of a laser, such as image projection. The projection-based SLA is an AM process that also uses photopolymerization to fabricate 3D shapes (refer to

figure 1.5b). However, in the projection-based SLA process, a Digital Micro-Mirror Device (DMD) is used to dynamically project a mask image of sliced layers onto the surface of photosensitive resin. The DMD chip consists of millions of micro mirrors, which can be turned on and off at a frequency of 5kHz. Hence, the shape of a whole thin layer can be solidified simultaneously. When a mask image is projected onto the liquid surface, each pixel of the image can be independently controlled. This allows a very high resolution of the fabricated components, and makes the process applicable in micro-scale fabrication. Comparing with the other processes, projection-based SLA has the following advantages:

Fast speed: since a whole image can be projected at a high frequency, this process can potentially achieve a faster production speed than the other processes. An example can be found in (Tumbleston, 2015).

Surface finish: Projection-based SLA solidifies an entire area at the same time, and can use a small layer thickness (e.g. ~1 micron) in the fabrication. These could achieve better surface finish comparing with the other processes (Pan, 2012^a).

Manufacturing cost: The mask image in the projection-based SLA process is implemented by a DMD chip, which is relatively inexpensive comparing with the laser beam in SLS/SLM processes. As a matter of fact, projection-based SLA is becoming one of the most popular processes on the desktop 3d printer market.

Applicable scale: Projection-based SLA is capable of fabricating micro-scale components by reducing mask images to a small size (e.g. ~1mm). It has been widely used in the fabrication of microstructures (Choi, 2006 & 2009; Cheng, 2009; Sun, 2005; Park, 2011).

In projection-based SLA process (Song, 2012), when a mask image is projected on to the surface of liquid resin, the material that is exposed to the energy exceeding a critical energy exposure threshold (E_c) will be cured. The projected light beam is not a uniformly focused ideal square. Instead it follows a Gaussian distribution whose center is at the center of the pixel. Both the light beam radius (XY- plane) and the depth of penetration of resin (Z-plane) are bigger than the cured geometry (Zhou, 2009). The depth that the light can penetrate into the resin is defined as *cure depth*, as shown in figure.1.6 The cure depth

characterizes the maximum thickness of the materials in SLA which can be solidified under the same light intensity and is the most significant factor to determine the layer thickness. We will further discuss it in the later chapters.

As one of the main AM fabrication methods for polymer materials, SLA is a potential process that can be used in the fabrication of ceramic and polymeric composite materials. A promising way of processing non-polymeric materials by SLA process is to premix reinforcement fillers with photosensitive resin. The resin in the slurry can be selectively solidified by controlled light-induced photopolymerization, and finally serves as matrix material in the final component to bind filler particles together. The final component will thereby have enhanced properties introduced by the filler particles or fibers. Post-processing of the fabricated green parts is needed to reinforce the bonding interface between the particles and polymer, or remove the organics in the green part in order to indirectly yield materials which are difficult to manufacture.

1.4 Problem Formulation

The materials used in conventional SLA processes are restricted to photocurable resin, from which only polymer components can be made. Their physical properties such as mechanical strength and hardness are limited for many industry applications. Ceramic and composite fabrication using SLA process is potentially a method to achieve enhanced material properties along with complex geometry. The materials used in the fabrication process are generally prepared by mixing photocurable resin with solid particles. By adding reinforcing fillers into the photocurable resin, the properties of the final components fabricated by the method can be greatly improved. With different types of solid particles, we can obtain significantly different properties for the green parts. However, adding solid fillers into the liquid resin will obviously change the fabrication characteristics of the materials, such as rheological behavior and photosensitivity, and this introduces a lot of challenges to the additive manufacturing processes. That is, the different rheological and photosensitive properties of the mixed slurry make it more difficult use existing liquid-resin-based SLA method to perform the fabrication. In this section, we will discuss the problems involved

in the SLA process for ceramic and composite fabrication and present our method to solve the main challenges in the process.

1.4.1 High viscosity

In projection-based SLA processes, light is projected onto a free liquid surface and new layers are solidified on the top of previously cured layers. After a layer is built, the building platform is moved down for one layer thickness δ (e.g. $\sim 100\mu\text{m}$) to allow the liquid resin to refill the gap. This procedure is called *layer recoating*. Low viscosity of the resin can facilitate the layer recoating with a fast speed and guarantee the gap is fully refilled without voids generated inside. It is recommended by most SLA processes that the viscosity of the used materials should be less than $3000\text{mPa}\cdot\text{S}$ (Jacob, 1992). When viscosity is higher than this limit, uniform layer recoating becomes increasingly difficult.

Compared with liquid resins that are commonly used, the slurry made by mixing solid powders and liquid resin has a dramatically increased viscosity. Higher solid loading (e.g. above 60wt% alumina slurry) in the composite slurry will result in a larger viscosity that can substantially exceed the maximum viscosity limit. With such a high viscosity, the slurry can't flow into the gap within a reasonable time. In a top-down projection based SLA process (Jacobs, 1992) shown in figure 1.7b, a blade is employed to aid in forming a new layer by moving across the free surface of the slurry, but ultrathin layers such as $10\mu\text{m}$ layer thickness still cannot be achieved for viscous slurry. In addition, since the fabricated part is immersed in a tank filled with slurry, tiny features can be easily broken by drag force of the viscous slurry when the platform moves up and down.

Efforts can be made to reduce the viscosity of the slurry. For example, the use of diluents and a heating system may reduce the slurry's viscosity to certain extent (Jang, 2000). However, the addition of diluents may lead to issues such as the large shrinkage and fragility of the structures (Hinczewski 1998^a; Melchels, 2009), as shown in figure 1.8. Increasing the temperatures of composite slurry will require an additional heating system; in addition, the temperature increase has a limited range since resin may be cured by

increased temperature as well. Hence the resulting viscosity may still be too high to ensure a good layer recoating (Hinczewski, 1998^b).

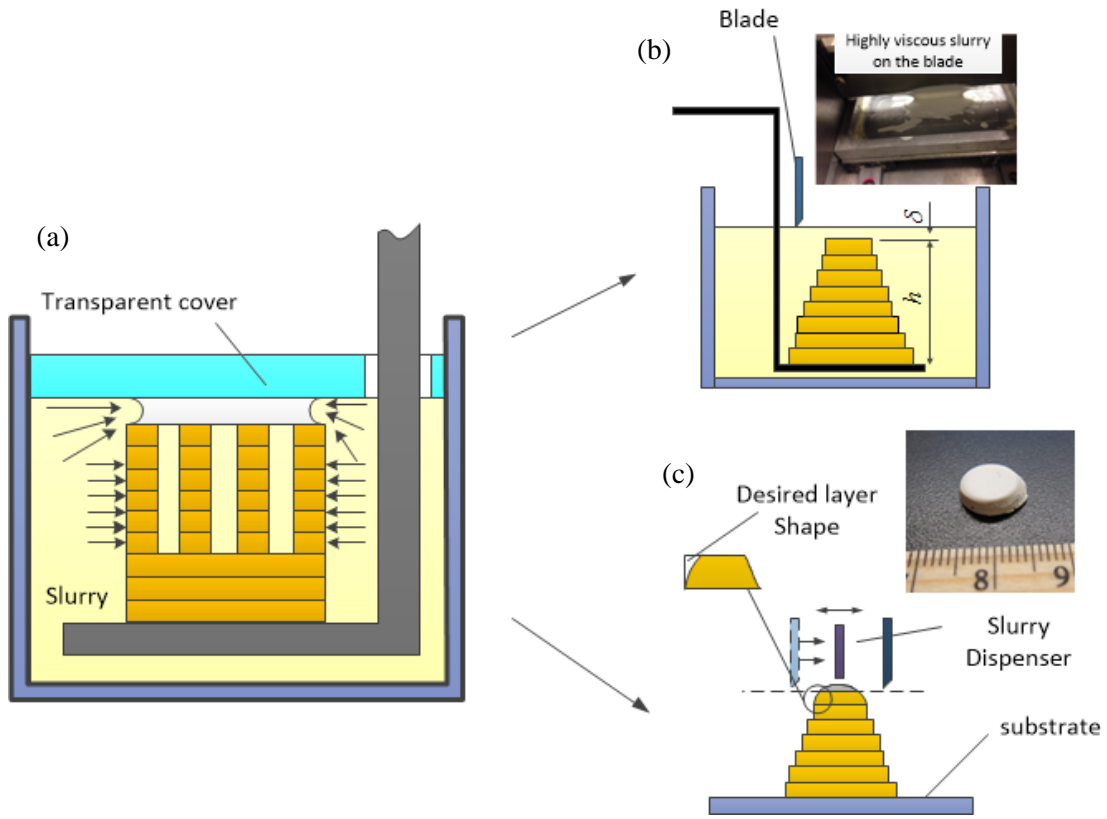


Figure 1.7 Two recoating processes for the top-down projection method.

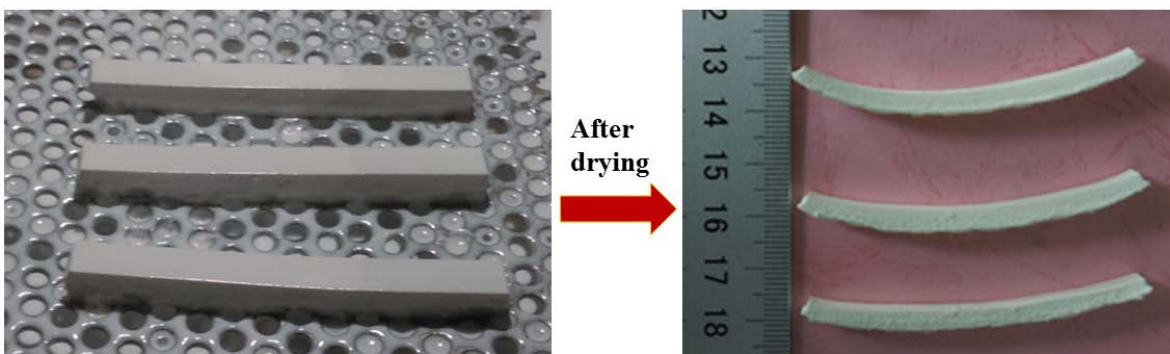


Figure 1.8 Deformation of green parts fabricated from diluted slurry after drying

1.4.2 Slurry homogeneity

Homogeneity is another characteristic of the slurry that should be considered in the fabrication process. As we discussed above, final properties of a component depend on the solid content of the slurry. The particle sizes of the solid filler used in the SLA processes are usually less than 5 μm . Due to the high surface energy of such small particles, it is extremely easy for the particles in the slurry to aggregate. The particle aggregation will reduce the homogeneity of the slurry, and hence influence the property isotropy of final green parts. Furthermore, the inhomogeneous distribution of solid particles in green parts will lead to non-uniform stress inside the part during the post processing, which will consequently contribute to failure of the post processing, such as cracking and delamination (refer to figure 1.9).

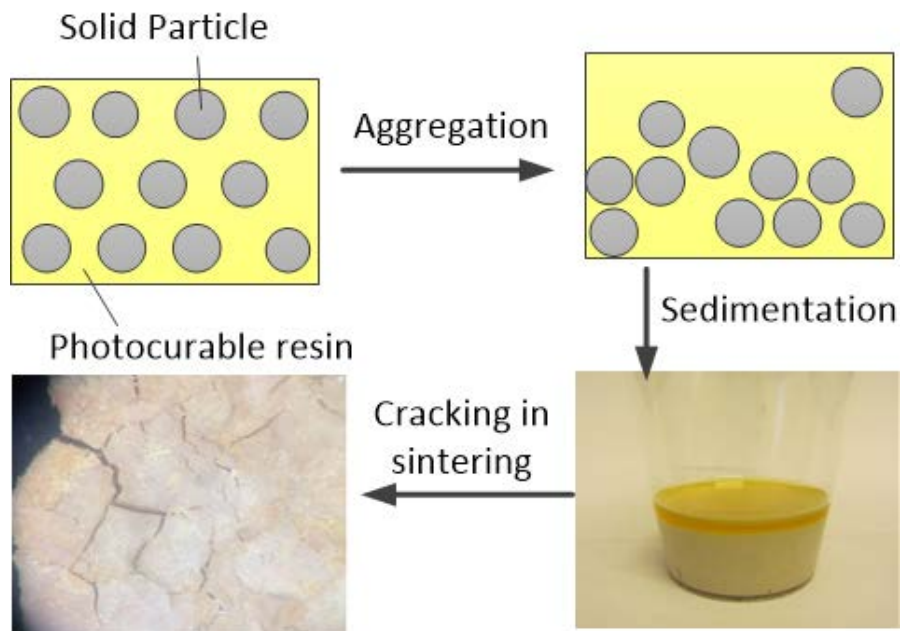


Figure 1.9 Effects of slurry homogeneity

In the top-down projection-based method, the volume of the slurry in the tank must be large enough to ensure the building volume is completely immersed. The particles in the slurry tend to become aggregated after the well-mixed composite suspension has been stored in the tank for a while. In order to ensure homogeneous composite slurry for the fabrication, storage of a large amount of slurry in a tank should be avoided.

Instead of using a slurry-filled tank, another recoating approach is to directly deposit slurry on top of the previously built layers as shown in figure 1.7c. The recoating approach eliminates the needs of a large amount of slurry, and avoids particle aggregation in the suspension. However, due to the surface tension of the slurry, the recoated layers by a blade tend to have defects, which will adversely affect the surface finish of green parts. A test example based on the recoating approach is shown in figure 1.7c.

1.4.3 Low photosensitivity

Another main challenge in the ceramic composite slurry based SLA process is the reduced cure depth. That is, when light travels through composite slurry, the solid particles will absorb and scatter the incident light. The light energy that can access the photosensitive resin is decreased by an order of magnitude. Hence, the cure depth will be significantly reduced. For example, pure photocurable resin typically has cure depth up to 1000 μm , but ceramic composite only has cure depth less than 100 μm under the same light intensity.

Small cure depth brings two technical issues to the fabrication process. First, as discussed in section 1.4.1, a smaller layer thickness is needed to accommodate the reduced cure depth. For example, for ceramic composite mentioned above, a layer thickness as small as 10 μm may be required to ensure sufficient overcure between layers. However, this will impose difficulty in recoating such ultra thin layers, especially for highly viscous slurry. The second issue is layer detachment becomes more difficult. In the SLA process, a transparent cover is commonly used to make the recoated layer more uniform. After the layer is built, it needs to be detached from the cover to allow a new layer to be recoated. To achieve this, the attaching force between the layer and the transparent cover has to be smaller than the bonding force of the layer with the previous layers. A smaller attaching force can be achieved by coating the cover with a film (e.g. Teflon), but it is still too large with respect to the bonding force in the case of composite slurry. The bonding force between layers is mainly determined by light overcure (see figure 1.10), which is the light penetration depth beyond the layer thickness. Since composite slurry has a relatively small cure depth, its overcure range is accordingly small, such that a fresh layer tends to stick to the transparent cover during the layer detachment.

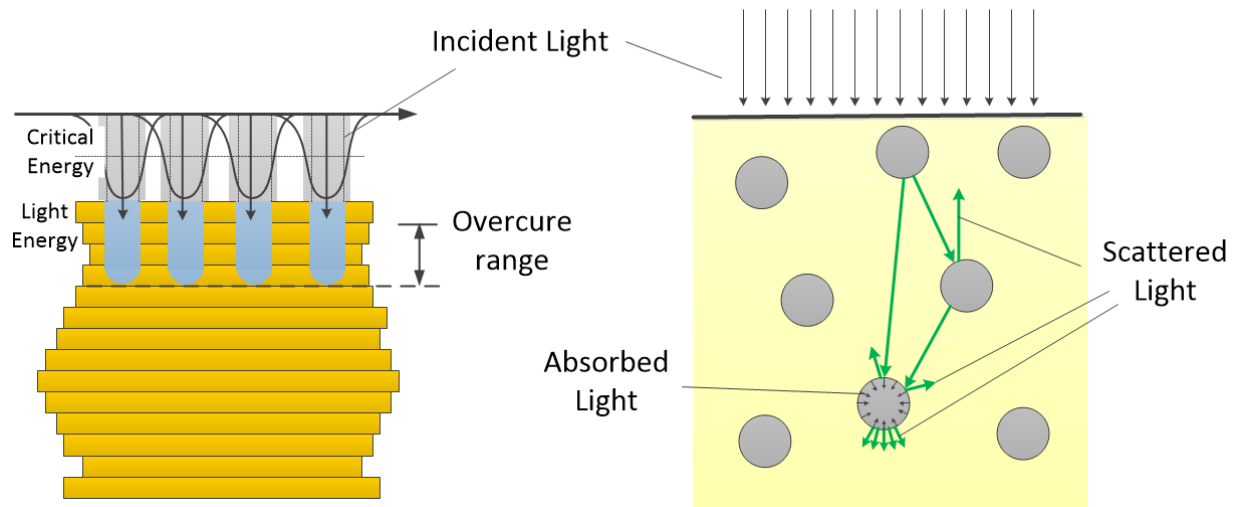


Figure 1.10 Light scattering by solid particles in liquid resin

1.4.4 Post processing

The properties of the fabricated green part can be further improved by proper post processing. Heat treatment is a way that can be chosen to enhance the interface between solid particles and photocured polymer. It has been studied (Deng, 2012) that the temperature has an effect on the final properties of specific compositions.

Another post processing method involves both polymer burn-out and high temperature sintering of the fabricated composite green part, in order to obtain dense organic-free component. This processing method has been extensively studied for ceramic fabrication, in which a polymer-ceramic composite object is heated in a furnace to burn out the resin. Since the resin has a much lower melting temperature than the ceramic, the ceramic part of interest is left behind as the final product. Sintering then follows as a densification process to reduce the porosity of the final part. For both debinding and sintering, temperature, rate and dwell time have to be carefully designed especially for low-photosensitive slurry materials, otherwise polymer will not be able to be completely removed, and cracks and delamination may easily occur during the sintering.

In contrast with debinding and sintering, some post processing methods remove the filler particles in the composite green parts instead of the matrix. For example, in foam agent method, a component containing foam agent particles and ceramics or composites is heated such that foam agent particles can be decomposed and a foam structure can be obtained.

1.5 Research Questions, Hypotheses and Contributions

The principal research goal in this dissertation is to extend material selection options for additive manufacturing, especially ceramics and composites. The AM process that we are focused on is projection-based SLA due to many of its advantages over the other processes. The primary research questions for the dissertation are stated as follows:

RQ1. Can stereolithography method be used to fabricate materials other than plastics?

RQ2. How can post processing be conducted to obtain materials or structures with desired physical properties?

We made the following two hypotheses in response to the primary research questions above. These two hypotheses describe the basic methods that we investigate in the fabrication of ceramics and composites.

Hypothesis 1 Projection-based Stereolithography can fabricate polymer-based composite components from a slurry mixture of photocurable resin and filler particles.

Hypothesis 2 Post processing of polymer-based composites, such as debinding and sintering, sugar foaming, etc., can be used to obtain high performance materials (e.g. ceramics) or novel structures (e.g. porous structures).

The challenges in composite fabrication using SLA, as discussed in the previous sections, include high viscosity, low photo-sensitivity of composite slurry as well as slurry homogeneity. The following three questions illustrate the main problems that need to be solved in the fabrication of polymer-based composite

components using SLA. Three corresponding hypotheses are investigated to answer each of these research questions.

RQ1.1. How should the slurry materials be prepared for the projection-based SLA process to achieve the best properties?

RQ1.2. How can viscous slurry materials be recoated during the SLA process?

RQ1.3. How can a thin layer be detached from constrained surface?

Hypothesis 1.1 A slurry mixture without any dilute solvent added will help avoid large deformation and big shrinkage in the post processes.

Hypothesis 1.2 Recoated layer thickness is restricted by slurry viscosity, which can be reduced by increasing shear rate on the slurry.

Hypothesis 1.3 Separation force becomes less by using sliding mechanism than by direct pull-up.

When the slurry is viscous, it becomes increasingly difficult to recoat a thin layer. Therefore, it is essential to reduce the slurry viscosity during the process in order to achieve thin layer recoating. In the case of polymer-ceramic composite slurry with a non-Newtonian rheological behavior, the viscosity can be changed by controlling the parameters of recoating process without adding diluents into the suspension. The reason that we want to avoid the use of diluent solvent in the slurry is we expect that geometries can be better controlled in the post processes by using less solvent.

When detaching a newly fabricated layer from substrate, we can either choose to directly pull the platform up, or slide the substrate aside. By direct pull-up, the new layer has to overcome the adhesive force from the substrate and can easily detach from the previous layers. Sliding mechanism works well for liquid resin (Zhou, 2013), and can potentially be used to fabricate viscous materials.

According to hypothesis H2, ceramic components can be fabricated through post-processing polymer-ceramic composite parts (also called *green parts*), which can be built by slurry-based SLA. If the polymer in the green parts can be completely burned out, a sintering process can follow to densify the ceramic components. Moreover, porous structures can be fabricated through post-processing polymer-foam-agent composite parts. Water-soluble particles, such as sugar, can be chosen as the foam agent in order to enable an efficient foam agent removal without destroying the other constituents in the composite parts.

Research questions and corresponding hypotheses are stated below to support research question RQ2 and hypothesis H2:

RQ.2.1. How can polymers in a polymer-ceramic composite part be removed in order to obtain pure and dense ceramic materials?

RQ.2.2. What properties of a ceramic component can be achieved by post processing a polymer-ceramic composite part fabricated by slurry-based SLA?

RQ.2.3. How can solid particles in a polymer-based composite part be removed in order to obtain porous structures?

Hypothesis 2.1 The debinding process should be conducted slowly in order to avoid cracks and delamination, while the sintering process should be in an air atmosphere.

Hypothesis 2.2 Properties for both structural (e.g. strength and hardness) and functional (e.g. piezoelectricity) purposes can be achieved by debinding and sintering a green part fabricated by slurry-based SLA.

Hypothesis 2.3 Sugar foaming method can help increase the porosity of a foam structure fabricated by SLA.

To solve the aforementioned problems and verify individual hypothesis, slurry-based SLA methods have been studied in the dissertation. The related chapters to each question and hypothesis are shown in figure 1.11. First of all, a bottom-up projection based SLA process has been developed. In our method, a tape-casting system is integrated to recoat thick slurry layers on a transparent glass substrate; uniform thin layers are then formed by moving the platform down and leaving a desired gap between the previously cured layers and the glass substrate. After the layer recoating, mask images are projected upwards onto the bottom of the substrate. The newly cured layer is separated from the substrate using a two-channel sliding mechanism. Compared with other processes, our method can achieve a thin recoating layer of viscous slurry (as small as $10\mu\text{m}$). By using the bottom-up projection approach, it also removes the need for a large amount of slurry. In addition, a higher shear rate in our tape-casting system is able to reduce the viscosity of suspension during the recoating due to the shear thinning behavior of composite suspension (Chartier, 1999). Hence our slurry-based SLA process can fabricate green parts using slurries that have significantly higher solid loadings. Furthermore, two types of post processing methods were discussed, based on the composite green parts fabricated by the slurry-based SLA process: debinding/sintering for ceramic fabrication and sugar foaming for porous structure fabrication. These two methods work in an opposite way: debinding/sintering removes the matrix material and leaves the filler particles behind in the final part, while sugar foaming removes the filler particles but leaves the matrix material behind.

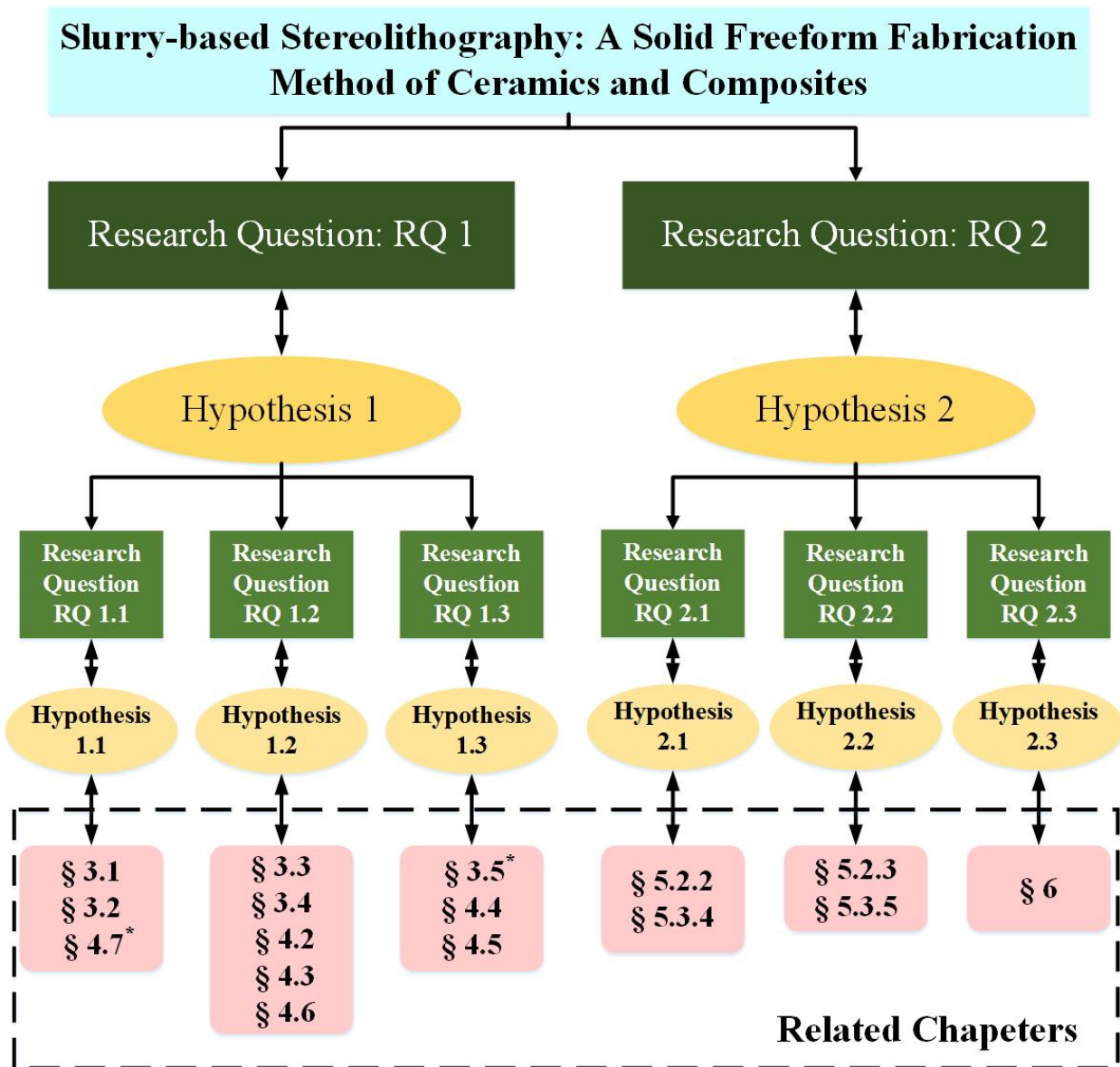


Figure 1.11 Related chapters to research questions and hypotheses

1.6 Outline of this work

The aim of this research is to study the fabrication methods of ceramics and composites using a slurry-based SLA process. More specifically, the major goals of this research include:

- (1) Develop a projection-based SLA process to fabricate polymer-based composite material with high viscosity and low light penetration depth;
- (2) Study the associated process parameters that affect the layer recoating and separation mechanism during the fabrication;
- (3) Study post processing methods for ceramic fabrication and explore the application of the fabricated ceramic and composite components;
- (4) Investigate a sugar foaming process to increase the porosity that can be achieved by conventional SLA processes.

Figure 1.12 gives an overview of all chapters in the dissertation. Chapter 1 introduces research background and primary research goals of the dissertation. In this chapter, research problems are discussed; several hypotheses are derived based on the research questions. Chapter 2 reviews the state-of-the-art of the AM technologies in the fabrication of ceramics and composites.

Chapter 3 and chapter 4 presents the development, modeling and optimization of a slurry-based SLA process. The developed process is introduced in chapter 3, in which a prototype system is demonstrated. Chapter 4 analyzes each step involved in the process, establishes the analytical models for the fabrication process and presents applications of the process in composite fabrication.

Chapter 5 and chapter 6 discusses post processing methods for the polymer-based composite components fabricated by the slurry-based SLA. Chapter 5 introduces the post processing methods for ceramic fabrication. Their application in fabricating piezoelectric components, i.e. ultrasound transducer, is presented in this chapter. Chapter 6 introduces the post processing method for porous structure

fabrication. Its application in increasing the porosity of scaffold structures in tissue engineering is investigated. Chapter 7 summarizes the dissertation and gives some suggestions for future research.

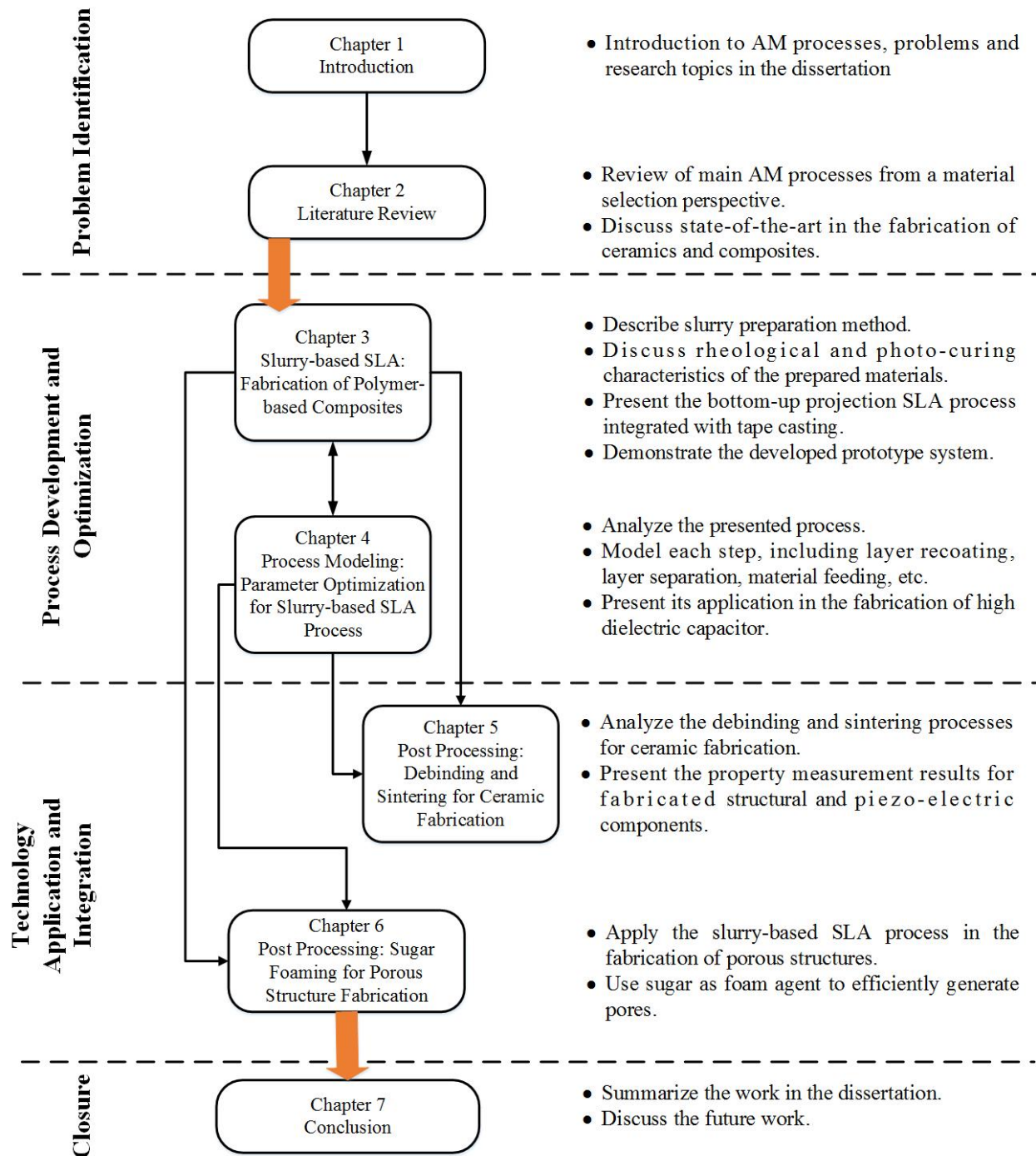


Figure 1.12 Overview of the dissertation

Chapter 2 Literature Review: Additive Manufacturing from a material selection perspective

Various additive manufacturing processes have been invented and applied into production since 1980s. Most of these processes are focused on plastics and metals and many research activities are devoted to improving their fabrication capabilities in terms of manufacturing quality, speed, cost, etc. Adding reinforcement phases into current AM processes is one of the routes to enhance the mechanical properties of traditional plastic or metal components. A lot of research papers have been reported in the recent decade to fabricate fiber or particle reinforced composite components. In this chapter, we will review main methods that have been developed for the fabrication of composites, in particular, polymer-based composites.

Advances in AM of composites have led to the development in ceramic fabrication using AM. Conventional ceramic fabrication processes use ceramic-organic-based composite as the feedstock materials and create dense ceramics through thermally processing the composites. Inspired by the traditional processing methods, efforts have been made to produce ceramics by combining polymer-ceramic composite AM processes with common post processing techniques. In this chapter, we will also review the development in AM technologies of ceramics.

2.1 Composite Fabrication

In this section, we mainly review the state-of-the-art of polymer-based composite fabrication using AM, including direct ink write, stereolithography, binder/ink jetting, selective laser sintering, laminated object manufacturing, etc. Main purposes of these composites are to enhance the mechanical properties of polymers, which are the most common materials available for additive manufacturing. Some composite

fabrication techniques will also be discussed in the next section, but they are used to produce ceramic-based composites, and the reinforcement phases are incorporated in order to reduce the porosity of the ceramic components printed by AM processes.

2.1.1 Indirect methods

Rapid prototyping is originally adopted to fabricate composite materials by injection molding. Taboas et al. (Taboas, 2003) used this method to fabricate porous polymer-ceramic composite scaffolds. They created a ceramic mold by casting Hydroxyapatite (HA)-based slurry in a wax or polysulphonamide (PSA) inverse mold built by a SolidScape 3d printer and sintered in a furnace. These molds were then used to cast Poly(l)lactide (PLA) materials such that a HA/PLA composite can be obtained.

Love et al. (Love, 2014) used another simple way to build fiber reinforced 3D model. They didn't really build a composite component using additive manufacturing, but assemble a 3d printed plastic piece with a long beam wound with continuous carbon fiber filaments.

Another simple method to indirectly create a composite 3D printed part is infiltration. A part is first made by additive manufacturing, which is then put in thermosetting materials such as acrylates or epoxy to fill the pores inside via a capillary effect. This method has been utilized in fabricating polymer-ceramic composites, such as polymer-piezo-composites (Safari, 1997; Bandyopadhyay, 1998), and provides a relatively inexpensive way to produce a fully dense and stiff polymer matrix composite part (Evans, 2005). In his work on piezoelectric composites, Bandyopadhyay and coworkers immersed a ceramic part fabricated by fused deposition in epoxy for one hour for thorough infiltration. After the epoxy was cured, the sample was removed from the epoxy tank and polished such that a piezoelectric ceramic/polymer composite part can be created.

2.1.2 Fused Deposition of Composite (FDC)

The most cost-efficient method of 3d printing composites is through fused deposition modeling (FDM) by replacing conventional thermoplastic filament with composite filament. Carbon has been extensively studied as a filler to reinforce thermoplastic filament for FDM process in the form of particle or fiber.

In 3d printing of polymer-based composites, carbon particle usually serves as conductive fillers to improve the conductivity of plastic components. Leigh et al. (Leigh, 2012) presented a low cost conductive composite material for fabrication of electronic sensors using FDM process. In their method, a regular low-cost desktop FDM machine can be used without any modification. The conductive composite material is prepared from Carbon Black as the filler and polycaprolactone (PCL) as the thermoplastic matrix. Filament for the FDM process is produced by a rolling method. A filler concentration of 15wt% was identified as the optimal setting for a usable electrical conductivity and smooth nozzle extrusion. The extruded material exhibited piezoresistive and capacitive behaviors, which enable its application as smart sensors.

Carbon fiber reinforced polymer composites attracted many attentions recent years due to their unique thermal, electrical and mechanical properties (Shofner, 2003). The polymer-composite filaments for FDM are prepared as follows: Vapor-grown carbon fibers were homogeneously dispersed in poly(acrylonitrile–butadiene–styrene) (ABS) by Banbury mixing. The mixture was shaped into bulk sheets by compression molding process. The bulk sheets were further granulated and extruded into FDM filaments via a single-screw extruder. Thanks to the shearing force in the extrusion process, the carbon fibers can be highly aligned along the axial direction of the extrusion. The carbon fiber content and fiber length play an important role in improving the mechanical properties of the specimen. Ning et al. (Ning, 2015) reported that a fiber content around 5wt% achieved the optimal properties, including flexural modulus, tensile strength, etc.

Although strength and modulus significantly increased in the printed samples, the fiber breakage and pore formation during the material preparation and part fabrication still limit the actual application of this method (Tekinalp, 2014). One potential solution is to add fibers continuously during the extrusion

(Matsuzaki, 2016). Matsuzaki and coworkers developed a new fused deposition modeling process to produce continuous fiber reinforced polymeric composites. Carbon fibers or twisted yarns of natural jute fibers were used as the reinforcement fillers, with the upper limit of fiber volume fraction around 40~50%. In their printing process, fibers are thermoplastic filament are fed into a printing head separately. Before the fiber was impregnated into the nozzle, it was heated by a nichrome wire to enhance its interface with plastic filament. The fiber and the thermoplastic filament are bonded into a single composite filament in the nozzle. Property tests show that the Young's moduli and tensile strengths of the printed composites are improved.

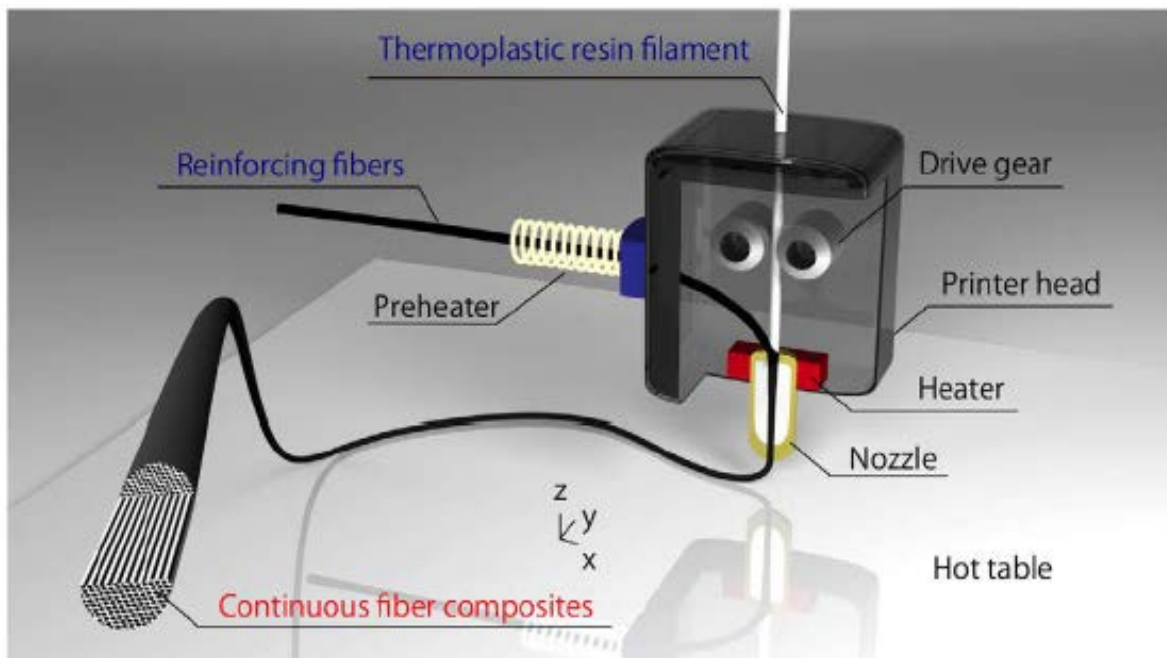


Figure 2.1 Schematic of the 3D printer head to produce continuous carbon fiber reinforced composites (Matsuzaki, 2016)

2.1.3 Direct Ink Write

Direct ink write (DIW) is an extrusion process similar to FDC, but deposits colloidal inks on a platform instead of melted thermoplastic-based composites. After the ink is extruded out of a nozzle, ultraviolet (UV) curing is most commonly used to solidify the materials. For example, de Hazan et al. (de Hazan, 2012)

fabricates ceramic/polymer nanocomposite from high loaded, solvent free UV curable ceramic colloidal inks. They used a 3d robotic deposition method, in which an extrusion system is used to deliver the ink. UV curing was manually done every 2 layers with a UV lamp. Lebel et al. (Lebel, 2010) developed an ultraviolet-assisted direct-write fabrication method to build continuous 3D micro coils. The materials consist of a blend of single walled carbon nanotubes and polymer matrix. The carbon nanotube filler in the composite allows for desired spring rigidity in the coils. Bakarich et al. (Bakarich, 2014) used a commercial extrusion system to deposit different gels on a platform, including alginate/acrylamide gel, an epoxy based UV-curable adhesive and alginate support gel. The gels are cured by a UV light source after each layer is deposited. In the final composite component, the alginate/acrylamide gel serves as reinforcement fiber and the epoxy serves as matrix.

Some research groups tailor the alignment direction of fillers before photocuring the ink, such that anisotropic properties within the final parts can be obtained. Gladman and Lewis (Gladman, 2016) demonstrated a 3d printed hydrogel composite structure with locally aligned cellulose fibrils which can mimic morphology changes exhibited by plants in response to environmental stimuli. In their method, hydrogel composite ink was printed through a nozzle-based system and photopolymerized by a UV light source. The cellulous fibrils were aligned along the extrusion direction under the shear forces that arose as the ink flowed through the nozzle. The resulted filament will consequently swell anisotropically and cause the printed flat structure morph into a pre-defined 3D shape. A similar method was also used in their work on the fabrication of lightweight cellular composite parts (Compton, 2014). Kokkinis et al. (Kokkinis, 2015) used magnet to align the fillers. They fabricated composite materials by combining a direct writing 3d printer with a photopolymerization-based process. Four syringes on the 3d printer are loaded with inks with different formulations. The inks were prepared by mixing photocurable resin with magnetically responsive alumina platelets in different ratios. During the fabrication, different inks are dispensed on a substrate. A magnet was used to align alumina platelets along a desired direction (refer to Le Ferrand, 2015 for similar methods). Following that, a light source was turned on to solidify the entire layer. Since a variety of

materials can be selected in the process, it provides a novel way for the design and fabrication of functional heterogeneous composite materials.

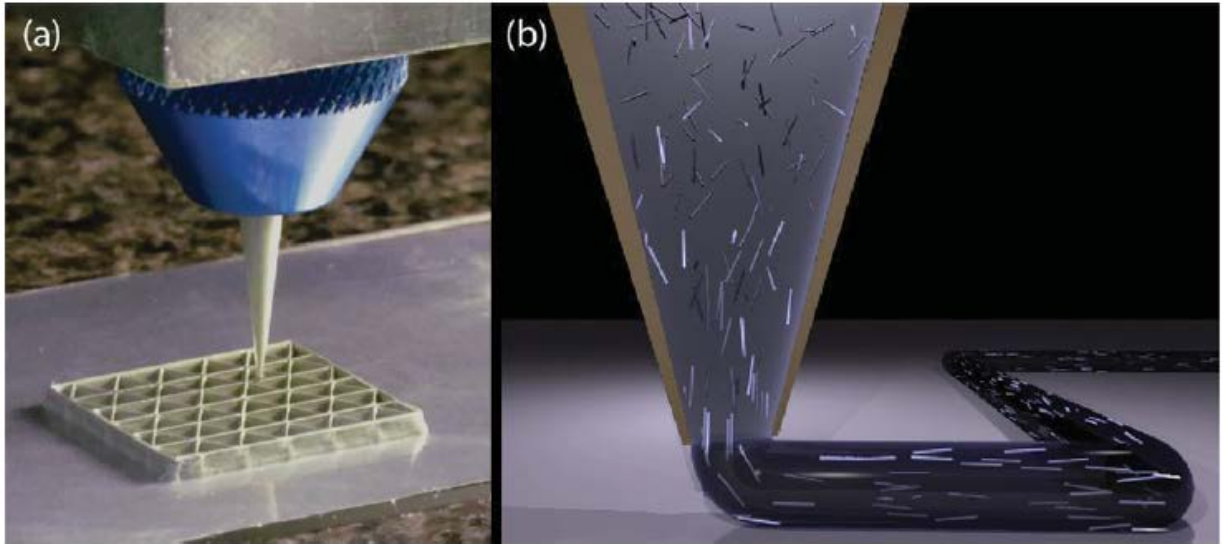


Figure 2.2 Schematic illustration of extruding fiber reinforced suspension via a nozzle system

(Compton, 2014)

Other than UV curing, ink can also be solidified through the evaporation of volatile solution in the deposited layer. Postiglione et al. (Postiglione, 2015) built conductive 3D microstructures by depositing conductive nanocomposite dispersion through a syringe-based dispensing system. The conductive nanocomposite ink consists of multiwall carbon nanotubes (MWCNTs), PLA and a highly volatile solution. Fast evaporation of the volatile solution after liquid deposition leads to the solidification of a wet layer. Similar method has also been used to create polylactic acid (PLA) and calcium phosphate based composite scaffold (Serra, 2013).

In all the direct ink write methods described above, composite feedstock materials are prepared before the fabrication by mixing matrix materials with fillers. Different from these methods, multi-nozzle direct write system can deposit each composition independently to form a composite. Lee and coworkers (Lee, 2014) demonstrates a method to build composite tissues using such a multi-nozzle direct write system. Human ear is comprised of both the auricular cartilage and fat tissue. This complex composition along with

its complex shape make it difficult to regenerate an ear using traditional methods. The authors first built an ear scaffold from poly-caprolactone (PCL), with poly-ethylene-glycol (PEG) as the support materials. After the scaffold was fabricated, PEG was removed by soaking the structure in aqueous solutions. To obtain a complete tissue for the in vitro test, chondrocyte laden alginate hydrogel (CLH) and adipocyte laden alginate hydrogel (ALH) were dispensed on the final PCL scaffold using the same multi-nozzle printing system. Since CLH and ALH were dispensed at different locations on the scaffold, post processing was performed afterwards to crosslink these two compositions.

Although direct ink write process can achieve a high filler concentration, e.g. over 55vol% in (de Hazan, 2012), and consequently relatively good properties in the composites, the accuracy is still limited by the diameter of the extrusion nozzle. Therefore, it probably has more application in the fabrication of lattice structure.

2.1.4 Stereolithography

Stereolithography of composite parts is simply performed by incorporating reinforcement phases into photocurable resin to improve the mechanical properties of the polymer parts. According to the actual purposes, the reinforcement can be fibers or particles. For example, Zak et al. (Zak, 1996) used short discontinuous glass fibers as reinforcements to improve the mechanical properties of polymeric objects. Liu and coworkers (Liu, 2010) modified the photocurable resin with silica nanoparticles in order to enhance mechanical and thermal properties of the materials. Kumar et al. (Kumar, 2012) reported the addition of small amounts of cellulose nanocrystals into curable resin to reinforce the mechanical properties of the printed objects by SLA. Several advantages of cellulose nanocrystals, including biosustainability, biorenewability, low production cost, simple functionalization and dispersibility, make them a very ideal choice for composite reinforcement.

As discussed in chapter 1, the addition of reinforcement phases in SLA will dramatically influence the rheological behaviors of the materials. Zak et al. (Zak, 1996) studied the effects of different factors on the

rheological behavior of fiber-based composites, including the volume fraction of the fibers, their aspect ratio, surface coating, etc. and concluded that the volume fraction of fiber has to be controlled at a low level, i.e. less than 15vol% in order to maintain a low viscosity. Liu et al. (Liu, 2010) tested different solid loadings and found that the optimal mechanical properties, including flexural modulus, tensile strength etc., were obtained with a solid loading of 1-3wt%, since a higher ratio will give rise to agglomerates and rapid increase in the viscosity. Kumar et al. (Kumar, 2012) only used a low filler concentration below 5% of cellulose nanocrystals in the mixture.

Although the mechanical properties can be improved by introducing the reinforcing agents, the improvement is still limited by the low solid loading that is available for current SLA process. The final composites are insufficient in major properties that are required by composite industries, hence they are far from an actual application. Attempts have to be made to further improve the properties of SLA-fabricated composite parts either by modifying the interface between filler and matrix or by increasing the solid loading of reinforcement fillers in the mixture without increasing the viscosity.

Modifying the filler/matrix interface may work for functional composite fabrication. Kim and coworkers (Kim, 2014) presented a method to fabricate piezoelectric composite part with a low solid loading by projection based stereolithography method. In their approach, only 10wt% of BTO nanoparticles were added into photocurable polymer solutions. The low mass loading of BTO nanoparticles leads to insufficient piezoelectric properties of the composites. In order to enhance the mechanical-to-electrical conversion of nanocomposites, the BTO nanoparticles were chemically modified for generating tight bonds with the polymer matrix. The experiment showed a piezoelectric constant of $\sim 40\text{Pc/N}$ in the fabricated piezoelectric composite.

Adding diluent solvent is a general way to achieve relatively high solid loading with a reasonable viscosity. In his research on biocompatible orthopaedic implant produced from ceramic/polymer composite materials, Lee (Lee, 2002) added a solid loading of greater than 40vol.% of alumina into biocompatible monomer solution, to match the elastic modulus of bone, i.e. $\sim 16\text{GPa}$. They used a reactive monomer

(Methyl methacrylate, MMA) as the diluent to both lower the viscosity and improve the reaction rate of the biocompatible monomer solution. Although the viscosity can be reduced to a reasonable level for SLA fabrication, the formation of a rigid ceramic “skin” due to surface evaporation of the solvent can still result in shearing or incomplete coverage of the cured layer with fresh suspension during the process.

In addition to adding fibers or particles, composite component can be produced by placing fibers on the building part during the process. Karalekas (Karalekas, 2004) used nonwoven glass fiber mats as the reinforcement to improve the mechanical properties of SLA products. The fiber mat was manually inserted between two neighboring layers during the SLA process. The interlayer adhesion of photopolymers to fibrous mats brought a lot of challenges to the process. The authors didn't really solve this problem but only embedded a single layer of reinforcing fabric into the mid-plane of a sample. However, experiment tests still reveal higher tensile properties in the reinforced sample compared to non-reinforced one.

2.1.5 Binder/Ink Jetting

Although Lewis (Lewis, 2006b) classified Binder or ink jetting as one of the direct ink write processes, we discuss them separately in this section in that they are quite different from nozzle-based methods in terms of accuracy and material requirement. Binder jetting deposits adhesive binder onto a powder bed to bond powder particle together. Composite powder is simply used in the fabrication of composites by binder jetting. Christ et al. (Christ, 2015) studied the fabrication of short-fiber-reinforced composite materials by binder jetting process. Limited by the capability of the process in spreading a uniform powder layer, only 1% short fibers with a maximum length of 1-2mm were investigated. Cellulose-modified gypsum powder was used as the matrix. Powders were mixed with reinforcement fibers for 10min and printed by a commercial binder jetting printer. By comparing with non-reinforced printed samples, the bending strength of the fiber-reinforced samples were improved by 180% and work of fracture were enhanced up to 10 times.

Ink jetting directly deposits composite materials onto a region of cross section, which will be solidified either by UV curing or drying. Elliott et al. (Elliott, 2013) used quantum dots (QD) as nanoparticle fillers

in a polymeric matrix and studied their fabrication using poly-jet printing process. QD is a type of nanoparticle which has unique optical properties, such as size-dependent photoluminescence property. The addition of QD nanoparticles into the jetting resin will affect the viscosity of the materials and consequently the jetting ability of the printing head. It will also influence the rate and depth of photocuring. In their research, only a small percentage of QDs (up to 0.5wt%) is used in order to guarantee the materials within the printable region of the process.

2.1.6 Selective Laser Sintering

Selective laser sintering (SLS) can build composites by mixing powders with reinforcement fillers. Kenzari and coworkers (Kenzari, 2012) used quasicrystals (QC) as filler particles to produce polyamide-based composite parts by SLS process. The QC particles are mixed with nylon particles with an appropriate concentration (i.e. 30vol% QC). The fabricated quasicrystal-polymer composite parts can have reduced friction, improved wear resistance and are leak-tight.

2.1.7 Laminated Object Manufacturing

Laminated object manufacturing (LOM) is an approach of building 3d models by laminating 2d sheets. When composite sheets are used instead, composite 3D model can be obtained by LOM. Klosterman et al. (Klosterman, 1999) used this method to fabricate glass fiber/epoxy composites. The method lay-ups green composite laminates and cuts the layers into shapes using a CO2 laser. The stacked layers are then consolidated in one step via a vacuum bag/oven cure method. The dimension accuracy of the process is within 1% of the design specification except height, which is around 8%. The bigger error along the height direction may be caused by the lamination-related errors. The fiber volume fraction that can be achieved by this method is around 41-45% and a shear strength of 3600psi is reported in the research, which is significantly lower than that of general high performance composites (i.e. 12,000-18,000psi). A problem with LOM in the fabrication of composites is the poor surface quality. The edge burning effect, due to charring from the cutting action of the CO2 laser, can be clearly seen on the fabricated parts.

2.2 Ceramic Fabrication

As one of the three basic material categories, ceramics have attracted a lot of attentions both in the ceramic and additive manufacturing research community. A complete AM process of ceramics involves material formulation, green part fabrication and post processing. Several reviews have been given on the additive manufacturing of ceramics in the recent years. The interested readers are referred to (Lewis, 2006b) (Travitzky, 2014) and (Zocca, 2015). According to these reviews, main green part fabrication methods for ceramics include extrusion freeform fabrication (EFF), SLA, binder/ink jetting, SLS/SLM, fused deposition of ceramics, LOM, etc. The formulation of feedstock materials replies on the actual fabrication process, while post processing for most of current AM processes of ceramics contains debinding and sintering. In this section, we will provide a brief review of the latest AM technologies of ceramics and give an analysis from material and process perspectives.

2.2.1 Extrusion Freeform Fabrication

Some AM techniques of ceramics form 3D geometries by controlling a nozzle. Different terms have been defined to characterize these techniques, such as fused deposition of ceramics (FDC), filament-based writing (FBW), etc. Their common principle is to deposit a mixture of ceramic powder and solidification agent (e.g. binder) via a nozzle extrusion system and solidify the materials immediately after the extrusion. In the earliest research on extrusion fabrication of ceramics, the ceramic mixture is prepared as filament. For example, McNulty et al. (McNulty, 1998) developed a new ceramic filament formulated entirely from commercially available constituents. Jafari et al. (Jafari, 2000) prepared continuous ceramic filaments from a mixture of ceramic powders, precoated with stearic acid, and binders.

As ceramic suspension is well studied, some extrusion processes directly extruded the mixture without formulating a filament at beginning. In the research of Scheithauer and coworkers (Scheithauer, 2014), stainless steel powder and zirconia powder were mixed with a binder system at a temperature of 100°C. An extrusion system is used to dispense the mixture onto a substrate at a temperature of about 80°C. The

mixture solidifies immediately after printing on the substrate due to the temperature difference. At the end, debinding and sintering processes are used to decompose the organic matter in the samples and densify the structures.

Different routes have been investigated to solidify the ceramic suspension after its extrusion. Scheithauer et al (Scheithauer, 2015) prepared a thermoplastic ceramic suspension with very high solid loading (over 65vol% alumina) and extrude the material using a heatable dispensing unit. The viscosity of the suspension can be reduced to a lower range, i.e. 5-10Pa•s, by heating up it to a temperature of 80°C. The high viscosity could make the extruded material retain its geometry. After debinding and sintering, a final part with density up to 99% can be obtained. Huang and Leu (Huang, 2009a) developed a ceramic fabrication technique called the freeze form extrusion fabrication (FEF). Similar to FDC method, FEF extruded aqueous ceramic paste through a nozzle and deposited the materials on a platform layer by layer. The difference of this process is it has fabrication process performed below the past freezing temperature. Under such as low temperature, the extruded material becomes solid immediately after the extrusion. In their process, a higher solid loading (e.g. 50vol% alumina) and a larger part size can be made to achieve a density up to 98% of theoretical density after binder removal and sintering. Morissette et al. (Morissette, 2000) developed aqueous alumina-poly(vinyl alcohol) (Al₂O₃-PVA) gelcasting suspension in order to improve the mechanical strength of the deposited layers. Gelcasting of each layer is based on polymerization of monomers or cross-linking of polymers in the solution and only requires a low organic content ($\leq 5\text{vol}\%$). The AM of the suspension was conducted using a two nozzle extrusion system, one of which delivered the alumina suspension, and the other one dispensed cross-linking agent solution.

However, a big disadvantage of extrusion freeform fabrication techniques is their relative low accuracy. Due to issues such as inaccurate geometric representation and system control, process voids may be generated in each layer, which lead to poor density of the final parts (Jafari, 2000).

2.2.2 Stereolithography

By adding ceramic powders into photocurable binder, stereolithography can be used to produce dense ceramic green parts. Unlike extrusion freeform fabrication techniques, SLA can yield a higher resolution in the final parts. This offers a great potential to create ceramic parts with very delicate structures, such as scaffolds (Bian, 2012). In traditional SLA process for ceramic fabrication, diluent has to be added and process temperature has to be controlled to tailor the viscosity to be suitable for the SLA process (Hinczewski, 1998). Most ceramic suspensions for SLA used deionized water as the diluent solution, since deionized water can have lower viscosity. A disadvantage of these aqueous ceramic suspensions is the low strength of the as-gelled green body. Resin-based ceramic suspension has higher cured strength than the aqueous ceramic suspension, but its higher viscosity greatly limits the volume fraction of ceramic powders in the suspension. In order to solve the contradiction between the cured strength and viscosity, Zhou and coworkers (Zhou, 2010) replaced deionized water in aqueous ceramic suspension with silicasol, which has low viscosity and can improve the strength of ceramic green parts. The achieved suspension (50vol% silica) in their process has a viscosity less than 1800mPa•s and has a cure depth larger than 200 μ m. However, support structures can still be easily damaged by the viscous suspension during the fabrication, and special support structures have to be designed to avoid the defects.

Another way to overcome high viscosity of highly loaded ceramic suspension is adding a doctor blade to spread the viscous suspension. Lithoz (Schwentenwein, 2015; Hatzenbichler, 2012; Tesavibul, 2012) is one of the most successfully commercialized ceramic AM technologies that adopt a doctor blade to spread slurry layers. They developed a stereolithography-based ceramic manufacturing system based on a Digital Micro-Mirror Device (DMD) chip. Alumina suspension was prepared with a viscosity between 12 and 14 Pa•s. Such a high viscosity necessitates a wiper blade for the recoating of each layer. A rotary vat along with the blade provides continuous slurry flow into the production area but also makes the machine much bigger than the actual building size.

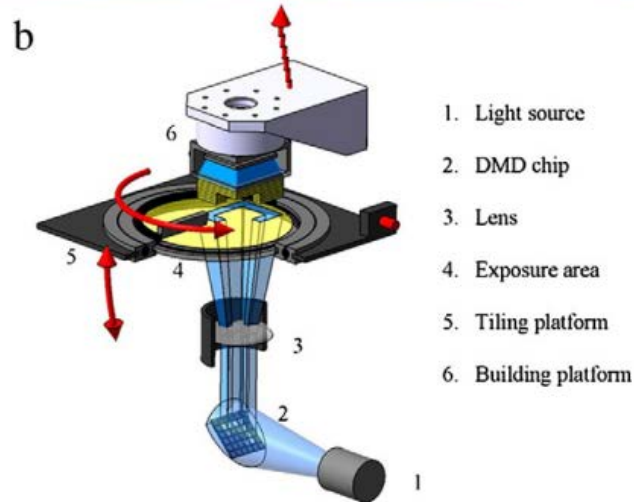
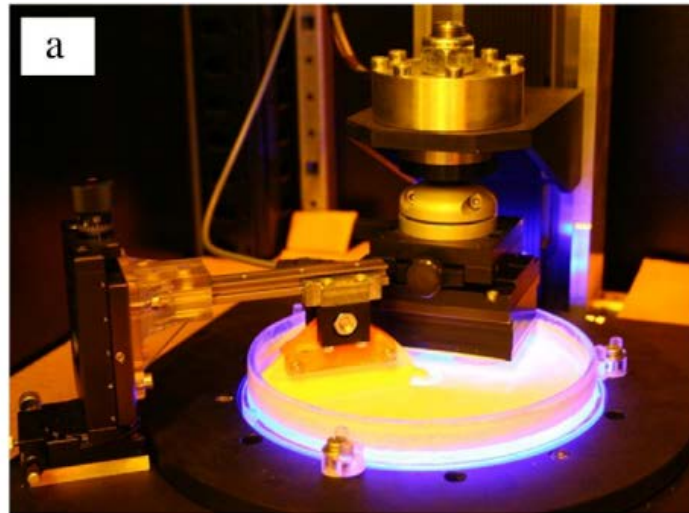


Figure 2.3 Lithoz's digital light processing system for photosensitive ceramic slurries (Tesavibul, 2012)

Some recent research activities (Echel, 2016; Zanchetta, 2016) have focused on the development of UV-active preceramic monomers for ceramic SLA. These materials convert to preceramic polymers under UV light and can further pyrolyze into SiC, SiOC, or other compositions upon heat treatment. Although this method can yield ceramic parts with very excellent mechanical properties, it can only produce Si-based ceramics and is limited in the fabrication of other ceramics, such as alumina, barium titanate, etc.

2.2.3 Binder/Ink Jetting

Ink jet printing of ceramics works in the same way as regular 2D ink printer, except that preceramic polymer or ceramic suspension is used as the ink. Preceramic polymer and its ceramic suspension have been printed by direct inkjet printing process in (Mott, 2001). Silicon carbide was obtained by pyrolyzing the deposited preceramic polymer. Ink jetting of ceramic suspension is more flexible with the ceramics that can be selected, but the contradiction between solid loading and viscosity remains a challenge for the process. Ebert et al. (Ebert, 2009) discussed a direct ink jet printing method for dental prostheses made of zirconia. An empty standard HP printer was modified by injecting the ceramic suspension into its cartridge. Limited by the maximum viscosity of ink jetting, only 27vol% of zirconia powder is mixed within the suspension. A density of 96.9% of the theoretical density was obtained after heat treatment.

Most research activities on jetting related techniques have focused on binder jetting, but the density that has been achieved is limited by the density of powder bed. One solution to improve the final parts is to add reinforcement fillers. Suwanprateeb et al. (Suwanprateeb, 2009) studied the improvement of mechanical properties of hydroxyapatite-based bone implant printed by binder jetting. Hydroxyapatite is a type of excellent biocompatible material used as bone implant. The authors employed apatite–wollastonite (A–W) glass as reinforcing phase and fabricated A-W glass ceramic/hydroxyapatite composite with standard binder-jetting process. After debinding and sintering, a bioactive composite implant can be produced with improved flexural modulus and strength. Inzana et al. (Inzana, 2014) explored the fabrication of bone scaffolds based on binder jetting printing of composite calcium phosphate and collagen. It has been shown that adding collagen into bones could be beneficial for tissue strength and toughness. In this research, a calcium phosphate structure is printed by a binder-jetting process, where a phosphoric acid solution was used as the binder. This binder solution eliminated the need of binder removal, as what was usually done in calcium phosphate printing, and thereby enabled the incorporation of collagen (enhance strength and toughness) into the scaffold structures. By dissolving collagen into the phosphoric acid solution and dispensing it together with the binder into the calcium phosphate powders, a composite calcium phosphate

and collagen scaffold can be produced eventually. A similar AM method was also used in (Bergmann, 2010), but heat treatment still followed to increase the mechanical strength of the scaffolds. Different from Inzana's work, the feedstock materials used in this research are granules consisting of 60wt% bioactive glass and 40wt% calcium phosphate. The composite granule was prepared by a blending and melting process, and a grain size of $d_{50}=41\mu\text{m}$ was achieved in the final granule. Since calcium phosphate and bioactive glass have different biodegradation properties, the presented method provides a possibility for tailored biodegradation capabilities of the implant in an in vivo application.

Another route for improving the density of final parts in binder jetting processes is through infiltration. Melcher et al. (Melcher, 2006) used binder-jetting process to build porous alumina preforms for pressureless infiltration with copper alloy. Yin and coworkers (Yin, 2007) used a similar method to indirectly fabricate a dense composite of $\text{Ti}_3\text{AlC}_2\text{-TiAl}_3\text{-Al}_2\text{O}_3\text{-Al}$. A TiO_2/TiC powder mixture is 3d printed into a "green" preform, which was then pyrolyzed at 800°C and consolidated at temperatures up to 1400°C in Argon. The porous ceramic preform is infiltrated by reactive Al, resulting in the form of different compositions in the final composite. According to the measurement, the toughness of the materials is improved greatly comparing with that of ceramics. Lipke et al. (Lipke, 2010) explored the fabrication of ZrC/W composite parts by combining a binder-jetting process and Displacive Compensation of Porosity (DCP) process. ZrC/W composites possesses higher stiffness, reduced weight and higher resistance to fracture relative to monolithic tungsten or zirconium carbide. A WC preform was first built by a binder-jetting process followed by conventional de-binding and sintering processes. The porous WC preform was then infiltrated by molten Zr_2Cu at $1150\text{-}1300^\circ\text{C}$. In the infiltration, the Zr reacts with WC to yield ZrC and W products for the ZrC/W composites.

2.2.4 SLS/SLM

The simplest way in which SLS/SLM is used to produce ceramic components is through injection molding. Rapid prototyping assisted molding has been an effective method to produce highly dense ceramic

parts. Guo et al. (Guo, 2004) used SLS to build a polymer mold and cast aqueous PZT suspension with it. The polymer mold was then removed during the sintering of the PZT part. However, this method can't really be considered as ceramic SLS/SLM, so we won't discuss it in details in this section.

Selective laser sintering or melting has been mainly used to deal with metallic materials, but has limited capability in fabricating ceramics. Some research papers have been focused on the application of SLS/SLM in ceramic manufacturing. During the fabrication processes, a powder layer is selectively heated and sintered or melted by a focused laser beam, which will induce stresses inside the ceramic part due to the thermal gradients. These stresses will consequently cause crack formation in the material. In order to avoid crack formation, Wilkes et al. (Wilkes, 2013) preheated the ceramic powder bed to 1600°C with a CO₂-laser (output power 1,000W) and then used an ND:YAG-laser (output power 150W) to selectively melt the ceramic powder. By preheating the powder bed to a higher temperature, thermal gradients during the fabrication are reduced and therefore mechanical stresses can be significantly relieved. However, the surface finish achieved by this method is rough due to the difficulty in the control of melting pool. Crack formation may still occur during SLM, caused by other reasons such as deposition of cool powder layers on the preheated layer.

Compared with direct SLS/SLM of ceramics, indirect SLS is probably a more feasible way to be applied in actual production of ceramics. In indirect SLS processes, a mixture of ceramics and polymers is used, in which polymer phase serves as a sacrificial binder. Shahzad et al. (Shahzad, 2013; Shahzad, 2014) produced polymer-ceramic composite particles via a thermally induced phase separation method. The synthesized composite particles were then fabricated by conventional SLS process. The green parts were debinded and sintered in the post processes and only a density of 38.5% of true alumina was obtained. The low sintered density can be explained by the low green density and inhomogeneous green microstructure. The concentration of ceramics in the composite powder can't be high, otherwise the green parts will be fragile and delaminated.

It has been reported (Subramanian, 2015) that SLS-fabricated green parts have a porosity which is quite similar to that of the powder bed from which they are formed. That means the density of ceramic parts fabricated by indirect SLS is limited by the low density of its green parts. Infiltration and isostatic pressure have been employed to increase the density of the final parts (Shahzad, 2013; Deckers, 2012), but the resulted density was still less than 90%.

2.2.5 Slurry-layer casting

Many recent work on ceramic AM particularly explored the usage of slurry casting in ceramic green part fabrication. These research papers (Yen, 2015; Tang, 2015; Muhler, 2015) argued that appreciable density can be reached by the use of ceramic slurries. Both Tian (Tian, 2012) and Tang (Tang, 2005) studied slurry-based AM processes for ceramic fabrication. Tian claimed that layer-wise deposited slurry could achieve a relatively high green density of ceramic film after drying compared with powder-based or organic binder-based ceramic processing methods. They used water-based ceramic slurry as the feedstock material and deposited slurry layer through a deposition system similar to (Yen, 2015). After drying for about 2min, the ceramic tape was sintered by a 100W laser system. The final part was post processed in a furnace for improved density. The process developed by Tang et al. works in a similar way. A layer of ceramic slurry, consisting of water, silica sol (40-50nm) and silica powder (10 μ m), was deposited onto a platform. The slurry was scanned by a laser beam and became solid due to the “gelling effect” of the silica sol.

The fabrication of ceramic slurry can also be accomplished in an opposite way, as described in (Tang, 2015). When a dried layer of ceramic slurry was scanned by a laser beam, the binder (polyvinyl alcohol) in the scanned region (usually the boundary of a 2D cross section) evaporated, leaving a weaken area with only ceramic powder along the scanning track. A green part could thus be separated from the dried slurry block along the weaken area. A benefit of this method is that no support structure was required in the process since the weaken area could serve as the support.

A challenge for slurry-based AM processes is to stably spread thin and uniform slurry layers. Yen et al. (Yen, 2015) developed a slurry-layer casting system for additive manufacturing of ceramics. The presented slurry-layer casting system is comprised of a slurry-feeding mechanism, a casting device and a cleanup mechanism for the casting device. The tested slurry only has a viscosity less than 650cP, which is far below that of the ceramic slurry used in our method. Waetjen et al. (Waetjen, 2009) used an airbrush spraying method to deposit aqueous ceramic suspension instead of conventional doctor blade. The spraying can handle alumina suspension with a solid loading of 60-76wt%. After the spraying, the slurry layer was dried with an infrared heater, followed by SLS method. An average density of 98.5% of alumina parts was achieved by their method.

2.2.6 LOM

Tape casting and LOM process has been investigated in the last decade to produce 3D ceramic parts. Aqueous ceramic suspension is cast with a doctor blade system into ceramic tapes, which are used as starting materials in the LOM process (Gomes, 2009). LOM process cuts one layer of ceramic tape with a laser and laminates it on top of the previous layers using a binder solution as adhesive agent. Post processing for LOM is the same as other ceramic AM methods, including binder pyrolysis and sintering. The biggest issues with LOM process are the relatively large amount of material waste during the fabrication and poor surface finish limited by the thickness of ceramic tapes.

2.2.7 Electrophotographic Printing

Electrophotography process has been used in AM of ceramics (Kumar, 2004). In this process, a photoconductor drum is used to electrophotographically create a layer of part powder or binder powder in a given image pattern and transfer it onto a building platform. For ceramic fabrication, depositing binder powder on part powder appears to be a better choice. That is, binder powder is first electrophotographically printed on uniformly deposited part powder and then thermally fused to bind the part powder together. A

resolution up to 600dpi can be achieved in each layer but the instability of powder transfer prevents its further application in ceramic fabrication.

Pascall and coworkers (Pascall, 2014) also utilized electrophotographic principle to process ceramic powders but their method works in a different way. Ceramic suspension was filled into a space between a photoconductive electrode and a counter electrode. The charged region on the photoconductive electrode was dynamically changed by illuminating different light patterns such that the ceramic powder in the suspension can be selectively deposited onto a desired region on the electrode. This is a promising method that can allow for the fabrication of multiple types of ceramics simultaneously, but the low density of deposited ceramic layer and the small building volume are two big issues that need to be solved for the process.

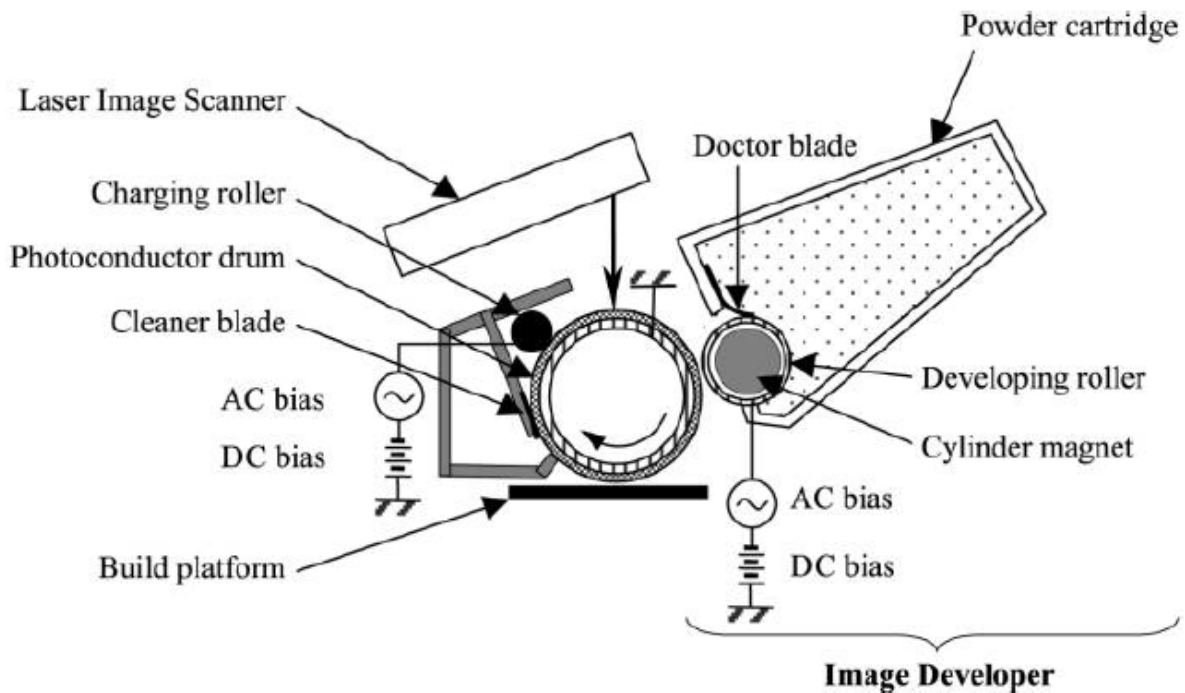


Figure 2.4 Schematic of an electrophotographic printing system (Kumar, 2004)

2.3 Summary

In this chapter, we outlined major AM technologies that have been studied in the fabrication of composites and ceramics, including DIW, SLA, LOM, SLS/SLM, etc. In the review of composite AM processes, particular emphasis was given to polymer-based composites. According to the review on ceramic fabrication, most of current AM processes of ceramics are based on the fabrication of ceramic-polymer composites (i.e. green parts) and heat treatment. In other words, to fabricate a ceramic part, a ceramic-polymer composite green part is first built and then heat-treated for consolidation. Therefore, many processes can be utilized in the production of both composites and ceramics, such as fused deposition, SLA and SLS.

AM processes for polymer-based composites are almost the same as those for polymers, except that polymeric feedstock materials are replaced by composite ones. The composite feedstock materials are either prepared before or during the process. When composite materials are formed in situ during the process, continuous fillers can be achieved in the final parts. Otherwise, only discontinuous fillers can be imparted into the parts.

To the best of our knowledge, slurry-based AM processes can achieve better properties in the final ceramic parts, such as extrusion freeform fabrication, SLA and slurry-layer-casting-based SLS. According to limited reports on powder-based AM processes for ceramics, they usually yield inferior properties to slurry-based ones, which can be explained by the low density of the powder bed in these processes.

Chapter 3 Slurry-based SLA: Fabrication of Polymer-based Composites

Recognizing the importance of ceramic slurry in ceramic processing, we presented a slurry-based stereolithography (SLA) process by replacing liquid photosensitive resin with ceramic-resin composite slurry. Photosensitive resin is the material used in conventional SLA processes, from which only polymeric components can be fabricated. The presented slurry-based SLA process fabricates polymer-ceramic composite components by photocuring ceramic composite slurry. Ceramic composite slurry is prepared by mixing ceramic filler powders with photocurable resin. In the fabrication process, the resin serves as binder to bond ceramic powders into given 3D shapes. The physical properties of the polymer-ceramic composite parts largely depend on the amount of ceramic particles that are mixed in the slurry. However, a higher percentage of ceramic fillers in the slurry mixture will dramatically decrease the curing sensitivity of the slurry and increase its viscosity. Hence both layer recoating and curing would be more difficult than those in liquid resin-based SLA. To overcome these challenges, we developed a projection-based SLA process by integrating slurry tape-casting and a sliding motion design for layer separation. Compared with other processes, our method can achieve a thin recoating layer (as small as 10 μ m) of ceramic composite slurry and can fabricate green parts using slurries with higher solid loadings.

3.1 Ceramic composite slurry formulation

In our study, different fillers were tested using the presented slurry-based AM process, including solid glass microsphere (Z-CEL, 8054, Potters, PA), Aluminum Oxide (type CR3, BaikaloX, Charlotte, NC), Zirconia (TZ-3YS-E, Tosoh, Tokyo, Japan), Barium Titanate (BTO, Sigma-Aldrich, St.Louis, MO) and

Lead Zirconate Titanate (PZT, Piezoelectric Technology Inc., Indianapolis, IN). In order to obtain homogenous suspension, the powders were first deagglomerated in an azeotropic mixture of methylethylketone (66 vol%, MEK, Sigma-Aldrich, Saint Louis, MO) and ethanol (34vol%, Sigma-Aldrich, Saint Louis, MO) with dispersant by ball milling (Fritsch GmbH, Idar-Oberstein, Germany) at the room temperature for 12 hours. The same ratio of azeotropic mixture was also used in (Chartier, 1999; Mikeska, 1988). The solid loading of the dispersion is 25vol%. Phospholan PS-131 (AkzoNobel, Chicago, IL) and Triton x-100 (Dow Chemical Co., Midland, MI) were selected as dispersant due to their good dispersion properties (refer to Mikeska, 1988; Paik, 1998; Jang, 2000). Dispersant with 0.5-0.8wt% concentration was added into the mixture, on a dry weight basis of ceramic powders.

The dispersion is then dried at 50°C for 12 hours. After the evaporation of the solvent in the dispersion, dry ceramic powders with dispersant adsorbed onto their surface can be obtained. The deagglomerated ceramic powders (containing 0.5-0.8wt% dispersant) were dissolved in commercial photocurable resin (SI500, EnvisionTec Inc., Ferndale, MI) in a mortar based on a designed ratio. The photocurable resin has a viscosity of 0.18Pa•s at 30°C and a density of 1.10g/cm³ at 25°C. Its glass transition temperature is 61°C. The resin is selected in our study due to its excellent photosensitivity. It contains 60-90wt% Methacrylated monomer, 5-10wt% 1,6-Hexanediol acrylate, 5-15wt% Acrylated monomer, 1-2wt% Titanium dioxide and 0.1-1wt% photoinitiator. Additional 0.2wt% dispersant was added into the suspension to ensure full dispersions of particles. The suspension was then milled at 200rpm for 1-2 hours with stainless steel beads to break down the agglomerates formed during solvent evaporation.

Similar to other SLA processes (Dufaud, 2003; Ventura, 2000; Cheverton, 2012; Chabok, 2012) for ceramic composite fabrication, solvent such as IPA can also be added to reduce the slurry viscosity. In our process, less diluent solvent is required, due to the integrated tape casting system and two-channel sliding design. Finally, the mixture is degassed in a vacuum chamber (Bel-Art Products, Wayne, NJ) for 0.5-5 hours to remove the air bubbles that may be generated during the ball milling process.

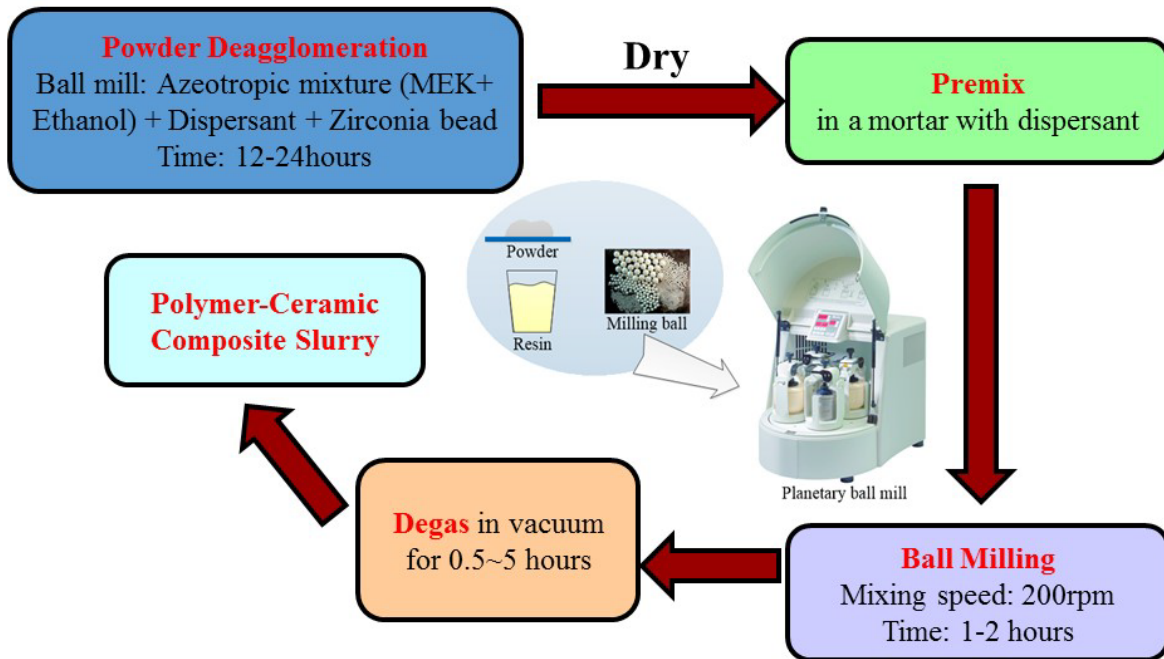


Figure 3.1 Preparation of ceramic composite slurry

3.2 Curing characteristics

Different from pure photocurable resin, curing characteristics of ceramic composite slurry are significantly influenced by the light scattering effect of the ceramic particles in it. In other words, when light travels through highly concentrated ceramic composite slurry, its propagation direction will be changed by the ceramic particles. Therefore, penetration depth of the incident light, or cure depth of the slurry, is reduced dramatically. Table 3.1 shows the cure depths of four different types of composite slurry that are measured in a prototype system of the slurry-based SLA process developed in our lab. A single-layer-curing method is used to measure the cure depth of ceramic composite slurry. In the measurement, a layer of ceramic composite slurry is first coated on a film collector by a doctor blade, whose height is set to be 3~5 times bigger than the expected cure depth. A digital image of a circle with a diameter of 10mm is then projected onto the coated layer of ceramic composite slurry. After the mask image is projected for 10 seconds, a thin layer of ceramic composite will be solidified. The thickness of the solidified layer is

measured by a micrometer caliper, which is considered as the cure depth of the material. The cure depth is a significant parameter that determines the thickness of each layer during the fabrication of a 3D model. Empirically, layer thickness has to be set less than one half of the cure depth in order to ensure tight bonding force between neighboring layers.

Table 3.1 Physical properties and cure depths of ceramic powders with 65wt%

| Type | Cure depth (μm) | d50 (μm) | np@632.8nm | Density (g/cm ³) | Resin | Cure time (s) |
|------------|-----------------|----------|---------------------------|------------------------------|-------|---------------|
| PZT | 39 | 3 | 2.397 | 7.7 | SI500 | 10 |
| BTO | 97 | 3 | 2.4043 | 6.08 | SI500 | 10 |
| Alumina | 340 | 1.1 | 1.766 | 3.95 | SI500 | 10 |
| Glass | 590 | 5 | 1.5151 [†] | 1.8 | SI500 | 10 |
| Pure resin | 1087 | NA | 1.382-1.441 ^{††} | 1.10 | SI500 | 10 |

Note: †refer to (data for glasses on <http://refractiveindex.info/>) ††refer to (Griffith, 1996).

The relation between cure depth and energy input is defined by the Jacob's equation (Jacobs, 1992):

$$C_d = D_p \ln\left(\frac{E}{E_c}\right) \quad (3.1)$$

where C_d is the cure depth; E is the energy density of incident light; E_c is the critical energy density, i.e. the minimum energy for the photocurable resin to be solidified; and D_p is the resin sensitivity. The light intensity of our projection system is $\sim 31.6 \text{mW/cm}^2$ measured by an illumination level meter (Simpson

electric, WI). The light energy absorbed by ceramic composite slurry is smaller than the light source energy due to the energy loss when light passing through the Polydimethylsiloxane (PDMS)-coated film collector (refer to section 3.5). In our setup the thicknesses of the glass and the PDMS is ~2.38mm and ~1mm, respectively. The cure depth may be slightly different if their thicknesses are modified.

For ceramic composite slurry, the parameter D_p is closely related to the absorption by the photoinitiator, the light absorber (e.g. dye) in the resin, as well as the light scattering by mixed particles (Tomeckova, 2010^a). According to Griffith and Halloran's scattering equation for ceramic composite suspension (Tomeckova, 2010^a; Griffith, 1997; Abouliatim, 2009; Tomeckova, 2010^b), D_p can be determined by the following equation:

$$D_p = \frac{2d_{50}}{3\tilde{Q}} \frac{n_0^2}{\Delta n^2} \quad (3.2)$$

where d_{50} is the average particle size; Δn is the refractive index difference between the solid particle (n_p) and the liquid resin (n_0 , i.e. $\Delta n^2 = (n_p - n_0)^2$). \tilde{Q} is the scattering efficiency term, which embodies a complex physics for scattering behavior in a dense system. Empirically it depends on volume fraction ϕ , d_{50} , and the light wavelength λ .

Equations have been studied in (Gentry, 2013) to describe the effect of scattering on cure width ω_{cure} :

$$\omega_{cure} = \omega_{beam} + 2\omega_{ex} = \omega_{beam} + 2S_w \ln\left(\frac{E}{E_w}\right) \quad (3.3)$$

where cure width ω_{cure} is obtained by adding the illumination width (ω_{beam}) and excess width (ω_{ex}) due to light scattering in the horizontal direction; and excess width ω_{ex} is related to the width sensitivity S_w , incident light energy E and the width critical energy dose E_w .

Compared with regular photocurable resins, the cure characteristic of ceramic composite slurry is affected by the slurry sensitivity defined in equation (3.2) and (3.3). Specifically, the cure depth depends on the refractive index difference between the filler particle and the resin, the particle size, and the solid

loading of solid powders in the suspension. Table 3.1 shows the measured cure depth of PZT, BaTiO₃, Alumina and glass microsphere with the same solid loadings - 65% weight concentration.

Our experiments show that the cure depth of ceramic composite slurry is dominated by the refractive index difference Δn . Among the three types of ceramics that are tested, PZT has the largest refractive index, while Alumina has the smallest one. Consequently, the cure depth of PZT is the smallest, while the cure depth of Alumina is the largest. Glass microspheres that are tested have good optical transparency, and its refractive index is smaller than alumina, and slightly higher than the SI500 resin. The d₅₀ as shown in the table is the size from the vendors' datasheets. The actual particle size will be smaller due to the grinding process.

3.3 Rheological characteristics

We studied the rheological behaviors of alumina slurries using a Brookfield dial reading viscometer equipped with a small sample adapter (SC4-14/6R). Alumina slurries containing 65wt% alumina powder and 0.5wt% dispersant on a dry weight basis of the powders were first analyzed. Deionized (DI) water was added as dilute into the resin with a weight concentration of 40~60wt% based on the total weight of the resin and the solvent. Figure 3.2 shows the viscosity of three different dilute concentrations at the shear rate $1\sim 8s^{-1}$. When the dilute concentration is below 45wt% or above 55wt%, the viscosity exceeded the force range of the instrument and can't be recorded. The measurement results indicate that the viscosity at the shear rate of $\sim 8s^{-1}$ was reduced to 8,000cP when 55wt% dilute solvent was added, which can be used in conventional SLA process.

As we discussed in chapter 1, adding dilute solvent will reduce the strength of the green parts and consequently contribute to their large deformation during post processing. For this reason, we studied the viscosity of slurries at different solid loadings without any dilute solvent and plotted the measurement results in figure 3.3. It is shown in figure 3.3 that the slurries exhibited shear thinning behavior with a Newtonian plateau at high shear rate. The viscosity of 50wt% slurry at high shear rate exceeds the range of

the instrument and were not recorded. The slurry with a solid loading of 55wt% or higher is too viscous to be measured. The viscosity of 50wt% slurry at the shear rate $\sim 4\text{s}^{-1}$ is over 80,000cP.

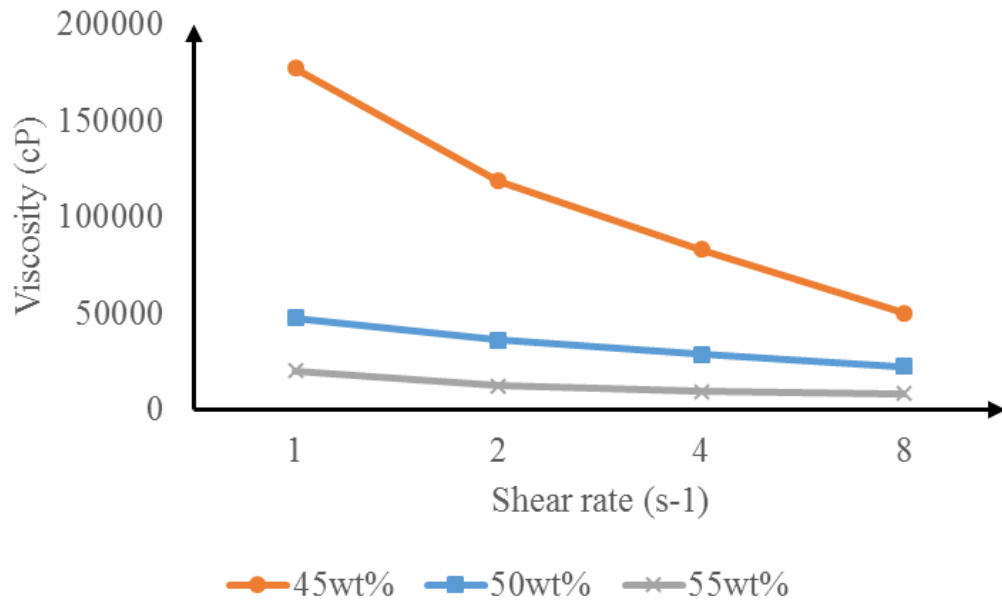


Figure 3.2 Viscosity of alumina slurries with different concentrations of dilute solvent

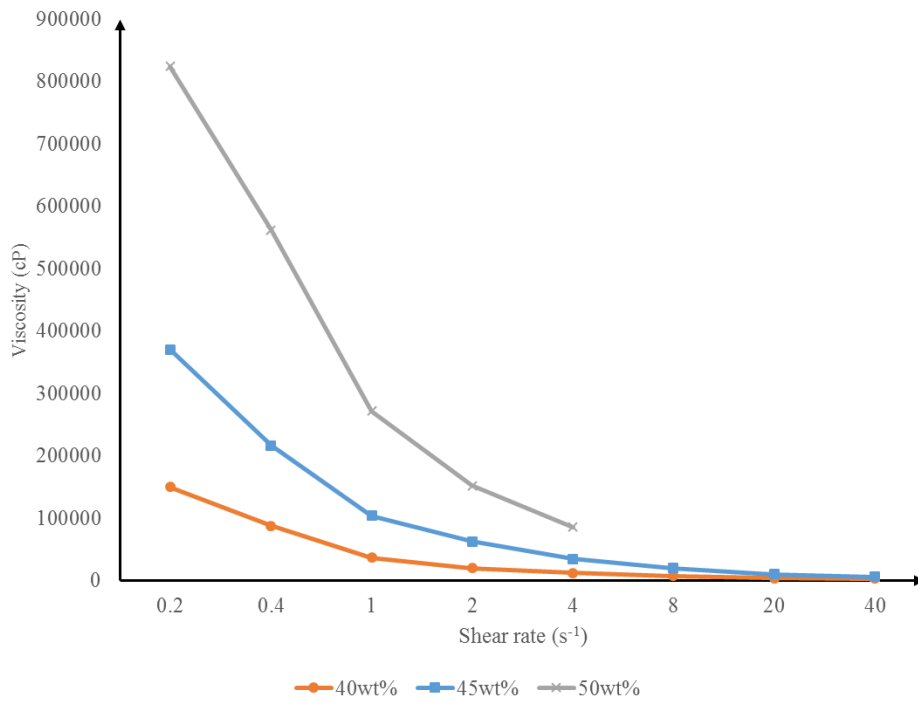


Figure 3.3 Viscosity of alumina slurries with different solid loadings

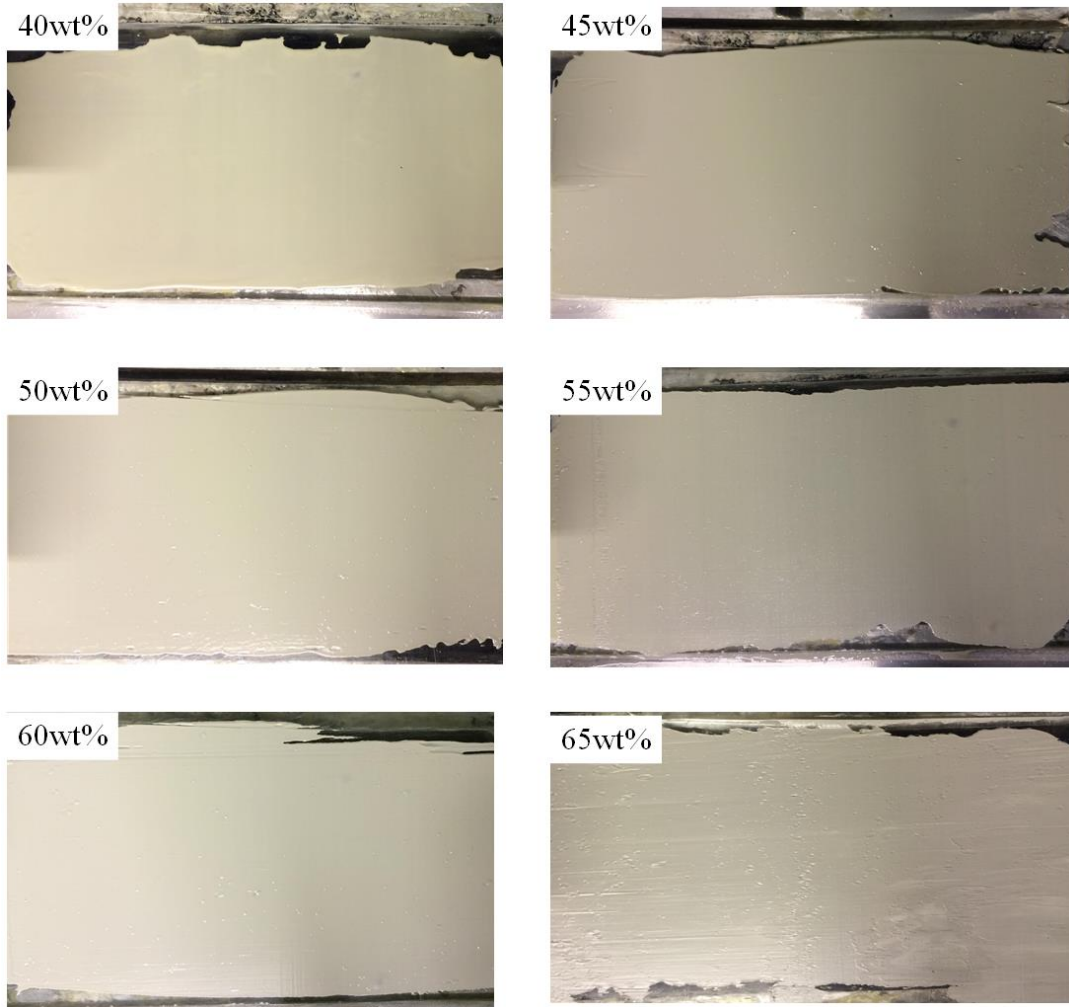


Figure 3.4 As-cast slurry tapes with different solid loadings, doctor blade height is 200 μ m

In a tape casting process, the viscosity of the slurries can't be large in order to achieve a smooth and homogeneous surface of a tape. For this reason, conventional tape casting process usually limits the viscosity of the suspensions in the range of 0.8-1.2Pa•s at the shear rate imposed by the blade during casting (Chartier, 1999). When tape casting is applied into our projection-based SLA method, the surface quality of a cast layer is not as important as that in the manufacturing of ceramic tapes, since a new layer for the fabrication is formed by pressing the cast tape into a thinner layer. Even if the original cast layer has a poor surface quality, the quality of the final layer can be improved after pressing the cast tape. Therefore, a bigger viscosity is allowed in the tape casting of our AM process as long as a solid slurry layer can be

obtained without void islands in it. Figure 3.4 illustrates the layer recoating results of different highly loaded slurries via the tape casting system in our process. The solid loadings that can yield a relatively uniform layer without pores can be used in the final fabrication. According to figure 3.3 and 3.4, the 65wt% loaded slurry that can be successfully coated by the doctor blade into thin layers (e.g.~200 μm) has a low shear viscosity >500Pa•s.

The rheological behaviors of ceramic slurries are determined by the type and concentration of powder, organic additives and solvent (Olhero, 2005). Many mathematical models have been developed to describe the dependence of rheological behaviors of ceramic slurry on solid loading, shear rate, etc., such as power-law model (Lewis, 1996), Herschel-Bulkley model (Hinczewski, 1998^b; Chartier, 1997), Casson model (Gurauskis, 2007; Bitterlich, 2002; Zupancic, 1998; Song, 2004).

The Herschel-Bulkley model is expressed in a form of

$$\tau = \tau_0 + K \cdot \dot{\gamma}^n \quad (3.4)$$

where τ is the shear stress (N/m²), $\dot{\gamma}$ is the shear rate (s⁻¹), τ_0 is the yield stress (N/m²), n is the shear rate exponent and K is a constant. For slurries that exhibit shear thinning behavior, n<1.

The Casson model is given as:

$$\sqrt{\tau} = \sqrt{\tau_0} + K\sqrt{\dot{\gamma}} \quad (3.5)$$

The influence of solid loading on the viscosity have been extensively studied by researchers. A simple model of relative viscosity η_r (Lewis, 1996) described that η_r is power-law dependent on the ceramic volume fraction:

$$\eta_r = \frac{\eta_{app,0}}{\eta_{soln}} = K\Phi^n \quad (3.6)$$

where $\eta_{app,0}$ is the low shear Newtonian viscosity, η_{soln} is the viscosity of the solution, i.e. resin and dilute.

A well-known Krieger-Dougherty model (Krieger, 1959) gives the relative viscosity dependence of hard sphere system on volume fraction as:

$$\eta_r = \left(1 - \frac{\Phi}{\Phi_m}\right)^{-[\eta]\Phi_m} \quad (3.7)$$

In the equation, Φ_m is the maximum volume fraction and $[\eta]$ is the intrinsic viscosity ($[\eta]=2.5$ for sphere particle). As for soft sphere systems (Bergström, 1996; Lewis, 2000), such as the slurry used in our process, scaled volume fraction Φ_{eff} for spherical system can be applied in the Krieger-Dougherty model by following:

$$\Phi_{eff} = \Phi \left(1 + \frac{\Delta}{a}\right)^3 \quad (3.8)$$

in which Δ is the adlayer thickness around each particle (a layer thickness of 10nm is used in many reports), a is the particle radius.

No matter which model is chosen, the parameters in the above equations are calculated by a mathematical fit to experimental data such that any viscosity of a specific slurry at a given shear rate and solid loading can be predicted.

Due to the limited shear rate range of our viscometer, we can use the limiting form of the Cross model (Bergström, 1996) to predict the viscosity at the high shear rates. In the high shear rate limit, the Cross model takes the form:

$$\eta_r = \eta_\infty + \frac{\eta_0 - \eta_\infty}{b\dot{\gamma}^p} \quad (3.9)$$

which has three parameters, namely η_∞ , $\frac{\eta_0 - \eta_\infty}{b}$ and p . To fit the high shear rate viscosity, set $p=0.6$.

To obtain the viscosity of slurry with higher solid loadings, we can apply a modified Krieger-Dougherty model presented in (Bergström, 1996).

$$\eta_r = \left(1 - \frac{\Phi}{\Phi_m}\right)^{-n} \quad (3.10)$$

which is a two-parameter empirical equation. With the slurry viscosity results of different concentrations at the same shear rate, the viscosity of a higher solid loading of alumina can be estimated at the corresponding shear rate.

3.4 Bottom-up projection for Stereolithography

High solid loadings in ceramic composite slurry are desired such that good physical properties can be obtained after the fabricated green parts are sintered. However, as discussed in chapter 1, recoating ceramic composite slurry with high viscosity is difficult in the top-down projection based SLA process. To address the challenges, we developed a tape-casting-integrated SLA process based on the bottom-up projection approach, which can build polymer-ceramic composite green parts using slurries with high solid loadings.

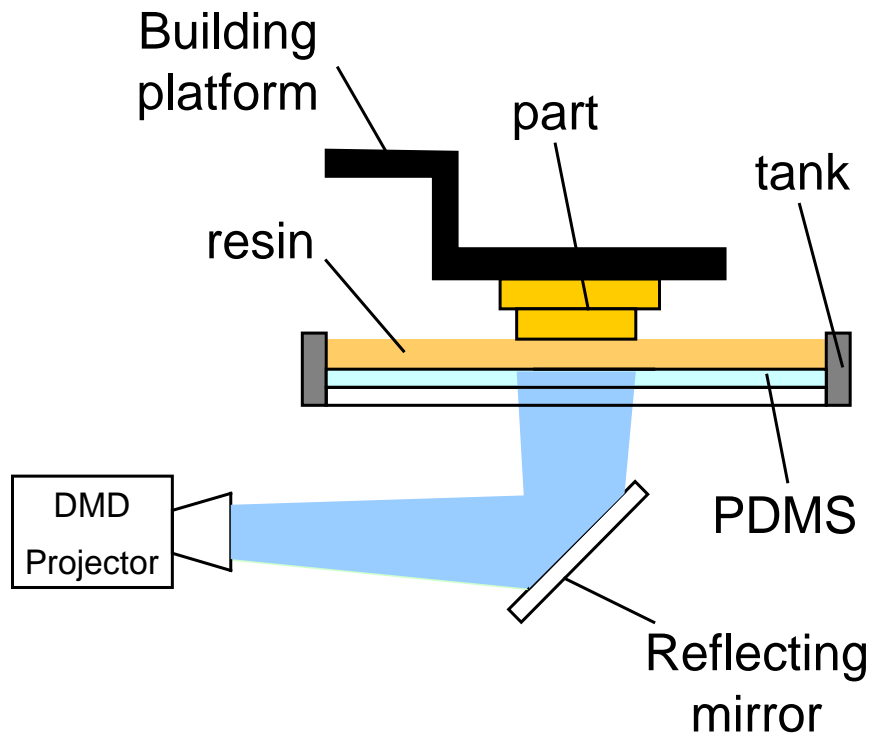


Figure 3.5 Projection-based SLA process using the bottom-up projection method

Different from the top-down projection based approach as shown in figure 1.7, the bottom-up projection based SLA process is shown in figure 3.5. Mask images are projected through a transparent resin

tank to cure layers that are hung upside-down on the building platform. In addition, the bottom of the resin tank is coated with materials such as PDMS or Teflon to facilitate the separation of newly cured layers (Zhou, 2013). The benefits of the bottom-up projection based approach include:

(1) Only a small amount of building material is needed. It is not required to have a tank filled with slurry during the fabrication process. Hence the problem of slurry sitting in the tank for a long time can be overcome, and the damage of tiny features caused by the viscous slurry can also be avoided.

(2) The recoating of ultrathin layers is enabled. In the bottom-up projection based system, a new layer is sandwiched between previously cured layers and the bottom of the tank. Hence its thickness can be accurately controlled by adjusting the height of the building platform.

3.5 Tape-casting integrated with Bottom-up Projection based Stereolithography

Tape casting is a widely used ceramic manufacturing process that can produce thin ceramic tapes from various types of slurries and has been applied in manufacturing a variety of ceramic products, including solid oxide fuel cells (SOFCs), ceramic substrates, etc. Initially developed by Glenn Howatt during World War II (Mistler, 2000), tape casting is also known as doctor blading and knife coating. A typical tape casting process starts with a slurry consisting of ceramic powders, binder, solvent, surfactant, etc. A wet tape is formed by casting the slurry onto a flat surface, or film collector, by a doctor blade. Heated air is supplied to remove the solvent in the wet tape and obtain dried tape. For ceramic tapes, a firing process is required after the drying to remove the binder and densify the tapes. Figure 3.6b shows an automatic ceramic film casting coater. Its capability of coating uniform thin layers provides an approach for recoating viscous slurry in the ceramic composite SLA process.

Figure 3.7 shows the main components of the developed tape-casting-integrated projection-based SLA process. The figure shows the moment when an initial layer is cured and has not been detached yet.

The developed system consists of a Z stage, a Digital Micro-Mirror Device (DMD) based projection system, and a tape casting module. The tape casting module is made up of a film collector and a linear guide to move it in the X axis. The film collector is mainly an embedded glass sheet coated with a PDMS or Teflon film.

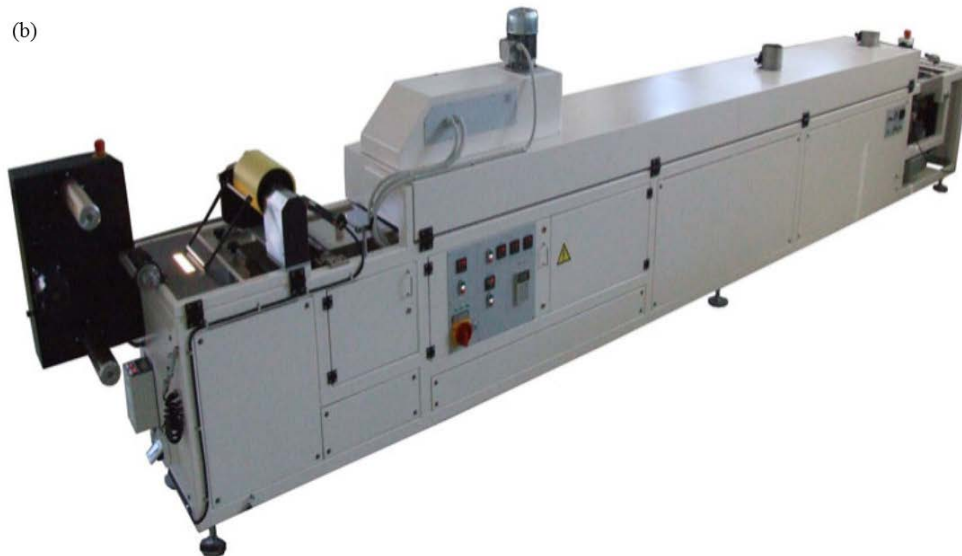
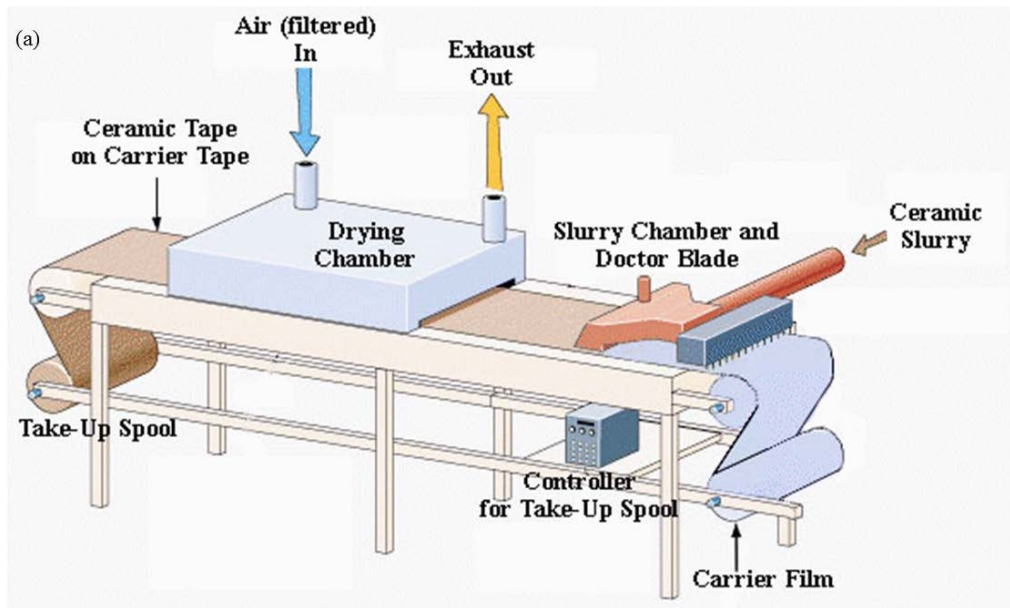


Figure 3.6 (a) Schematic of typical tape caster (Diamond & Related Materials Laboratory n.d.) (b)

An automatic tape casting coater (Haikutech n.d.)

In our previous research on multi-material fabrication (Zhou, 2013), it is shown the separation force is considerably large when the Z stage is directly pulled up even with the coated PDMS film on the film collector. In addition, the separation force will significantly increase when the resin viscosity is increased. Hence, for viscous ceramic composite slurry that is used in the ceramic composite SLA process, the separation force will be large. If such a separation force is larger than the bonding force between the newly cured layer and the previously cured layers, the newly cured layer will be detached from the part and the building process will fail. To facilitate the layer separation, a sliding mechanism based on a two-channel design is presented in (Zhou, 2013). Compared to the separation force during a direct pulling-up, the shearing force during a sliding motion along the X axis is much smaller. The two-channel design as discussed in (Zhou, 2013) is also used in our tape-casting-integrated SLA process.

As shown in figure 3.7, the film collector can be moved along the X -axis, and the Z stage can be moved along the Z -axis. The height of a doctor blade is set to be δ_{Blade} . Note that δ_{Blade} is usually much larger than the layer thickness δ (i.e. $\delta_{Blade} > \delta$). The film collector is divided into two channels, one has the PDMS coating and another one has not. The mask images controlled by a DMD are only projected onto the channel that has the PDMS coating.

After a layer is cured, the Z stage first moves up for a small distance ($d_{release}$) to release the stress in the cured layer generated in the polymerization process. Right after the lift-up, the film collector slides from left to right with a speed of V_s for a distance d_{feed} . As discussed in (Zhou, 2013), the force in this sliding movement is relatively small since a thin oxygen-aided inhibition layer ($\sim 2.5 \mu\text{m}$) is formed near the PDMS film, which can provide a non-polymerized lubricating layer for easy sliding. As soon as the cured layer slides to the channel that has no PDMS, the vacuum between the cured layers and the film has been broken. The built layers thus can be detached from the film collector. The peak separation force based on the sliding mechanism is only 4-5% of that based on the direct pulling-up approach (Zhou, 2013).

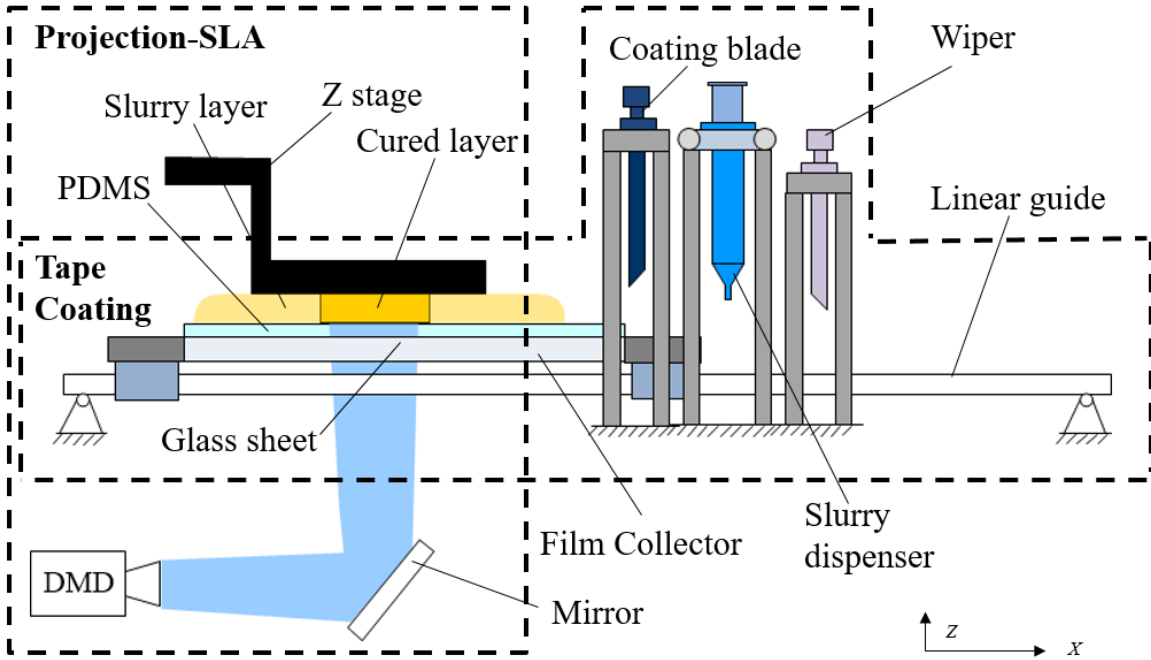


Figure 3.7 Green part fabrication using tape casting integrated SLA

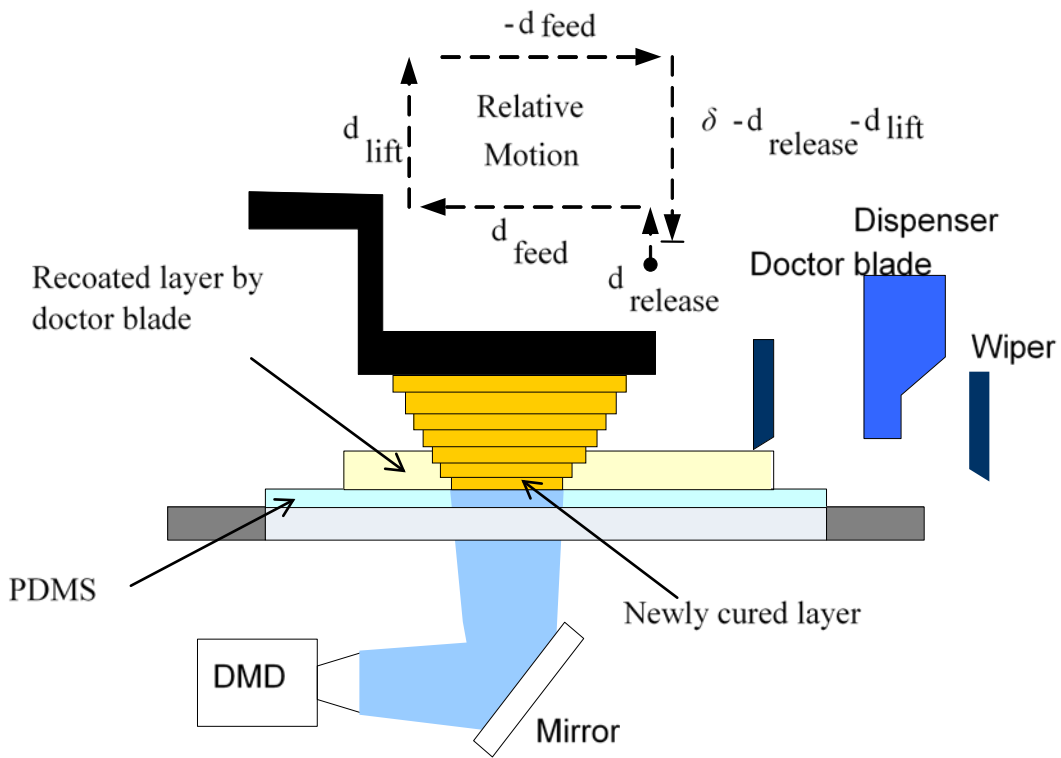


Figure 3.8 Process planning for the tape casting integrated SLA process

The film collector moves all the way to the right under the dispenser to add new slurry. Before the film collector moves back, the building platform is moved up for a distance d_{lift} (0.5~1mm) to allow the slurry that is spread by the blade to be conveyed underneath the built layers. After the film collector returns with a speed of v_r , the Z stage moves the building platform down for a distance $\delta - d_{release} - d_{lift}$. Thus a gap of one-layer thickness is left above the PDMS film. Hence, based on a thick layer that is formed by the tape casting module (i.e. δ_{Blade}), the designed motion of the platform can further form a thinner layer of slurry (i.e. δ). Even for rather viscous slurry, our system can achieve a layer thickness δ as small as 10 μ m. Such ultrathin layers are difficult to be formed if only the doctor-blade-based tape casting process is used.

3.6 Prototype Design and Process Planning

A testbed including both hardware and software systems have been built to demonstrate the presented polymer-ceramic composite fabrication process.

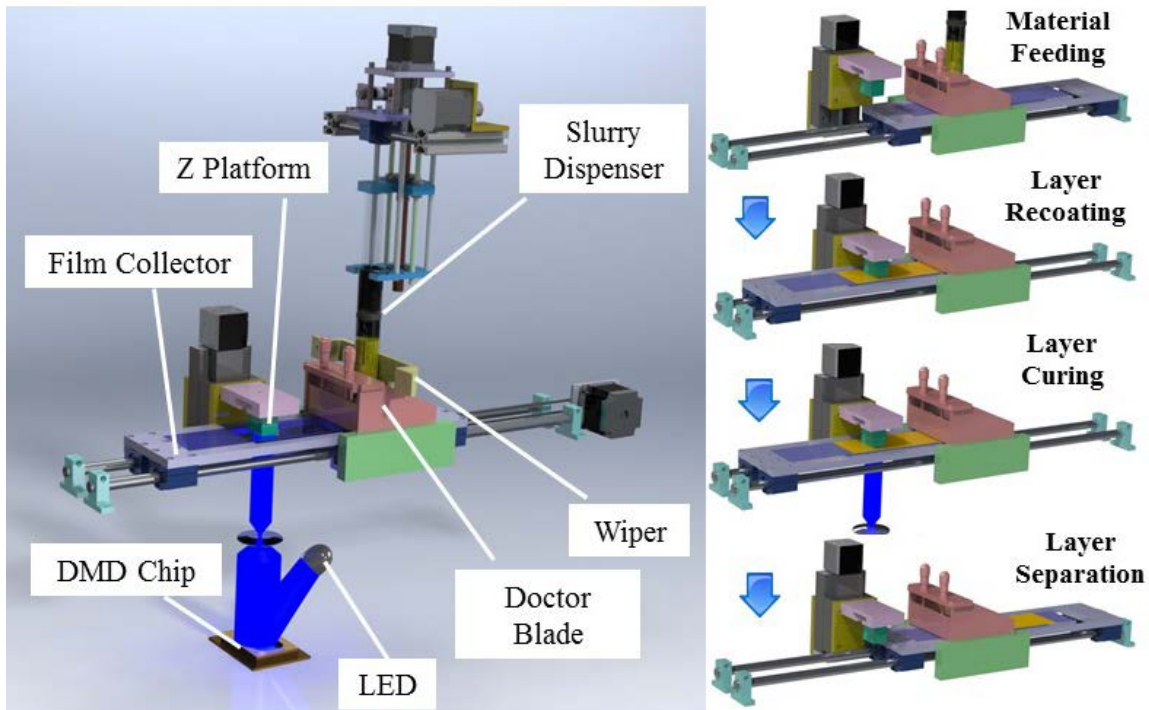


Figure 3.9 Fabrication machine of projection-based SLA integrated with tape casting

The hardware system design is shown in figure 3.9. A motorized micro positioning linear stage (Danaher Corporation, Washington, D.C., US) is used to drive the building platform in the Z axis. A clear glass sheet (3/32" or 2.38mm thickness) coated with PDMS (Sylgard 184, Dow Corning) is embedded in a film collector. The film collector moves along a linear guide through four linear ball bearing slide bushings. A belt-pulley mechanism was used to drive the film collector in the X axis. A micrometer adjustable film applicator (MTI Corporation, Richmond, CA) is used to conduct material spreading. Its blade height can be adjusted by a micrometer head with a resolution of 10 μ m. Hence the ceramic composite suspension layer that is recoated can be well controlled to be larger than the set layer thickness. A second blade is mounted at the right of the film doctor blade but in the opposite direction in order to recollect the slurry on the substrate.

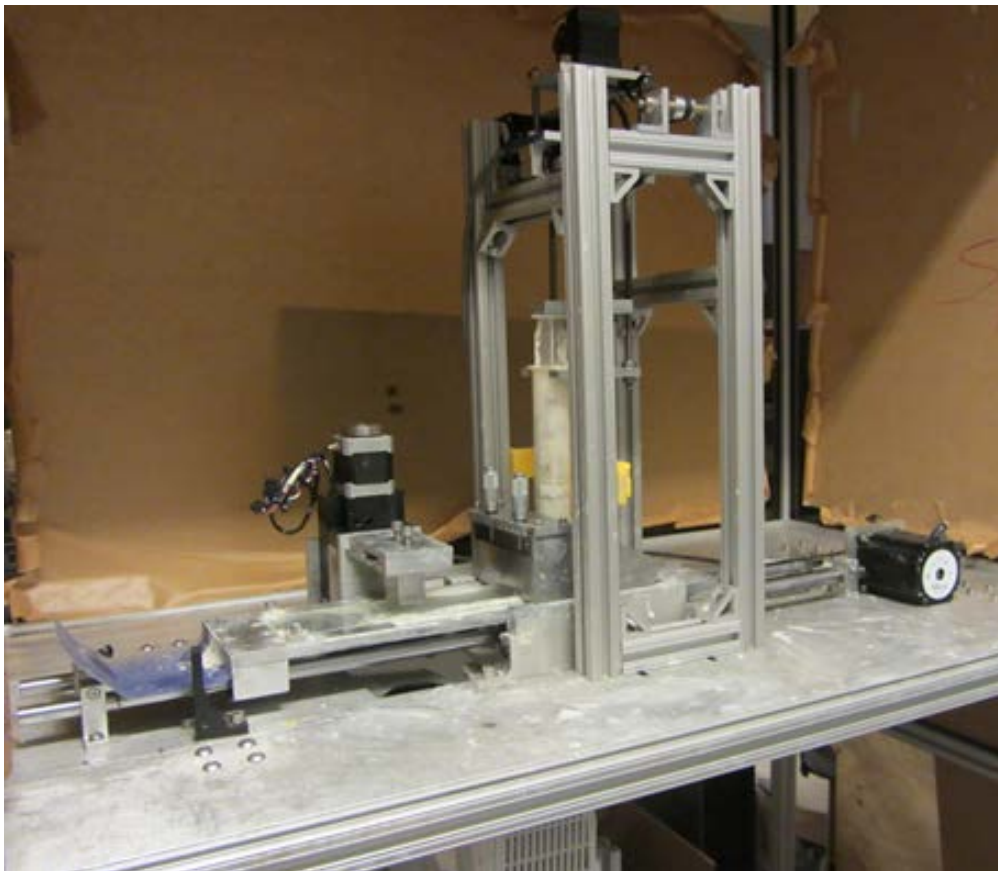


Figure 3.10 A prototype system using the tape casting integrated SLA process

A 60cc syringe is fixed behind the blades to dispense a certain amount of ceramic composite slurry after each motion cycle. The syringe plunger is driven by a linear actuator (Eastern Air Devices, Dover,NH). The dispensing is performed by moving the syringe along the y axis through a belt-pulley mechanism, while pushing the plunger down for a controlled distance at the same time. A prototype machine is shown in figure 3.10.

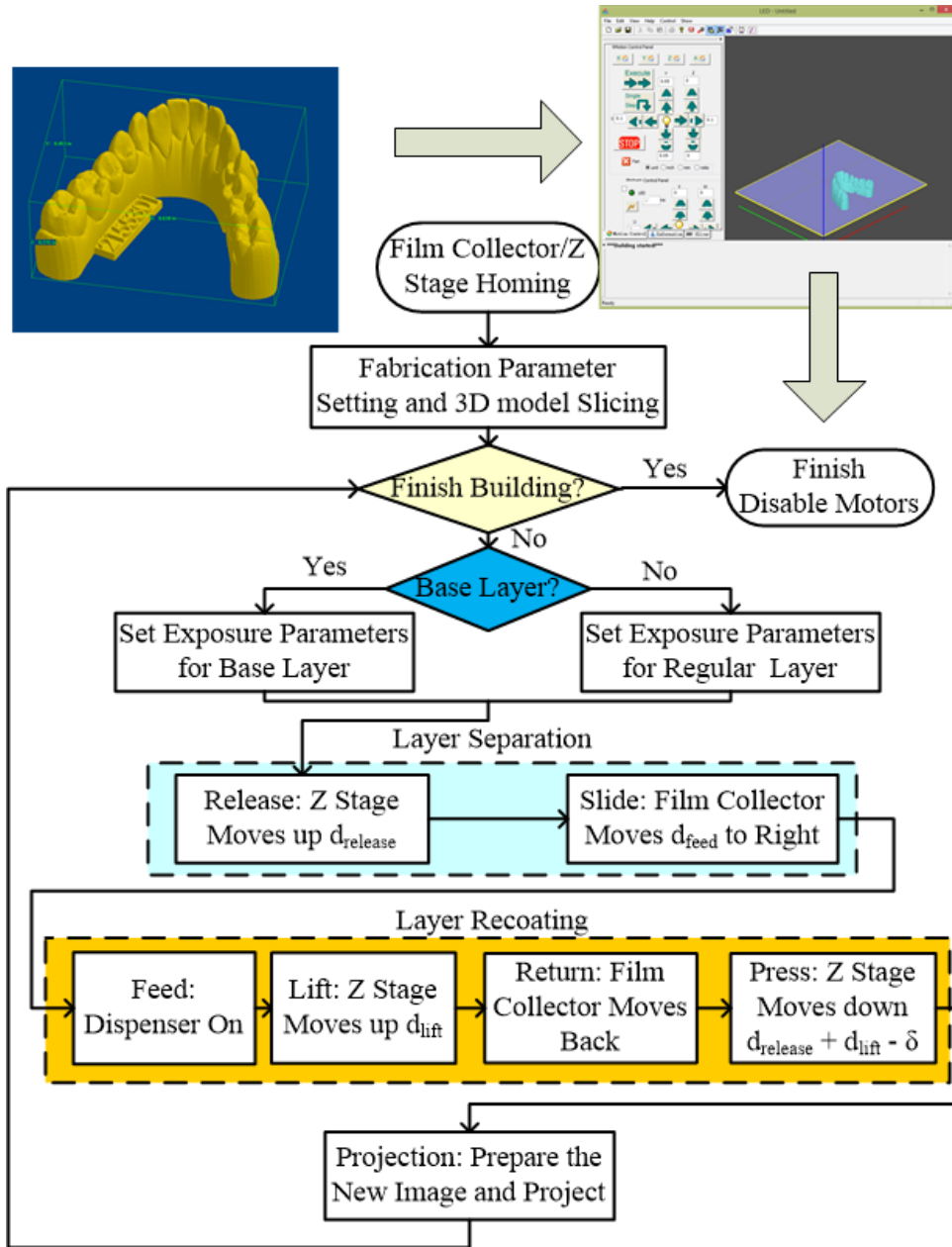


Figure 3.11 Flow chart of the tape-casting-integrated SLA process

A process control software system has been developed using Microsoft Visual C++. Figure 3.11 shows the graphical user interface (GUI) of the developed software system. The software system can slice a given CAD model and dynamically output mask images to the designed projection system. The projection image size of the prototype system is designed to be 43.18mm × 24.384mm. The resolution of the DMD chip (Texas Instrument, Dallas, TX) is 1280 × 720. The output light intensity of the projector is ~31.6mW/cm². The software system can also send motion control commands to a 4-axis motion controller (Dynomotion Inc, Calabasas, CA).

The planned process is also given in the figure 3.11. Before a 3D model starts to be fabricated, a base is first built to compensate the contact clearance between the Z platform and the surface of the film collector. The light exposure time for base layers is usually larger than that for regular layers, unless different materials are used in base and regular layers. Layer separation and layer recoating are performed sequentially right after process parameters are initialized. Main parameters include light exposure time for base and regular layers, base layer thickness, doctor blade height, recoating speed, pressing speed, minimum sliding height, sliding speed, dispensing amount, etc. In the next chapter, all these process parameters are analyzed and parameter design methods are discussed.

3.7 Summary

In this chapter, we presented a modified bottom-up projection based SLA process by integrating with tape casting. The method can be used to process polymer-based composite materials including ceramic-polymer composites and provides an indirect route for the processing of ceramic components.

Serving as the feedstock material for the presented process, ceramic composite slurry is prepared by mixing ceramic powder, photosensitive resin and other organic additives. Four steps are involved in the slurry preparation, including powder deagglomeration, premixing, ball milling and degassing.

Different ceramic powders were introduced and their slurries were prepared. The analysis of their curing characteristics indicates the great impact of factors, including incident light, powder type, solid loading, liquid resin, etc., on the cure depth and width of the final slurry materials.

Rheological properties of the ceramic slurry were also experimentally and analytically studied, using alumina slurry as an example. The viscosity of 65wt% solid loaded slurries with different dilute concentrations was first measured. Alumina slurries with different solid loadings were then studied by both viscosity measurement and layer recoating. It suggests that a solid loading of 65wt% can achieve the best layer recoating without adding any dilute solvent. Different mathematical models were presented to study the dependence of the viscosity on shear rate and solid loading. The limiting form of the Cross model and a modified Krieger-Dougherty model can be used to predict the viscosity of different solid loadings at the high shear rate.

The tape-casting-integrated SLA process was presented for fabricating viscous ceramic slurries. Uniform ultrathin layers can be recoated by integrating the bottom-up projection approach and the ceramic tape casting process. A doctor blade first spreads viscous slurry into thick layers. Platform pressing motion is then used to achieve a desired layer thickness that can be much smaller than the blade-recoated layer thickness. The design can also facilitate the layer separation after each layer is fabricated. Benefits of using the bottom-up projection and tape-casting methods were analyzed for the ceramic slurry based SLA process. An experimental prototype system has been developed to test the capability of the presented ceramic composite fabrication process.

Chapter 4 Process Modeling: Parameter Optimization for Slurry-based SLA process

4.1 Overview

In chapter 3, we presented an additive manufacturing (AM) process for fabricating viscous composite slurry by integrating a projection-based stereolithography (SLA) process with tape casting technique. Composite slurries are prepared by mixing filler particles with photocurable resin. When different filler powders are added, the slurry will exhibit distinct curing and rheological behaviors. Since process parameters can be significantly influenced by these behaviors of the materials, the dependence of process parameters on the material properties have to be studied in order to successfully fabricate a composite component. In this chapter, experimental and analytical methods (Song, 2015) were presented for the design of each process parameter, including doctor blade height, recoating speed, layer pressing speed, separation speed, etc. Two test cases were fabricated to demonstrate the capability of our process in the fabrication of composites, including glass reinforced composites and dielectric polymer-ceramic composites.

4.2 Layer recoating via tape casting

4.2.1 Blade height δ_{Blade}

A fluid flow process in a traditional tape casting system (figure 4.1a) is a combination of pressure flow and Couette (drag) flow in the parallel channel of a casting head (Chou, 1987; Tok, 2000). For the pressure flow, its flow rate results from an applied pressure, i.e. pressure p in figure 4.1a, while the Couette flow is caused by the drag force acting on the fluid by the doctor blade.

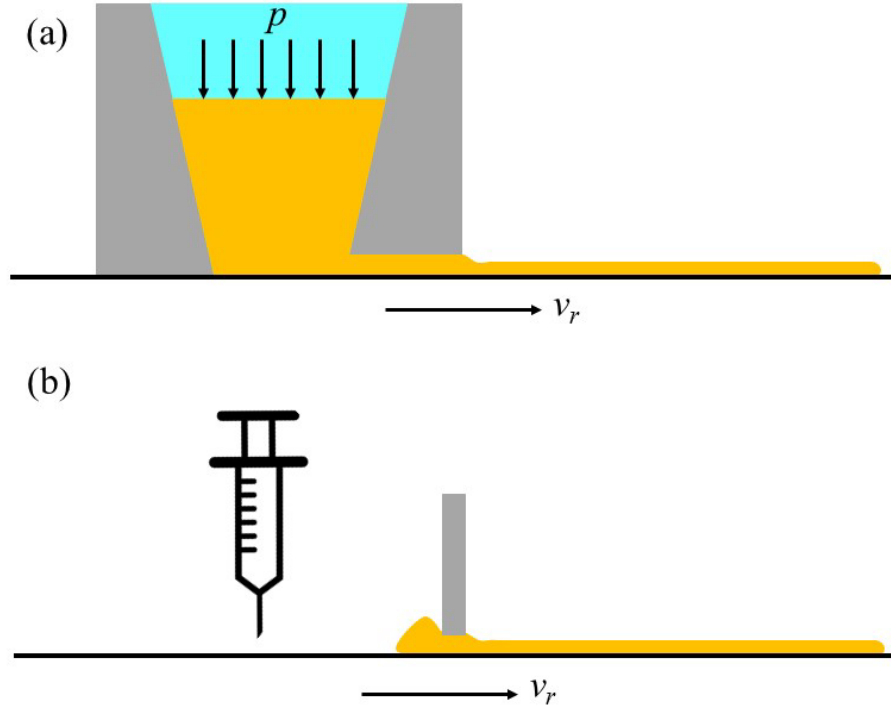


Figure 4.1 Tape casting techniques (a) traditional process (b) used in our process

Unlike the traditional tape casting system, the one in our process only dispenses a small amount of slurry behind the doctor blade for each layer (see figure 4.1b). That means the pressure p in the dispensed slurry is very small. Since the viscosity of the materials is relatively high and the pressure in the dispensed slurry is negligible, the blade recoating procedure can be modeled a plane Couette flow pattern, as shown in figure 4.2, with the bottom plate moving at a constant speed of v_r relative to the blade.

For a steady and fully developed fluid flow with negligible gravity and z -direction flow, the Navier-Stokes equation can be simplified as follows (Joshi, 2002):

$$0 = -\frac{\partial p}{\partial x} + \eta \frac{\partial^2 u_x}{\partial y^2} \quad (4.1)$$

The boundary conditions follow:

$$u_x = v_r, \text{ at } y = 0;$$

$$u_x = 0, \text{ at } y = \delta_{Blade} \quad (4.2)$$

$$p = 0, \text{ at } x = 0 \text{ and } x = L$$

η is the viscosity. L is the length of the film collector. δ_{Blade} is the doctor blade height. By solving the Navier-Stokes equations under the given boundary conditions, one can get the velocity profile:

$$u_x = v_r \left(1 - \frac{y}{\delta_{Blade}}\right) \quad (4.3)$$

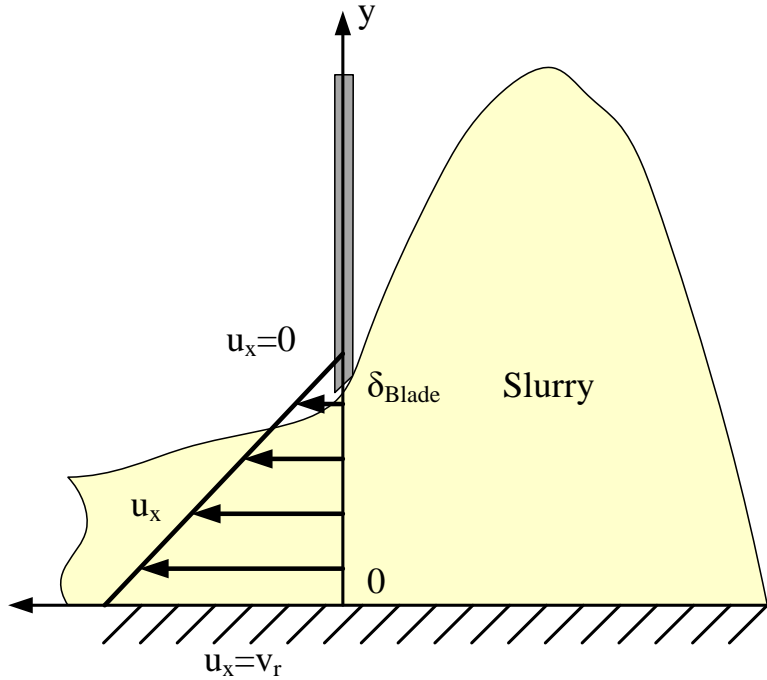


Figure 4.2 The velocity profile in the blade recoating

The volumetric flow rate of the fluid can be calculated as:

$$Q_c = \int_0^{\delta_{Blade}} u_x W dy = \frac{1}{2} \delta_{Blade} W v_r \quad (4.4)$$

where W is the doctor blade width.

It is known that the mass of the flow passing the doctor blade in a unit time is identical to the mass of the coated layer. So the following equation can be established:

$$\rho Q_c = \rho' \delta' W v_r \quad (4.5)$$

where ρ is the slurry density and ρ' is the density of the newly formed layer. A simplified equation of the thickness δ' of the wet recoated layer can thus be derived as:

$$\delta' = \frac{1}{2} \frac{\rho}{\rho'} \delta_{Blade} \quad (4.6)$$

If we consider the side flow occurring during the tape casting, which extend the width W to W' , we have:

$$W\delta' = W'\delta'' \quad (4.7)$$

and the thickness δ'' of the final recoated layer becomes:

$$\delta'' = \frac{W}{W'} \delta' = \frac{\alpha}{2} \frac{\rho}{\rho'} \delta_{Blade} \quad (4.8)$$

where $\alpha = \frac{W}{W'}$. To ensure tight interlayer bonding, δ'' must satisfy $\delta'' > \beta\delta$, where β is a safety factor to ensure two neighboring layers are tightly bonded ($\beta > 1$) and δ is the layer thickness chosen for the fabrication.

Hence the inequation for blade gap δ_{Blade} must hold:

$$\delta_{Blade} > \frac{2\beta\rho'\delta}{\alpha\rho} \quad (4.9)$$

4.2.2 Recoating speed v_r

Shear rate $\dot{\gamma}$ is calculated by recoating speed v_r and blade gap δ_{Blade} at $\dot{\gamma} = v_r \delta_{Blade}^{-1}$. Due to the shear thinning behavior of composite slurry, a higher shear rate will result in a lower viscosity of the slurry when the slurry passes the blade. Thus the sedimentation of filler particles in the recoated layer can be avoided, and a good homogeneity of the fabricated green parts can be achieved. With the same blade gap, a higher recoating speed v_r will generate a bigger shear rate $\dot{\gamma}$, and accordingly a smaller slurry viscosity.

4.2.3 Layer Pressing Speed v_p

As mentioned in chapter 3, conventional tape casting process requires the viscosity of the slurries in the range of 0.8-1.2Pa•s at the shear rate imposed by the blade during casting (Chartier 1999) in order to achieve a smooth and homogeneous surface of a tape. Composite slurry is too viscous to be spread by a doctor blade into a uniform layer which is thin enough (10~100 μm) to tightly bond with previous ones. In our process, a thick layer (100 ~ 500 μm) of slurry is first coated on the substrate by the tape casting system. Since the cast layer is much thicker than the required thickness, its surface doesn't have to be smooth as long as the building area is fully covered after casting. Therefore, a higher viscosity can thus be used in our process.

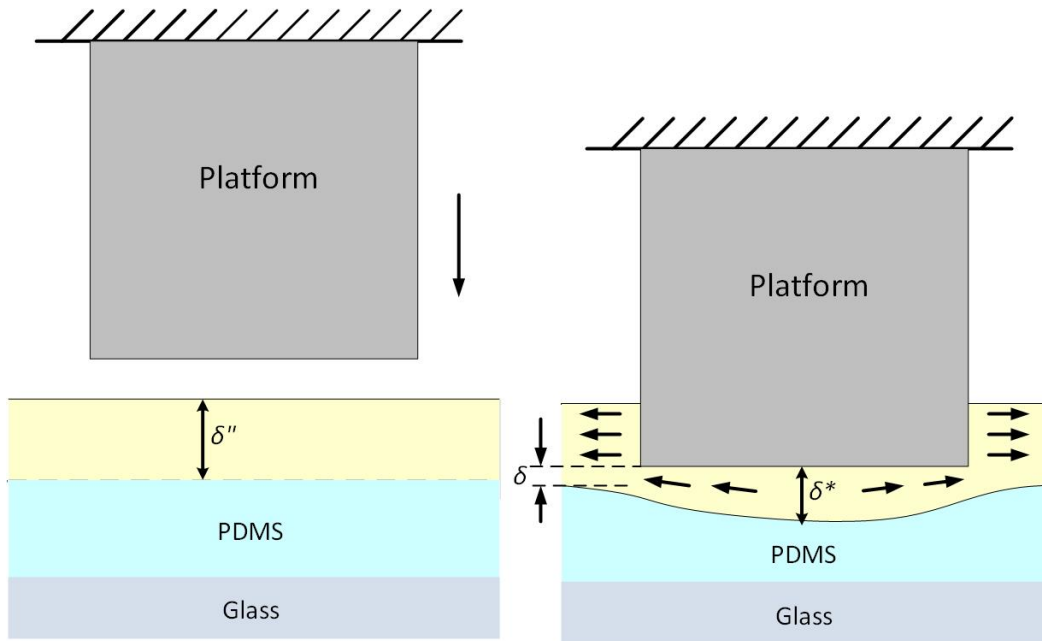


Figure 4.3 PDMS deformation leads to bigger recoated thickness

Based on this thick layer δ'' , a thinner thickness of the layer is then achieved by a pressing movement. Assume the required layer thickness is set to be δ , and cure depth of the tested material is C_d . As shown in figure 4.3, after a layer with a thickness of δ'' is cast, the platform is moved down towards the Polydimethylsiloxane (PDMS) until its distance to PDMS surface is equal to δ . Ideally extra slurry in the gap will flow outwards under the pressure of the platform, and a thin layer with the desired thickness δ can

be obtained between the platform and PDMS. However, due to the high viscosity of the slurry, the materials can't flow out freely, but push the substrate down and lead to the elastic deformation of the PDMS film. Therefore, the final slurry layer thickness, which is equal to the gap δ^* between the two surfaces, will be larger than the desired value δ and can result in the failure of the layer attachment to the previous layers.

The actual layer thickness depends on a lot of factors, including PDMS thickness, slurry viscosity, blade height, and pressing speed. Thanks to the shear thinning behavior of polymer-ceramic composite slurry, its viscosity will decrease as the shear rate increases. This allows for a way of controlling the actual layer thickness by selecting a proper pressing speed. To achieve the desired layer thickness δ , we investigated the relationship between the actual layer thickness δ^* and pressing speed v_p . In the experiments, all the other factors are fixed: the PDMS film has a thickness of 1mm, blade height is 250 μ m, and tested material is 70wt% Barium Titanate (BTO) with $d_{50} = 3\mu$ m.

The procedures of measuring recoating thickness are described in figure 4.4. Three layers of bases are built with pure resin to compensate for the clearance between the platform and PDMS surface. Resin has a cure depth as high as 1000 μ m which can ensure its attachment to the platform. After base layers are built, one layer of composite material is fabricated with the given pressing speed v_p . If this layer fails to attach to the base layers, the thickness δ^* of the recoated layer under the speed v_p must be bigger than cure depth C_d of the composite material. We then use C_d as the actual layer thickness with respect to the pressing speed v_p for simplicity. If the layer attaches to the bases successfully, the actual thickness δ^* should be smaller than cure depth C_d , and a wrapping method will be adopted to measure the thickness δ^* . That is, after the first layer of composite is built, all the fabricated layers, including the bases and the first layer, are covered by a plastic wrap (thickness $\sim 10\mu$ m). The fabrication of the second composite layer is then continued with the same pressing speed v_p . Due to the existence of the plastic wrap, the second layer will not attach to the previous layers and can be measured separately by a length gauge (Heidenhain, Schaumburg, IL, US). The actual layer thickness δ^* is equal to the sum of the thickness of the plastic wrap and that of the second layer.

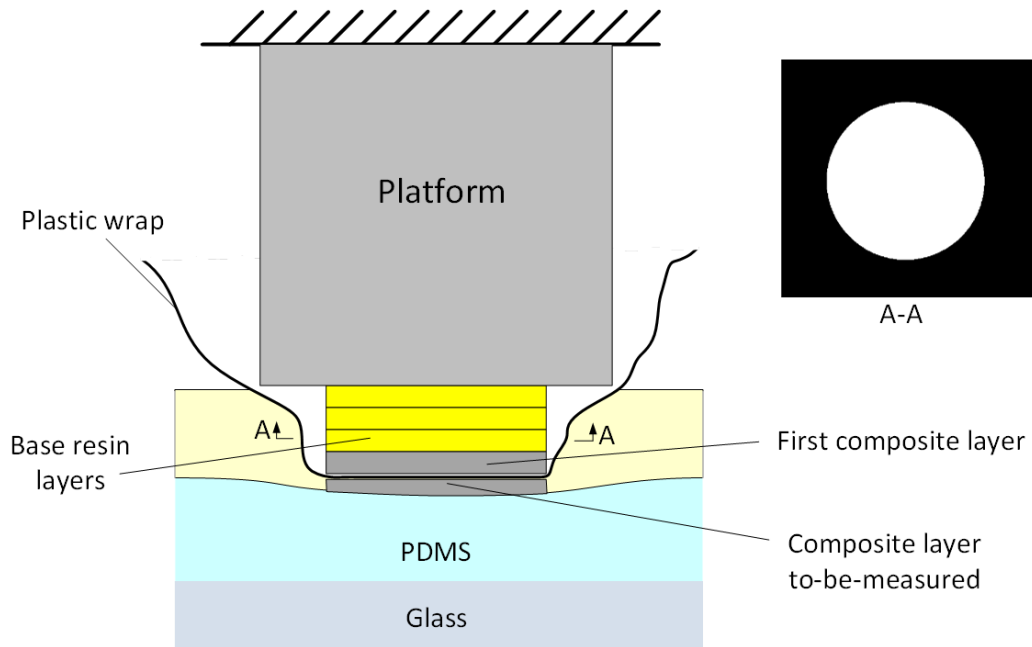


Figure 4.4 Measurement of recoated thickness

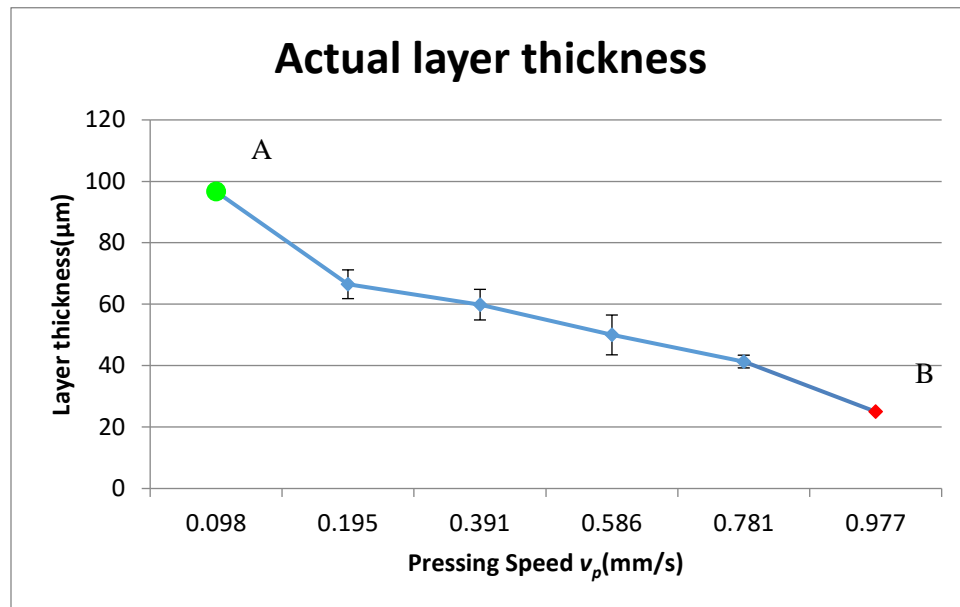


Figure 4.5 Actual layer thickness versus pressing speed. Note: (1) The cured layer at point A failed to attach to the platform, so the actual layer thickness is larger than the measured thickness. (2) The cured layer

The measurement results are shown in figure 4.5. It can be seen that the actual layer thickness decreases as the pressing speed increases until a minimum thickness (equal to designed layer thickness) is obtained. The curve is measured with fixed blade height, PDMS thickness and material viscosity. If different blade height, PDMS coating or materials are used, the curve should be re-measured and pressing speed can be accordingly identified based on the curve to minimize the actual layer thickness.

4.3 Layer separation via sliding mechanism

Sliding speed v_s . After a layer is cured, the platform goes up for a small distance from the PDMS. Then the film collector moves in the X axis with a speed v_s to detach the newly cured layer from the PDMS film. Suppose a cylindrical shape is being fabricated, whose diameter is d and the current building height is L . As shown in figure 4.6, when the part slides from left to right, the portion of the cylinder immersed in the slurry layer will experience a drag force F in the slurry moving direction as the average force q ($q = \frac{F}{\delta''}$).

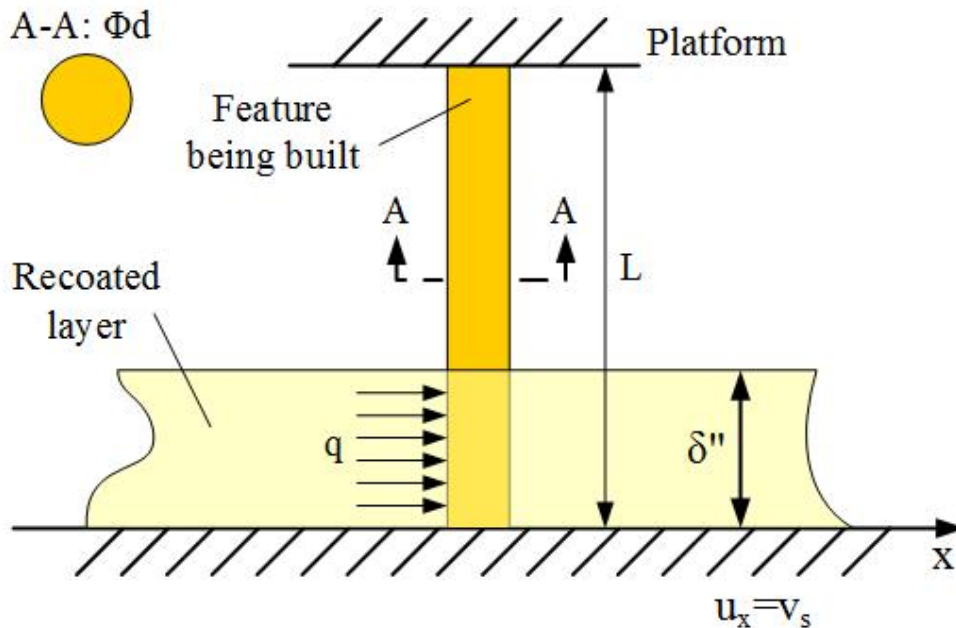


Figure 4.6 Drag force during the layer detachment

Based on the drag force equation, we know:

$$F = \frac{1}{2} \rho v_s^2 C_D A \quad (4.10)$$

where ρ is the mass density of the slurry; C_D is the drag coefficient that is related to Reynolds number Re of the slurry and can be identified by experiments; A is the reference area. In our case, $A = \frac{\pi d \delta''}{2}$.

Substitute equation (4.10) into the flexure formula of a cylinder $\sigma_{max} = \frac{Mc}{I}$ ($I = \frac{\pi d^4}{64}$ is the area moment of inertia for solid circular cross section), the maximal normal stress σ can be derived as:

$$\sigma = \frac{8\rho v_s^2 C_D \delta'' L}{d^2} < [\sigma] \quad (4.11)$$

Hence,

$$0 < v_s < \sqrt{\frac{[\sigma] d^2}{8\rho C_D \delta'' L}} \quad (4.12)$$

The material used in our tests has a minimal bending stress $[\sigma] = 65\text{MPa}$.

4.4 Base layers for initial gap compensation

In order to enable the initial layer to attach to the building platform, the platform plane has to be strictly parallel to the substrate. In practice, exact alignment between the two surfaces can't be guaranteed due to manufacturing and assembly errors. For composite slurry with relatively high cure depth (e.g. 200 μm), this error can be ignored, since the clearance can be filled up after the first layer is built. However, for composite slurry with smaller cure depth (e.g. 50 μm), even a small clearance between the two planes (e.g. 20 μm) will lead to unsuccessful attachment of the initial layers to the building platform. Furthermore, directly removing a fabricated part from the building platform could cause defects at the bottom of the part. As a result of the bottom defects, crack propagation will occur during the post processing.

For these reasons, we first build 5~10 layers of bases using pure photosensitive resin. This material, serving as the base layers, has a lower melting point compared to the composite layers, such that the base can be melted in the post processing without contaminating the final parts. By this base coating method, a

part can thus tightly stick to the building platform, even with a small cure depth (e.g. 50 μm), and can also be easily removed from the platform after the fabrication is finished without damaging the bottom surface of the green part.

4.5 Material Feeding

4.5.1 Moving distance of dispenser and its plunger

At the beginning of fabrication, the film substrate is moved to the dispenser, which drops a slurry line onto the substrate surface. The doctor blade will then spread the slurry line out and form a thin slurry film with a thickness of δ'' , as derived in equation (4.8). Assume $\alpha=1$ and the density before and after the casting is the same, hence $\delta'' = \frac{\delta_{blade}}{2}$. After one layer is fabricated, only a small portion of the recoated slurry layer is cured, and all the other slurries are left on the substrate. In the next cycle, the film collector moves to a wiper instead of the dispenser, to sweep the remaining materials to the leftmost end of the substrate. The same wiping process will be done in the following cycles until the recoated slurry can't cover the projection region. Assume the inner diameter of the dispenser chamber is D , the inner diameter of its nozzle is d (refer to figure 4.7). The projection region is designed to be L by W , based on the bounding box of the 3D model. Then we have the equation for the moving distance of the dispenser:

$$W_{ext} = W \quad (4.13)$$

The moving distance h_{ext} of the dispenser plunger for each material feeding can be calculated by

$$S \cdot \frac{\delta_{blade}}{2} = \left(\frac{D}{2}\right)^2 \pi h_{ext} \quad (4.14)$$

where S is the length of the recoating range. The left hand side of the equation means the volume of the recoated slurry, and the right hand size is the volume of the extruded material. So extrusion distance is decided by:

$$h_{ext} = \frac{2S\delta_{blade}}{D^2\pi} \quad (4.15)$$

Assume the projection region is positioned at the center of the recoating range. For the maximum number of layers n_{max} that material can fill up without new material dispensed, the equation should hold:

$$\frac{D^2}{4}\pi \cdot h_{ext} - n_{max}WL\frac{\delta_{blade}}{2} = \frac{\delta_{blade}}{2}W_{ext}\frac{S+L}{2} \quad (4.16)$$

Then the number of layers recoated by wiper should satisfy:

$$1 \leq n \leq n_{max} = \frac{D^2\pi h_{ext} - \delta_{blade}W_{ext}(S+L)}{2WL\delta_{blade}} \quad (4.17)$$

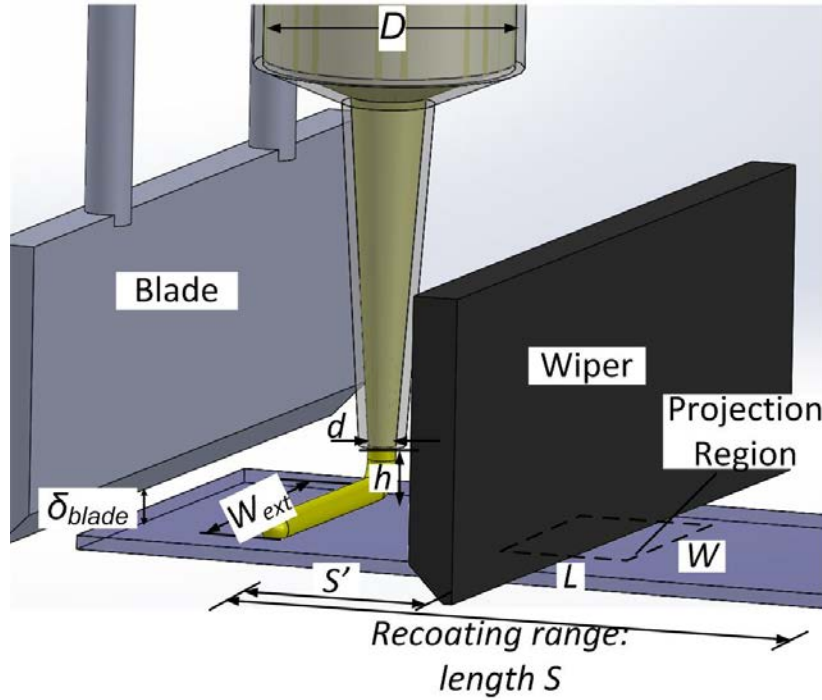


Figure 4.7 Parameters in the dispensing system

4.5.2 Nozzle height

The distance between the nozzle tip of the dispenser and the substrate should also be controlled within a suitable range, such that the cross section of the extruded slurry lines can maintain an arch shape with a contact angle larger than 45° . As a consequence of the shear thinning behavior, the slurry will not spread

out after it leaves the nozzle. To avoid a squeezing effect (Wang, 2005), i.e. the slurry is forced to flow beyond the volume formed by the nozzle height, the nozzle diameter and the distance the nozzle travelled in unit time, the nozzle height h must be bigger than the critical nozzle height h_c , and

$$h_c = \frac{v_{plunger} \pi \frac{D^2}{4}}{v_{disp} d} = \frac{\pi D^2 h_{ext}}{4 d W_{ext}} \quad (4.18)$$

Then the nozzle height should follow:

$$h_c < h < d \quad (4.19)$$

4.6 Case Study I: fabrication of glass reinforced composite components

The capability of the slurry-based SLA process in fabricating viscous materials extends the breadth of material selection. More materials, especially polymer-based composites, can be chosen in the SLA process other than liquid resin. Low cost solid powders, such as glass fibers, carbon fibers, etc., can be employed as a reinforcing phase in the resin matrix. The added reinforcing fillers can not only improve the mechanical properties of the final parts, but also reduce the required amount of liquid resin in the process, and consequently reduce the cost on the materials which are usually rather expensive.

Table 4.1 Process parameters used in the fabrication process for glass reinforced composite

| | Curing time for base/normal layers (s) | Layer thickness (μm) | Blade gap δ_{blade} (μm) | Recoating speed v_r (m/s) | Pressing speed v_p (mm/s) | Sliding speed v_s (m/s) |
|-------|----------------------------------------------|-----------------------------------------|----------------------------------------------------|-----------------------------------|-----------------------------------|---------------------------------|
| Glass | 2/1 | 100 | 400 | 0.0254 | 0.078 | 0.0254 |

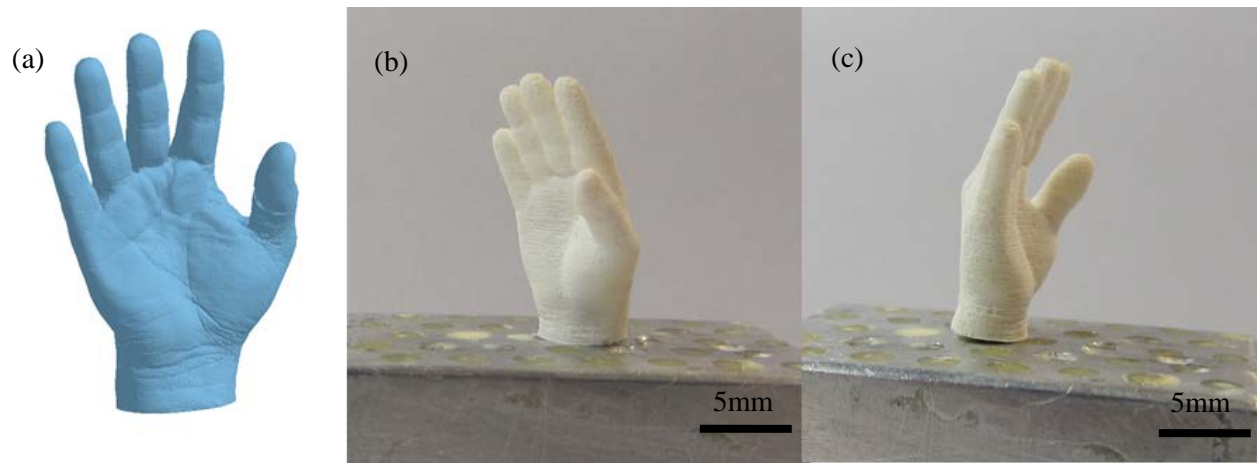


Figure 4.8 A “Hand” model fabricated with glass reinforced composite (a) CAD model (b-c) Two views of the built object

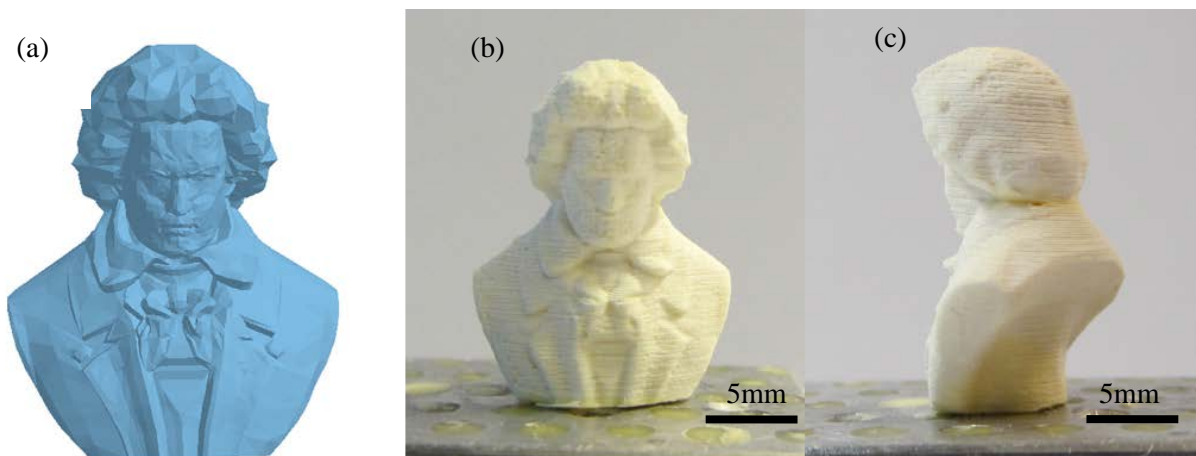


Figure 4.9 A “Beethoven” model fabricated with glass reinforced composite (a) CAD model (b-c) Two views of the built object

In this research, we investigate polymer based composite slurry by mixing sodium aluminosilicate glasses (Z-CEL 8054, Potters, Valley Forge, PA) with liquid resin. Sodium aluminosilicate glasses are white microspheres, originally developed as filler for paints, coatings and films. It has been used to improve hardness and abrasion performance of final product.

Composite slurry with 65% weight ratio of the glasses was prepared and used as the feedstock materials. The properties of the composite slurry are shown in table 3.1. All the associated process parameters discussed above are designed as in the table 4.1. Good optical transparency of the composite slurry allows a layer thickness as large as 100 μ m. Two sample models are fabricated with the given parameters, and the built objects are shown in the figure 4.8 and 4.9.

4.7 Case Study II: fabrication of high dielectric capacitor

Dielectric capacitors have attracted great interest as electrical energy storage devices, due to their capability of charging within milliseconds and high fatigue and retention properties (Yang, 2016). Polymer/ferroelectric ceramic composites and polymer/conductive filler percolative dielectric composites are two types of materials that have been widely studied for dielectric capacitors (Ramajo, 2007; Rahimabady, 2012; Mikolajek, 2015). Traditional fabrication methods for these devices embody drop casting, spin coating, hot pressing, roll coating, etc., which are significantly restricted by their incapability of producing complex structures. In this work, we fabricated 3D structured capacitors with the presented slurry-based SLA process. Ag decorated lead zirconate titanate (PZT) was used as fillers to enhance the dielectric properties of the composite material. This method offers the potential to reliably produce capacitive components for printed circuit board, high-k gate dielectrics and embedded passive components.

4.7.1 Starting Materials

PZT powders (DeL. Piezo Specialties, LLC, West Palm Beach, FL) with an average particle size of 3 μ m were deagglomerated in a ball mill for 24 hours. Photocurable resin from Makerjuice Lab (Flex) was selected as the matrix material in this study due to its excellent photosensitivity. Other used materials include aqueous solution of H₂O₂ (30 wt%), toluene, ethylene glycol, silver nitrate (AgNO₃), 3-aminopropyltriethoxysilane, etc. All the chemicals were used as received unless particularly specified.

Although PZT powders can have a dielectric constant ranging from 300 to 3850 (wiki PZT 2016), the dielectric properties of the PZT/polymer composites are still poor, due to the low dielectric constant of their resin matrix. Surface decoration of the PZT particles with Ag (denoted as PZT@Ag) is one of the methods to improve the compatibility and dielectric properties of the composites (Lu, 2008; Dang, 2013). By introducing a conductive interlayer around a dielectric particle, polarization and charge aggregates, so called Maxwell-wagner-sillars effect, can be enhanced (Panda 2008; Huang 2009b), such that the dielectric permittivity can be consequently improved. PZT@Ag hybrid particles were synthesized via a seed-mediated growing process by a redox reaction between silver nitrate and ethylene glycol, as shown in figure 4.10. Three steps were involved in the seed-mediated growing process: hydroxylation of as-received PZT particles, functionalization of PZT-OH and grafting of nano-Ag particles (Yang 2016).

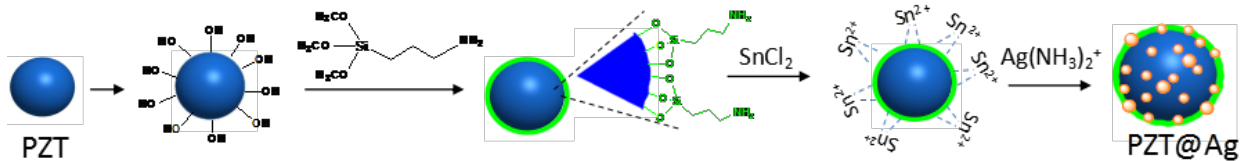


Figure 4.10 Scheme of the preparation process of the PZT@Ag nanoassemblies

Hydroxylation of as-received PZT particles: 10 g PZT particles were added into 50 ml aqueous solution of H₂O₂ (30 wt%) in a round-bottomed flask. The mixture was sonicated for 30 min and then heated at 105°C for 4 h. The nanoparticles were recovered by centrifugation. The obtained PZT particles were washed with deionized water for three times and then dried under vacuum at 80 °C for 12 h. The hydroxylated PZT particles were named as PZT-OH.

Functionalization of PZT-OH by chemical groups: 10 g PZT-OH nanoparticles and 2 g (3-aminopropyl) triethoxysilane (APTES) were first added into 80 ml toluene in a round-bottomed flask and sonicated for 30 min, and then the mixture was heated at 100 °C for 2h. The nanoparticles were by centrifugation. The obtained nanoparticles were washed with toluene two times and were dried under vacuum at 80 °C for 12 h and named as PZT-SH.

Grafting of nano-Ag particles onto the surface of PZT-SH: 10 g PZT-SH was added into 50 ml ethylene glycol in a flask and sonicated for 30 min. Then ethylene glycol containing 0.5 g AgNO₃ was slowly added. The mixture was heated to 160 °C and stirred under nitrogen for 2 h. The particles were recovered by centrifugation and were washed with water and acetone several times. The obtained particles were denoted as PZT@Ag.

PZT@Ag-polymer composites are prepared by mixing the synthesized PZT@Ag particles with the Flex resin. The selected solid loading of the particles in our case is 18vol% or less, with the minimum filler aggregates. The mixing is conducted in an ultrasonic bath for 1 hour and then stirred for 5 hours before use. The introduction of conductive layer around PZT particle could improve the electric field distortion, but at the same time it increases the refractive index of the fillers and hence decrease the cure depth to be less than 40µm. By making use of the advantages of our process in fabricating viscous materials with low photosensitivity, we are able to fabricate capacitors with complex geometry from the developed materials.

4.7.2 Results and Discussion

For the PZT@Ag-polymer composite, a layer thickness of 25 µm and cure time of 10s were selected to fabricate capacitors, considering the 40µm cure depth under the same cure time. Figure 4.11a.1 demonstrates several hexagonal patterns with different size. The maximum edge width is 1mm (figure 4.11a.2) and the minimum edge width is 200µm (Figure 4.11a.4). Figure 4.11b.1 and figure 4.11b.2 show two 3D capacitors with solid hexagon pillars or holes. The hexagon unit in both models has an average diameter of 400 µm and height of 600µm (about 24 layers). In figure 4.12, we built a star and a bowl using Flex and 18 vol% PZT@Ag. It can be seen that there are no macroscopically observed cracks in the parts and the surface of each part is smooth, which are important for the electrical properties of the composites.

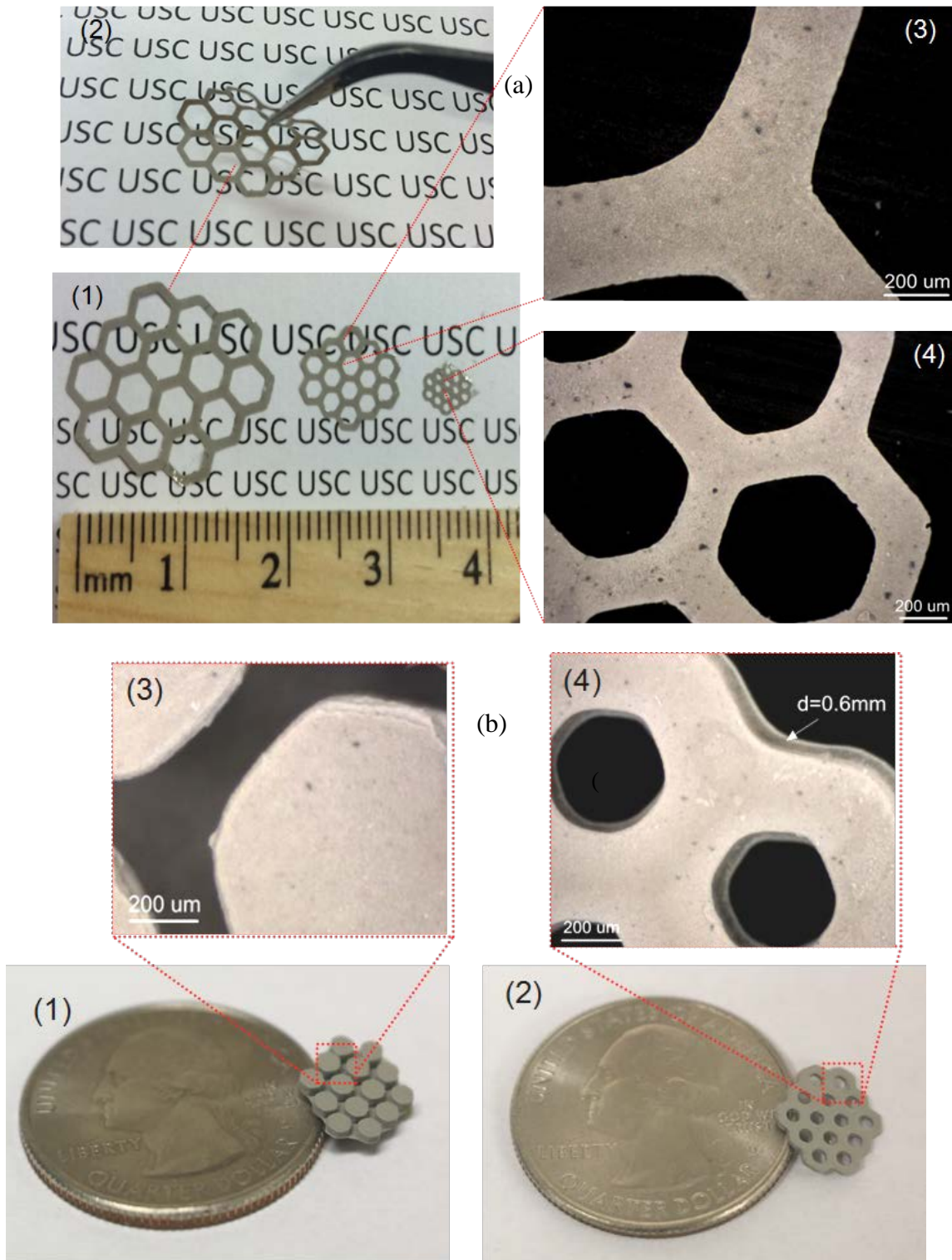


Figure 4.11 Fabricated capacitors (a) A cured layer of hexagonal pattern with different sizes (b) 3D hexagonal patterns of Flex/PZT@Ag (18 vol%) composites

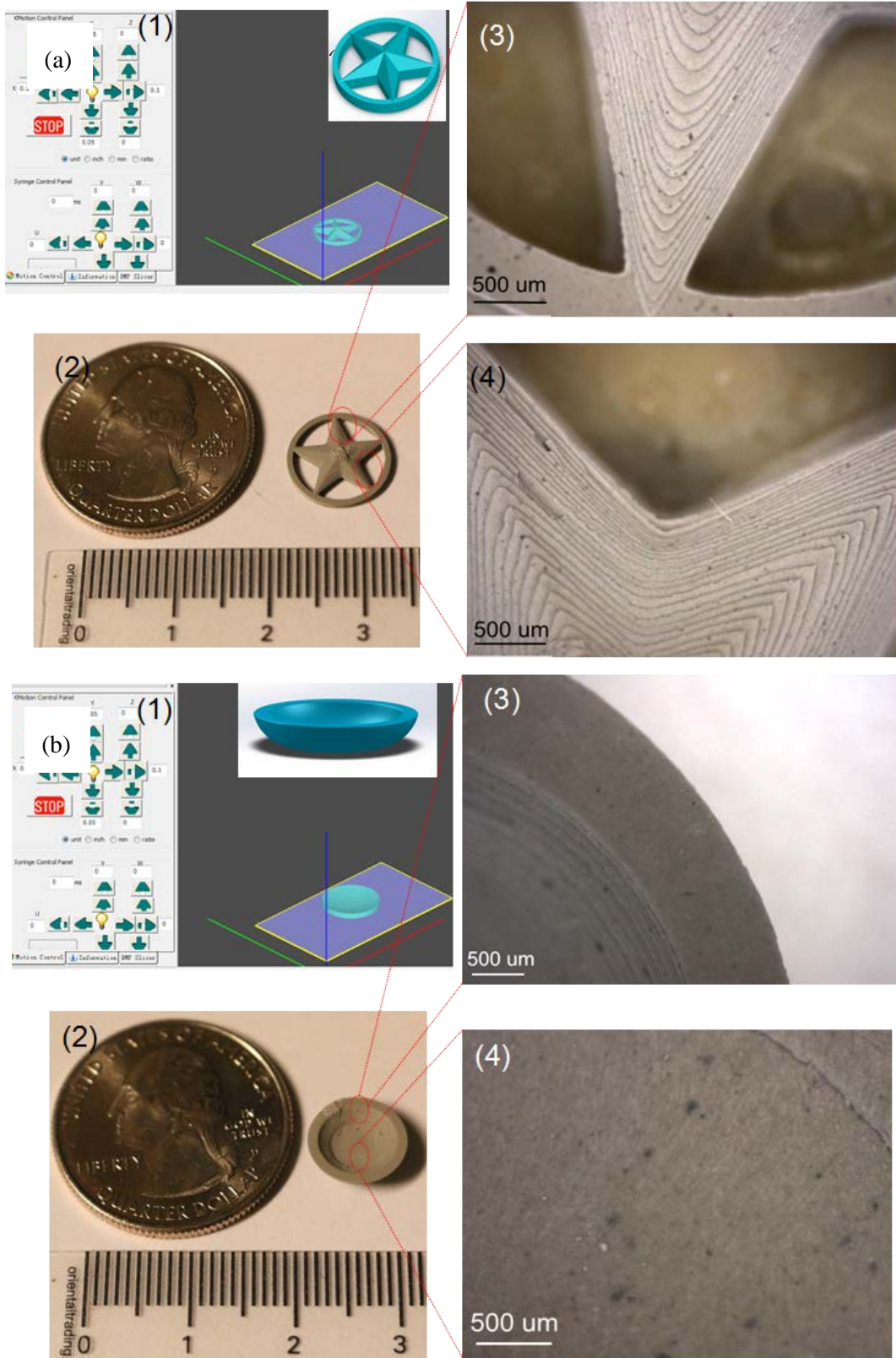


Figure 4.12 Fabricated capacitors (a) Star structure (b) Bowl structure

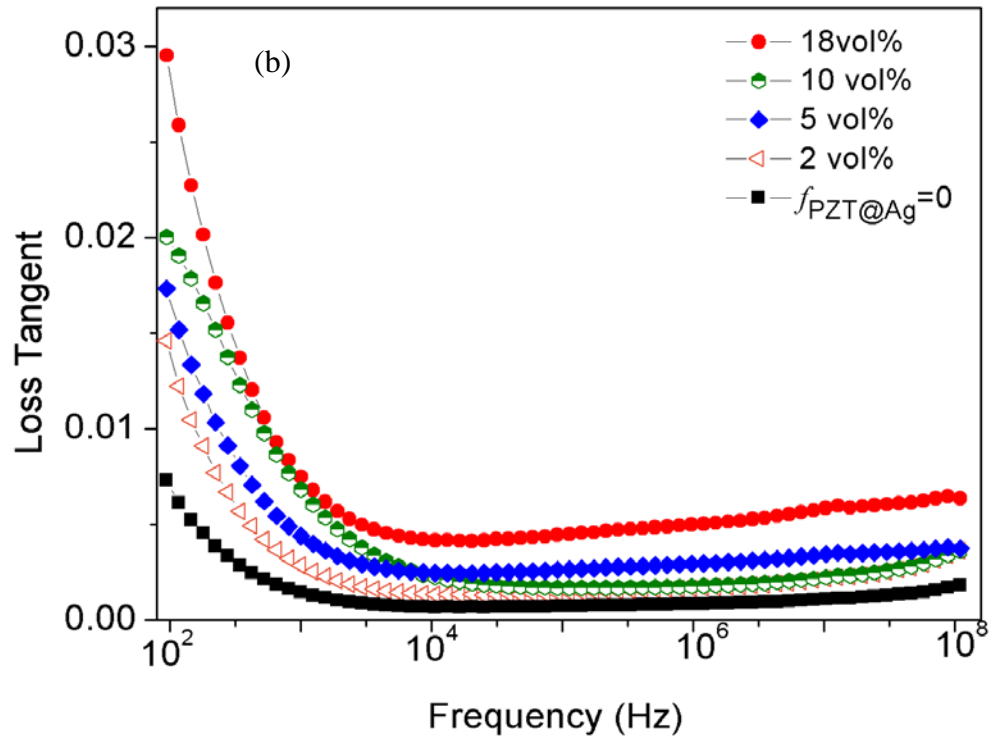
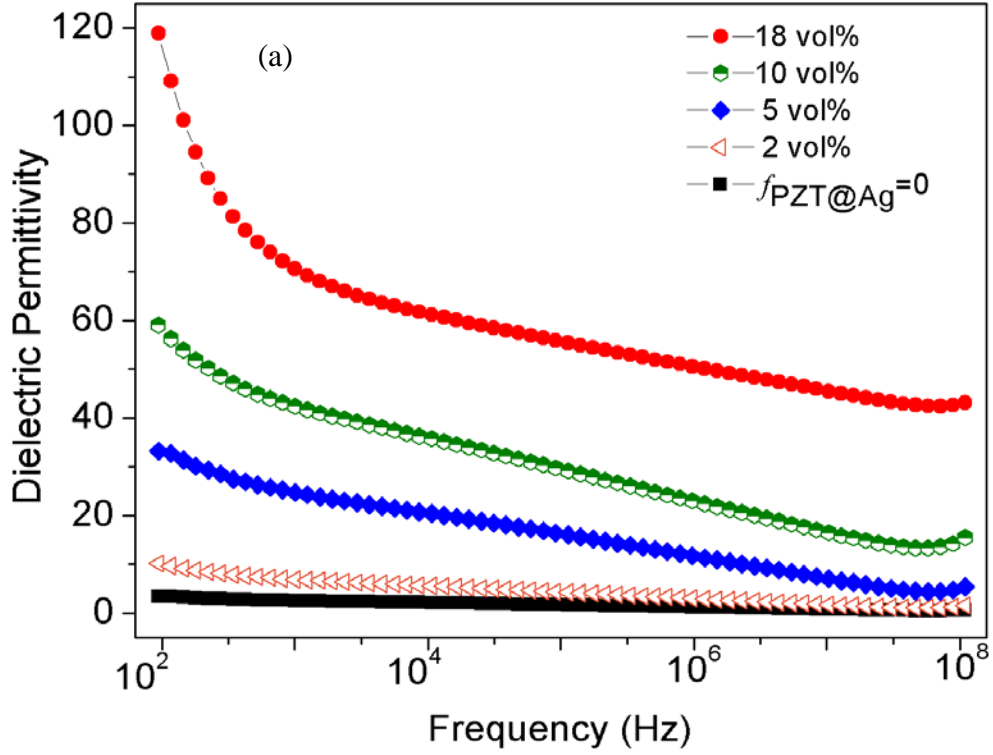


Figure 4.13 (a) Dielectric permittivity of composite film w.r.t frequency (b) Loss tangent of composite film w.r.t. frequency

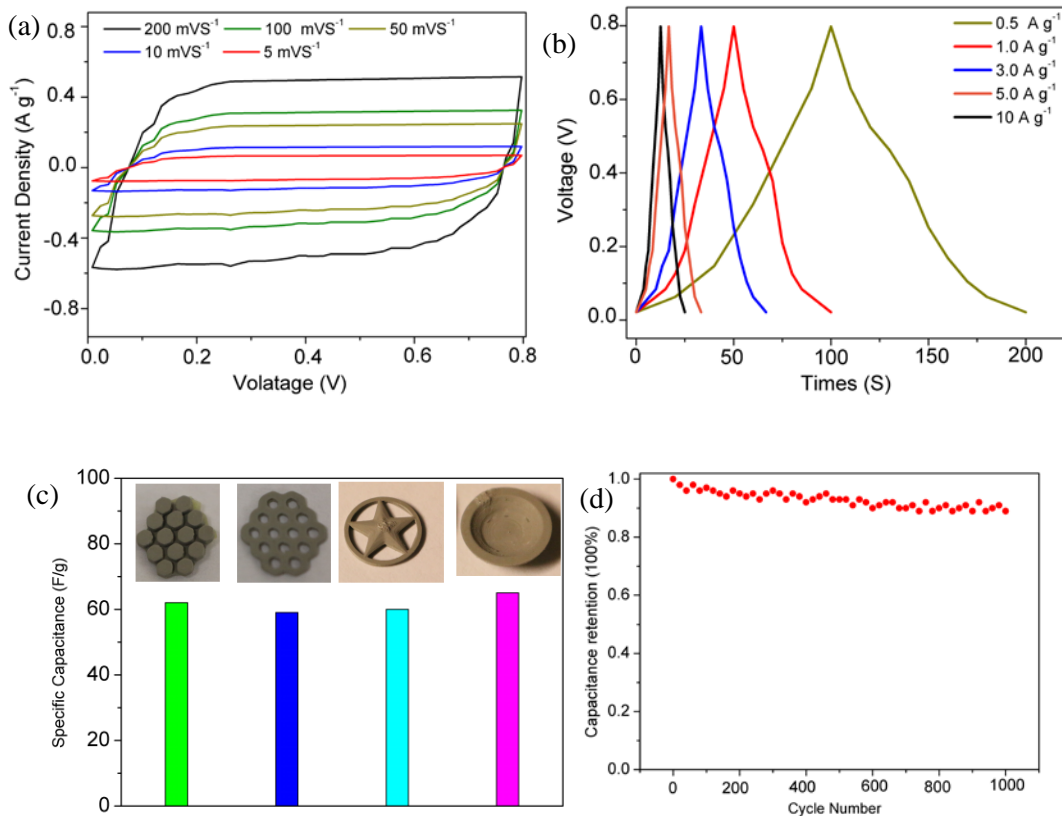


Figure 4.14 Electrochemical measurements for the as-printed capacitors (a) Cyclic voltammetry (CV) curves for the solid hexagonal pillar array (figure 4.11b.1) at different scan rates (5,10,50,100,200 mVS-1), (b) charge-discharge curves of the solid hexagonal pillar, (c) specific capacitances of different types of 3D printed capacitors, (d) Capacitance retention of the solid hexagonal pillar array capacitor after 1000 cycles under current density of 5 A g^{-1} .

Dielectric permittivity (ϵ) and loss tangent ($\tan \delta$) of PZT@Ag-polymer composite films with different volume fractions were measured by a precision impedance analyzer (Agilent 4294a, Keysight Technologies, Santa Rosa, USA), as depicted in figure 4.13. The measurement was conducted in the frequency range of 100Hz-100MHz at room temperature. It can be seen in the figure that both ϵ and $\tan \delta$ increase gradually with filler content. The composite film with a 18vol% solid loading has the largest dielectric permittivity of 120 (100Hz) and a low dielectric loss (0.028 at 100Hz). The dielectric permittivity of this composite film

is about 30 times higher than that of the pure Flex resin ($\epsilon=4$). The loss tangent is slightly higher than the other solid loadings though, it is still low enough, especially at a high frequency, to use in a capacitor for reduced energy loss.

To measure the capacitance of each capacitor shown in figure 4.11b and figure 4.12, both sides of the printed parts were sputter-coated with a gold electrode. Figure 4.14a shows cyclic voltammetry (CV) curves of the 3D printed solid hexagonal pillar array capacitor, which exhibits nearly rectangular shapes at different scan rates from 5 mVs⁻¹ to 200 mVs⁻¹, indicating this kind of capacitor possesses low resistance and ideal capacitive properties. Figure 4.14b displays the galvanostatic (GA) charge/discharge curves of the capacitor at different current densities. The specific capacitances of different types of 3D printed capacitor were calculated from their charge/discharge curves according to the following equation:

$$C_{sp} = \frac{I \times \Delta t}{\Delta V} \quad (4.20)$$

where C_{sp} is the specific capacitance, I is the constant discharging current density, Δt is the discharging time, and ΔV is the voltage window (Lu, 2012; Wang, 2012). The calculated specific capacitance of our 3D printed capacitor is about 63 F g⁻¹ at the current density of 0.5 A g⁻¹. Capacitance retention with respect to cycle number was measured with the solid hexagonal pillar array capacitor. Figure 4.14d shows the result: little degradation was observed for the tested capacitor after 1000 cycles, which indicates an excellent electrochemical stability of the 3D printed capacitors.

4.8 Summary

In this chapter, we discussed the main parameters involved in the slurry-based SLA process, including doctor blade height, recoating speed, separation speed, etc. These parameters are mainly determined by the curing and rheological properties of the materials, and have to be changed if a different type of slurry is used.

The tape casting system in our process is modeled as a Couette flow pattern, in which the flow rates result from the drag force between the doctor blade and the film collector. Based on the boundary conditions of this flow pattern, the dependence of the recoated layer thickness on the doctor blade height was derived. Furthermore, a higher speed was suggested for the slurry recoating which can yield a lower viscosity of the slurry.

An experimental method was presented to determine the layer pressing speed. The speed can reduce the error of actual layer thickness arising from the deformation of PDMS film under the pressure of Z platform.

A selection range for sliding speed was derived to enable the separation of each layer by the sliding mechanism without breaking tiny features.

Equations are derived for the material feeding system, including the moving distance of the dispenser and its plunger and the nozzle height, in order to guarantee a desired amount of slurry is delivered for each layer.

Finally, two test cases were presented to demonstrate the application of our process in fabricating composite components. The first case is to produce glass reinforced polymer composites. The fabricated samples using our process suggest a good accuracy of our method. The second case is to build high dielectric capacitors from resin/PZT@Ag composites. According to our measurement, the dielectric permittivity of resin/PZT@Ag composite reaches as high as 120 at 100Hz with 18vol% filler, which is about 30 times higher than that of pure resin. Although the loss tangent increases with the filler loading, it still remains at a low level around 0.028. Additionally, we built capacitors in different shapes, and measured their specific capacitance as 63 F/g at the current density of 0.5 A/g.

Chapter 5 Post Processing for Ceramic Component Fabrication

5.1 Overview

An important application of the presented slurry-based stereolithography (SLA) process is to fabricate high-performance structural or functional ceramic materials, such as aluminum oxide and piezo-ceramic component. Researchers have studied AM processes fabricating high-performance ceramic powders. A developed method based on Selective Laser Sintering (SLS) is to use high energy laser beam to locally sinter ceramic particles such that they will bond with each other. However, due to the high sintering temperature of ceramics, low melting point media such as polymer powder is usually added into ceramic powders. As shown in figure 5.1a, the low-melting point particles serve to bind ceramic particles together in the SLS process. Finally, some post-processing procedures are performed to burn out the added binder and to fuse ceramic particles.

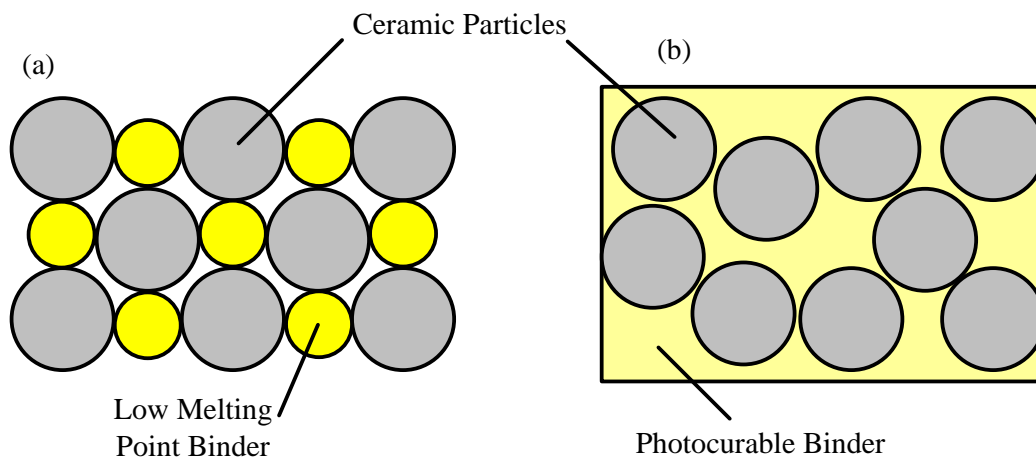


Figure 5.1 Different methods of bonding ceramic powders in additive manufacturing

Similarly, slurry-based SLA process adds photocurable resin into ceramic powders, which serves to bind ceramic particles together after being solidified by a light source (refer to figure 5.1b). Post processes were also performed, during which cured resin is burned out, ceramic particles of interested are left behind and grow together such that the sintered ceramic part becomes much denser.

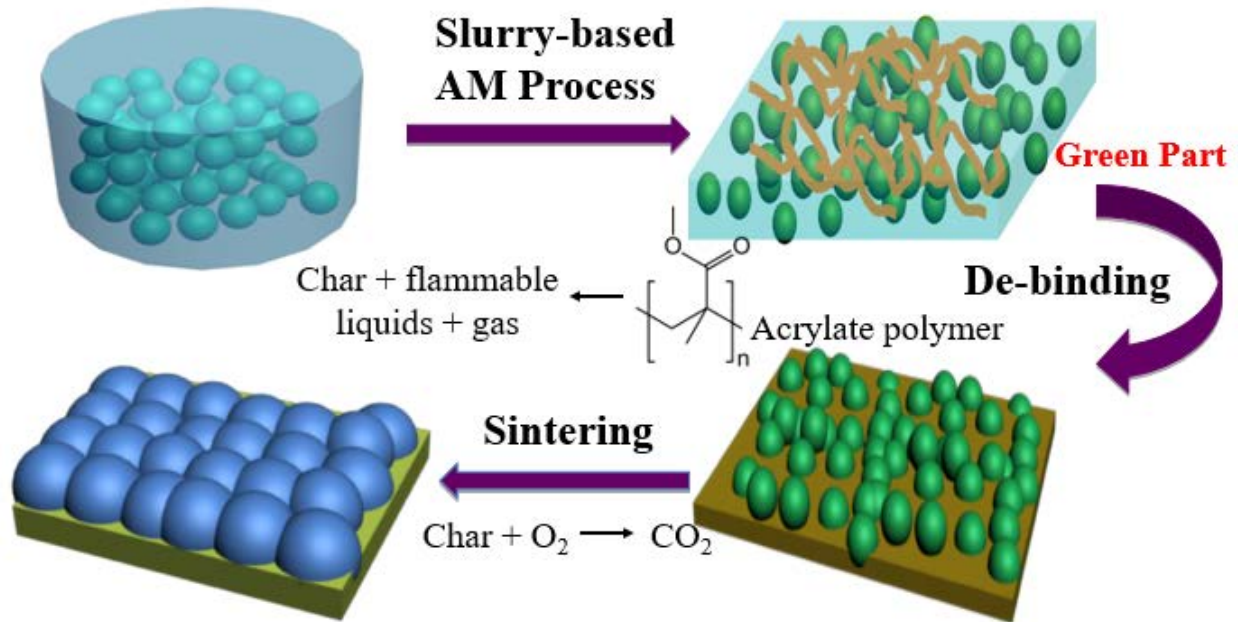


Figure 5.2 Schematic of Post Processing for Ceramic Component Fabrication

As shown in figure 5.2, there are three steps involved in the ceramic fabrication by firing polymer-ceramic composites. First ceramic powder is mixed with photocurable binder. The obtained viscous mixture is fabricated into a polymer-ceramic composite component via the slurry-based SLA process. We call this component as *green part*. In the second step, the green part is heated in a furnace, until the acrylate polymer in the green part is completely decomposed into char, flammable liquids and gas. The flammable liquids and gas are removed after the debinding, while the residual char in the debinded part serves as binders to retain the shape of the part. Finally, the part is sintered in a furnace. During the sintering, all the residual char reacts with the oxygen and turns into carbon dioxide. As a result, a pure and dense ceramic component can then be obtained. In the following sections of this chapter, we introduced the fabrication of two popular

types of ceramics using the method described above: *Aluminum Oxide* and *Barium Titanate* (BTO), which can be categorized as structure and functional ceramics respectively.

5.2 Case Study I: Traditional Ceramics for Structural Purpose

Aluminum oxide, commonly called alumina, is a crystalline raw material for a broad range of ceramic product. It is widely used for its low electric conductivity, chemical inertness, high strength and hardness. However, such excellent physical and chemical properties make it hardly be produced with conventional machining processes. By using our slurry-based SLA process along with post processing, we successfully generate alumina components with a relatively high density.

5.2.1 Green Part Fabrication

Alumina slurry with a solid loading of 65wt% is made by mixing the alumina powders with SI500 resin. The viscosity of the mixed slurry is around 5~250Pa•s with no diluent added in the suspension. The main process parameters that are used in the fabrication process are listed in Table 5.1. A longer curing time is used when building the initial 5-10 base layers; for other layers, a shorter curing time is used.

Table 5.1 Process parameters used in the fabrication process for alumina composite

| | Curing time for base/normal layers (s) | Layer thickness (μm) | Blade gap δ_{blade} (μm) | Recoating speed v_r (m/s) | Pressing speed v_p (mm/s) | Sliding speed v_s (m/s) |
|---------|----------------------------------------------|-----------------------------------------|-------------------------------------------------|-----------------------------------|-----------------------------------|---------------------------------|
| Alumina | 2/1 | 50 | 300 | 0.0254 | 0.293 | 0.0254 |

Figure 5.3 shows some of the fabrication results based on the selected process parameters. Figure 5.3a is a gear with a diameter of 15mm and a thickness of 3.78mm. Figure 5.3b shows a model of 25 hexagon

array. Both the length and width of the part are 15mm. The height of the base is 1mm, and the height of the hexagon is 1.26mm. Figure 5.3c shows a cutting tool in a diamond shape with a $\Phi 3$ mm hole in the center. In figure 5.3d is a tooth model.

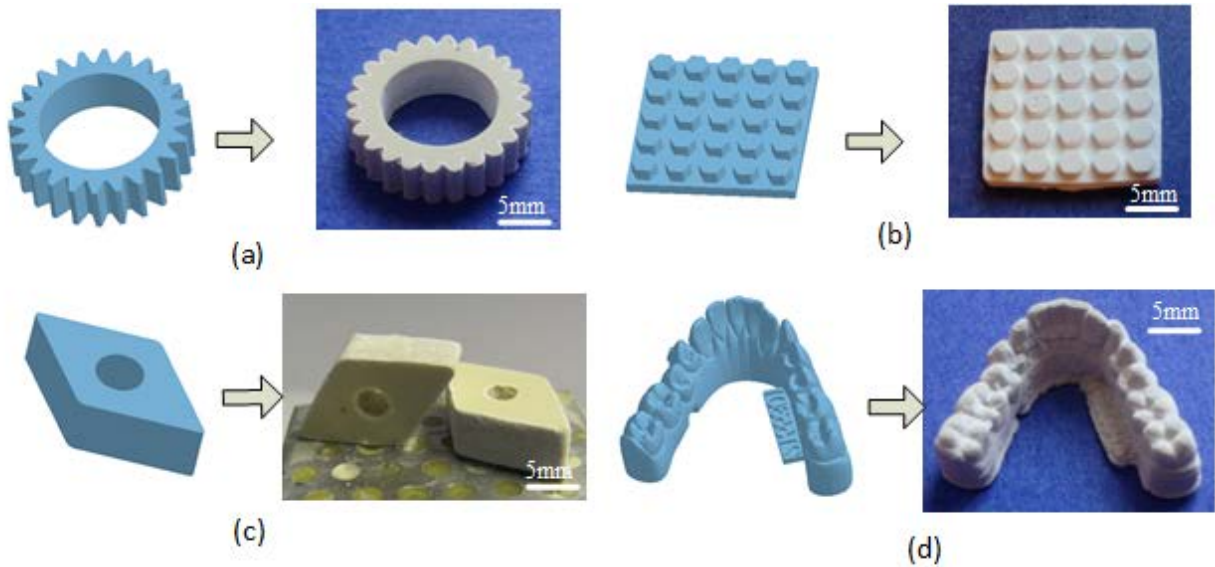


Figure 5.3 Alumina Green Parts fabricated by the tape-casting-integrated SLA process

5.2.2 Post Processing

The green parts fabricated by the slurry-based SLA process is an alumina-resin composite part consisting of organic compound (cured resin) and ceramic powders. In this section, we briefly discuss the post processing of the fabricated green parts in order to achieve fully dense ceramic components. The main post processing steps include organic binder burning-out and high-temperature sintering. A test case of a gear model is used to demonstrate the post-processing procedures. The solid loading of alumina powders is 65wt%. Based on the thermal analysis (TG-DSC) of the composite materials, the de-binding and sintering procedures for alumina are designed as follows.

In the de-binding step, the organic composition in the green part is fully burned out. To avoid delamination and pores, the green sample is put in a vacuum muffle furnace and debinded under a temperature of 600°C for 3 hours. After the polymers in the green part are burned out, a high-temperature

sintering process is carried out to improve its density. The sintering of the debinded sample is conducted in a regular muffle furnace at 1650°C for 1 hour. The heating schedules for both de-binding and sintering of the Alumina gear part are shown in figure 5.4.

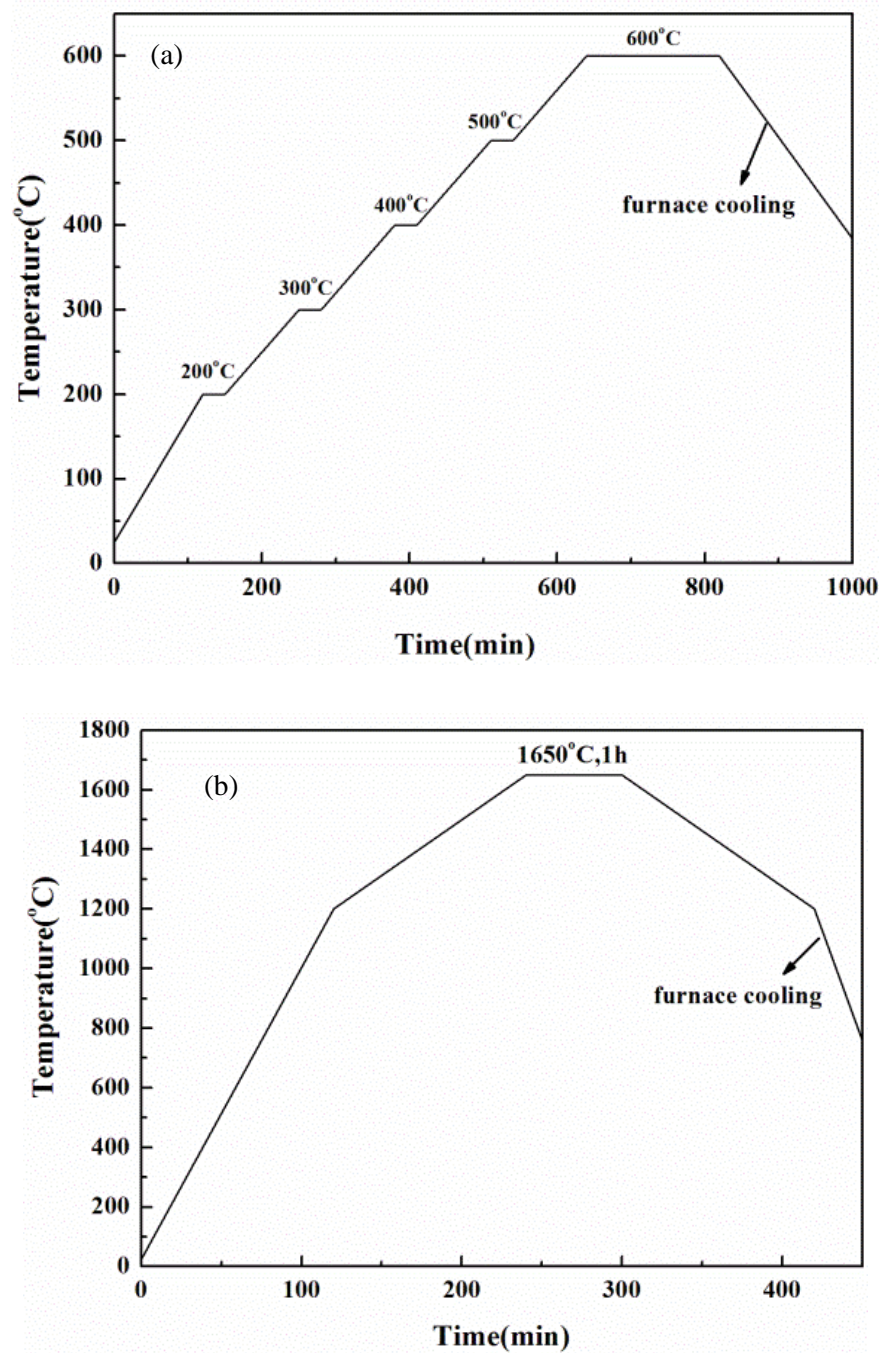


Figure 5.4 Post processing of Alumina green parts. (a) De-binding schedule; (b) sintering schedule

5.2.3 Testing Results of Sintered Samples

The Alumina green part and the corresponding sintered part are shown in figure 5.5a and 5.5b, respectively. The diameter of the green part is 15mm. After the de-binding and sintering procedures, the diameter of the gear part is ~11.6mm. The shrinkage of the presented ceramics fabrication process for the gear model is ~22.7%. Such shrinkage can be compensated by enlarging the original CAD model by an accordingly estimated ratio.

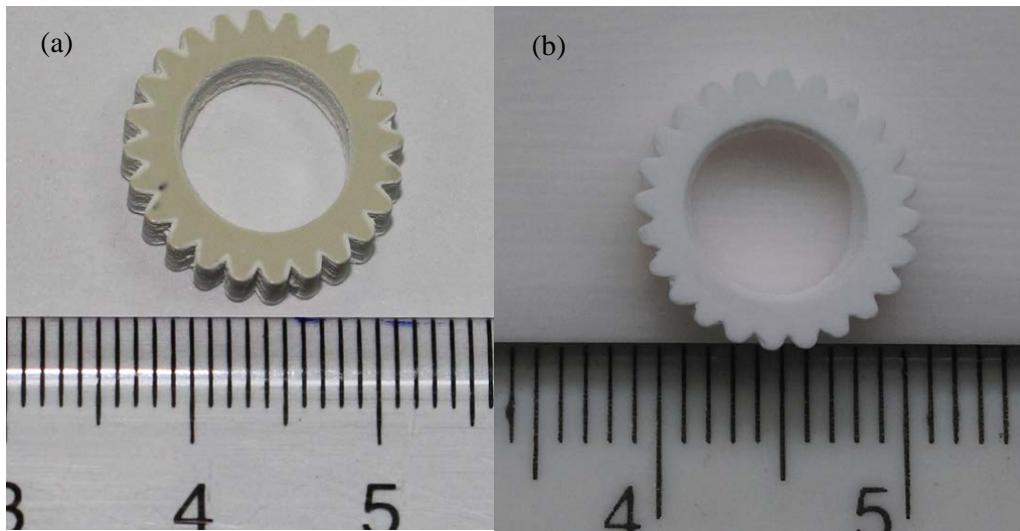


Figure 5.5 A test case of a gear model. (a) The green part of an alumina gear model; (b) the fabricated alumina gear after the de-binding and sintering procedures

Samples in the shape of a simple block are fabricated using the same materials and process settings as the ones used in the fabrication of the gear model. The cross-sections of the block samples before and after the post processing are prepared and put under a Scanning Electron Microscope (SEM). Figure 5.6 shows the SEM images of green and sintered parts. Figure 5.6a shows that the polymer and alumina particles are mixed uniformly throughout the entire volume, although some agglomerates in the green part may still exist. The average size of the alumina particles in the green part is less than $1\mu\text{m}$ due to the ball milling process. Figure 5.6b shows large alumina grains with obvious boundaries are generated after the de-binding and sintering processes. Improvement in the post-processing can be made to remove pores in the final part by

adding isostatic pressure during the sintering process. A density of 93.2% of true alumina density ($3.95\sim 3.98\text{g/cm}^3$) is obtained in the sintered block samples

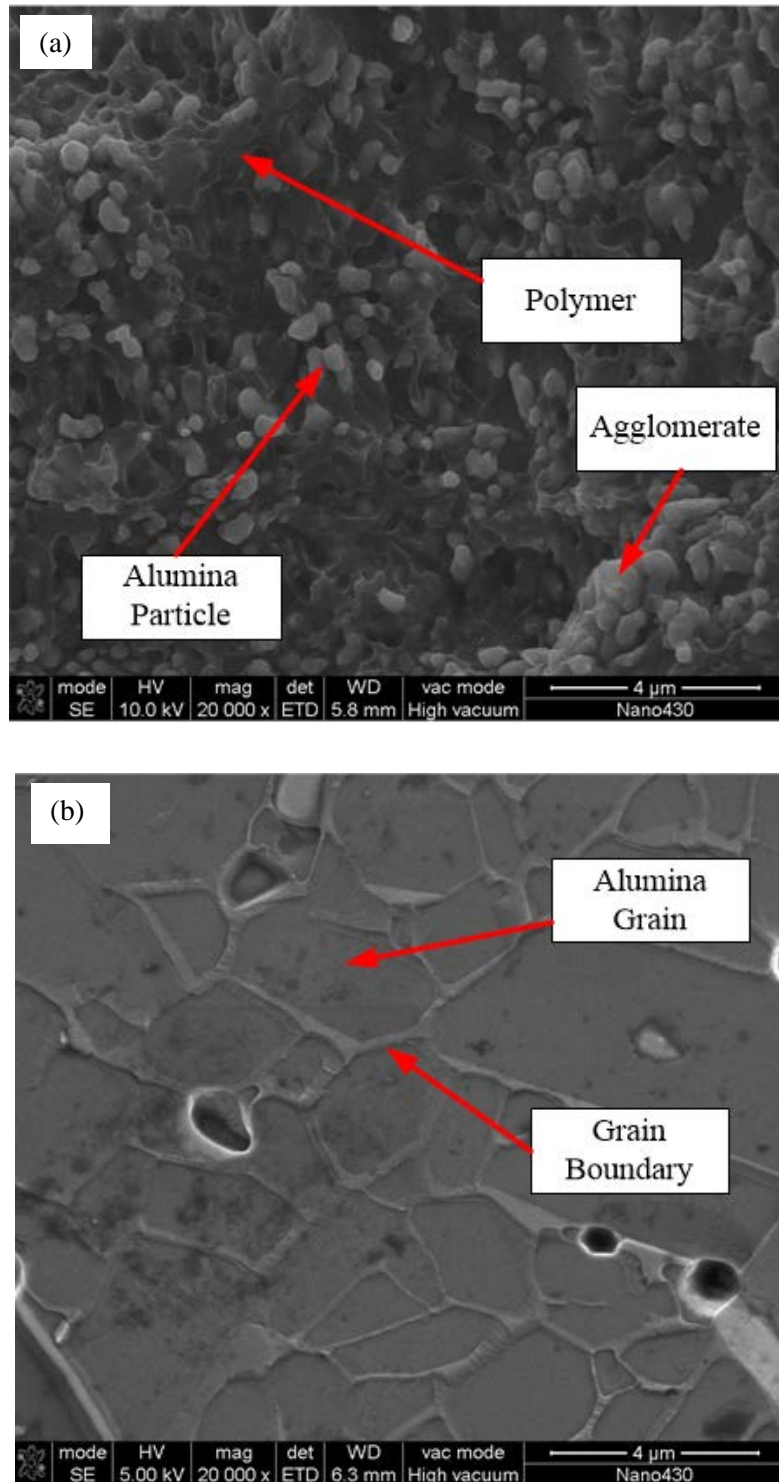


Figure 5.6 The SEM images of different samples. (a) Alumina green part; (b) sintered Alumina part

5.3 Case Study II: Piezoelectric Ceramics for Ultrasound Imaging

5.3.1 Introduction to Ultrasound Transducer

Ultrasonic imaging is an important medical imaging technique. Since ultrasound poses no known risks to patients, this technology has become one of the most widely used diagnostic tools in modern medicine (Shung, 2005). An ultrasonic imaging system requires an ultrasound probe, as shown in figure 5.7a. One of the core components of the ultrasound probe is a transducer array, which can produce mechanical energy in response to electrical signals and produce electrical signals in response to mechanical stimulus conversely. Ultrasound transducer arrays have been used to detect and visualize muscles, tendons, and many internal organs due to their advantages, such as high bandwidth, fast response, and high sensitivity.

Piezoelectric components such as ultrasound transducer arrays are generally made of piezoelectric ceramic materials, e.g. *Barium Titanate* and *Lead Zirconate Titanate* (PZT). Since these piezoelectric materials have relatively poor machinability, transducer arrays are typically fabricated into simple shapes, such as square or rectangle. In recent decades, new transducer designs based on aperiodic and non-rectangular array shapes have been investigated in the ultrasound transducer industry to achieve more efficient energy conversion (Akhnak, 2002; Thomenius, 2005). One of such design examples is shown in figure 5.7e, in which a hexagonal pattern is used (Thomenius, 2005). The new design is found to have less lateral mode coupling, contributing to a better acoustic efficiency. However, complex geometric designs with small dimensions poses significant challenges on the fabrication of an ultrasound transducer array. Current manufacturing methods have great difficulty in fabricating such complex piezoelectric components. For example, the dice-and-fill process prepares piezo-components by cutting a piezo-ceramic plate into an orthogonal array and filling the kerfs with polymer material, so it can only produce square arrays. To address such a challenge, we investigated the fabrication of piezoelectric ceramic components using additive manufacturing processes.

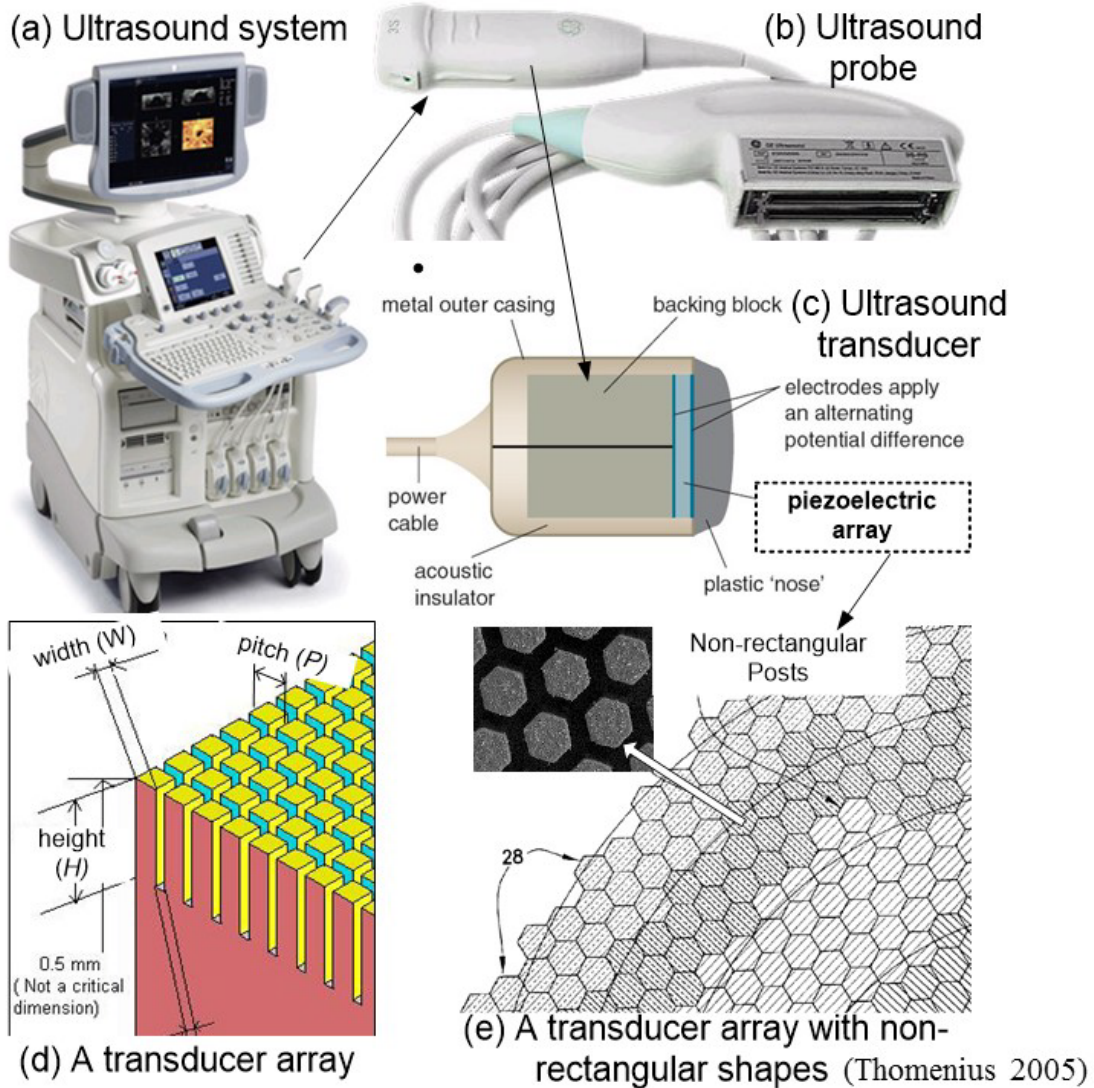


Figure 5.7 An illustration of ultrasound transducers in an ultrasound system

5.3.2 Related Work

Current approaches to fabricating piezoelectric components are mainly based on *machining*. Main steps of machining approaches are shown in figure 5.8a. Functional ceramics are first built in bulk and then cut into shapes by machining tools such as a dicing saw used in *dice-and-fill* techniques (Smith, 1991; Liu, 2001). However, cutting bulk piezoelectric materials becomes increasingly difficult as current trends on piezoelectric component design require more complex geometries to enhance their performance (Smith, 1986). Moreover, machining processes usually have relatively big feature resolutions which are limited by

their machining tools. Some other machining processes such as *laser dicing* techniques (Lukacs, 1999; Farlow, 2001) have been developed to fabricate smaller features. However, the ablation side effects and conic shape of ceramic arrays fabricated by these techniques have been observed, which will affect the piezoelectric performance.

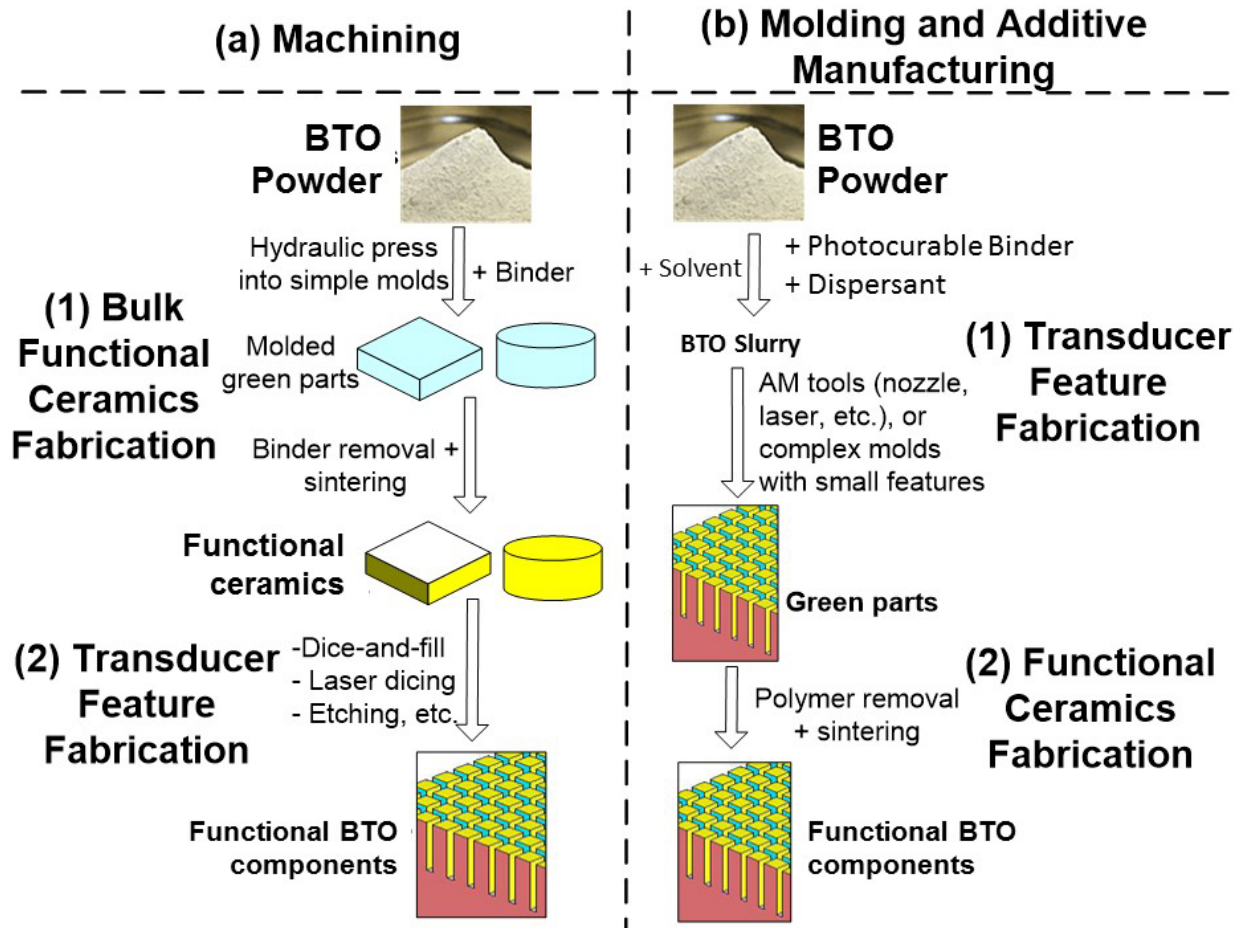


Figure 5.8 A comparison of piezoelectric component fabrication based on machining and AM processes.

Another approach to fabricating piezoelectric components is based on *molding and additive manufacturing* (refer to figure 5.8b). In these approaches, piezocomposite slurry is first made by mixing piezo-ceramic powders with polymers and solutions in certain mixture ratios. Various techniques have been developed to define the desired geometry in green-parts. An example is *composite micro molding* and *lost silicon molding* techniques (Hirata, 1997; Cochran, 2004), which consist of following steps: a silicon (or

plastic) mold is first made using the LIGA (lithography, galvano-forming and plastic molding) process (Becker, 1986); then the piezocomposite slurry is cast into the mold; and finally the mold is removed after applying a high temperature. The *lost silicon molding* or *injection molding* processes follow similar steps (Gentilman, 1994; Chu, 1998). However, these methods are indirect processes with multiple steps and each step requires significant effort. Other examples include *chemical vapor deposition* (CVD) (Aota, 2007) and *tape casting* methods (Chartier, 1997), which have been developed to directly deposit piezo-ceramic atoms or very thin tapes on a semiconductor substrate. However, the resulted geometry by these methods is usually simple and it is difficult to control the processes for more complex shapes.

During the past thirty years, many novel additive manufacturing (AM) processes such as *Stereolithography*, *Selective Laser Sintering*, and *Fused Deposition Modeling* (FDM) have been successfully developed and commercialized (Bourell, 2009). These AM processes have been investigated to fabricate piezo-ceramic parts before. For example, the *fused deposition of ceramics* (Lous, 2000; Safari, 2006) and *robocasting* processes (Cesarano, 1998) can directly fabricate piezo-ceramic parts by extruding piezocomposite slurry from a controlled nozzle. However, since these processes generally have a limited resolution and building speed, they are not suitable for the fabrication of ultrasound transducer arrays. Several variations of *stereolithography* (Brady, 1997; Dufaud, 2002; Sun, 2002; Bertsch, 2004) have also been developed by using a highly focused laser beam to scan over the ceramic slurry, but these processes are usually slow and require the viscosity of the materials to be small, hence they can only fabricate materials with low solid loadings. Digital projection devices such as *Digital Micromirror Devices* (DMDs) provide powerful tools that can dynamically control the energy input of a projection image. By using these digital devices in stereolithographic AM processes, a whole layer can be fabricated simultaneously and the fabrication speed can thus become substantially faster. Several research and commercial projection systems based on DMD have been developed (Farsari, 1999; Monneret, 1999; Bertsch, 2000; Sun, 2005; Lu, 2006; Pan, 2012b; Song, 2015). However, most of the research are focused on the fabrication of photocurable resin or structural ceramics such as alumina. Some of the previous work that considered piezo ceramics

(e.g. Dufaud, 2002) only studied the green-part fabrication; the heat treatment procedure and related material property measurements were not discussed. In this section we presented our investigation on both green-part fabrication and post processes. In addition to material property measurements, a functional device was built to demonstrate the capability of the projection-based stereolithographic AM process in piezocomposite fabrication.

5.3.3 Green Part Fabrication

BTO slurry used in our study is prepared as described in chapter 3.1. Tests on the curing characteristics of BTO slurry have been performed. An image of a square with a length of 8.57mm was projected into the system. The thickness and width of the cured films with different weight ratios were measured respectively with a length gauge (Heidenhain, Schaumburg, IL) and a caliper. The relations between cure depth/width and BTO weight ratio under different curing time (i.e. 1s, 2s, 8s and 16s) based on our experimental setup is shown in figure 5.9. For simplicity, slurry samples with weight ratio 30%-50% were prepared by ultrasonic mixing for 30 minutes. Slurry samples with weight ratios 60% to 80% were prepared by directly mixing photocurable resin with BTO powders in a ball mill. The light intensity of our projection system is $\sim 31.6\text{mW}/\text{cm}^2$ measured by an illumination level meter (Simpson electric, WI). It can be seen from figure 5.9 that cure depth decreases as more BTO powders are added. The slight increase in cure depth from 70% to 80% can be explained by non-homogenous mixing of 80% slurry due to its high viscosity, and this further indicates the significance of the presented slurry preparation method. The cure depth curves suggest bigger cure depth can be obtained by increasing curing time, but a longer curing time will also yield bigger overcure in width. The experimental result shows the optimal weight ratio for BTO fabrication through our system is 60-80wt% and a curing time of 2-8s, under which a reasonable cure depth can be obtained with the minimum overcure width.

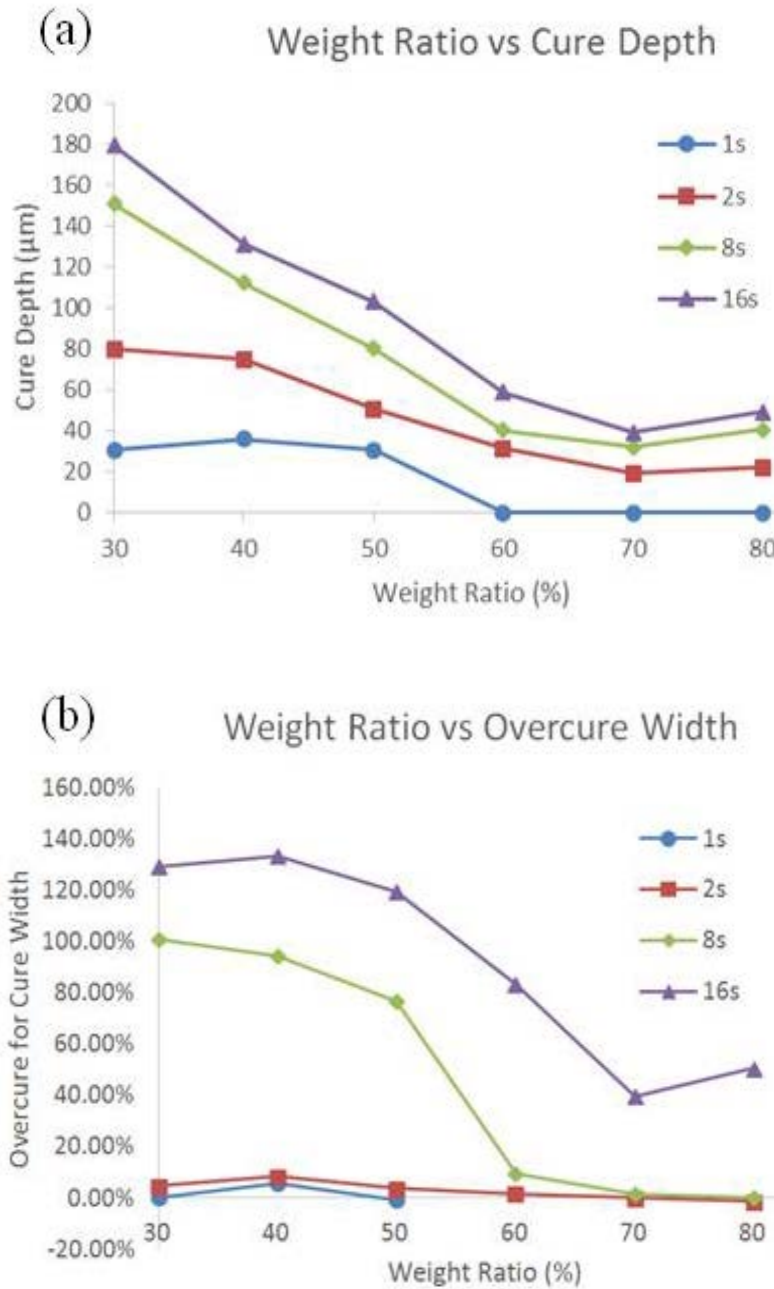


Figure 5.9 Curing characteristic of BTO slurry with varying BTO weight ratios

Piezoelectric ceramic powders have high refractive index with respect to the photosensitive resin in the slurry. This results in a light penetration depth as low as $40\mu\text{m}$. To ensure enough over cure beyond the layers, we chose the layer thickness for the building process as $20\mu\text{m}$. Then according to the doctor blade height equation, the doctor blade height δ is set to $100\mu\text{m}$ with a safety factor $\beta = 2$.

Table 5.2 Parameters used in the fabrication process for piezoelectric composites

| | Curing time for base/normal layers (s) | Layer thickness (μm) | Blade gap δ_{blade} (μm) | Recoating speed v_r (m/s) | Pressing speed v_p (mm/s) | Sliding speed v_s (m/s) |
|-----|----------------------------------------|-----------------------------------|----------------------------------------------|-----------------------------|-----------------------------|---------------------------|
| PZT | 2/10 | 20 | 100 | 0.0254 | 0.195 | 0.0254 |
| BTO | 2/2 | 20 | 100 | | | |

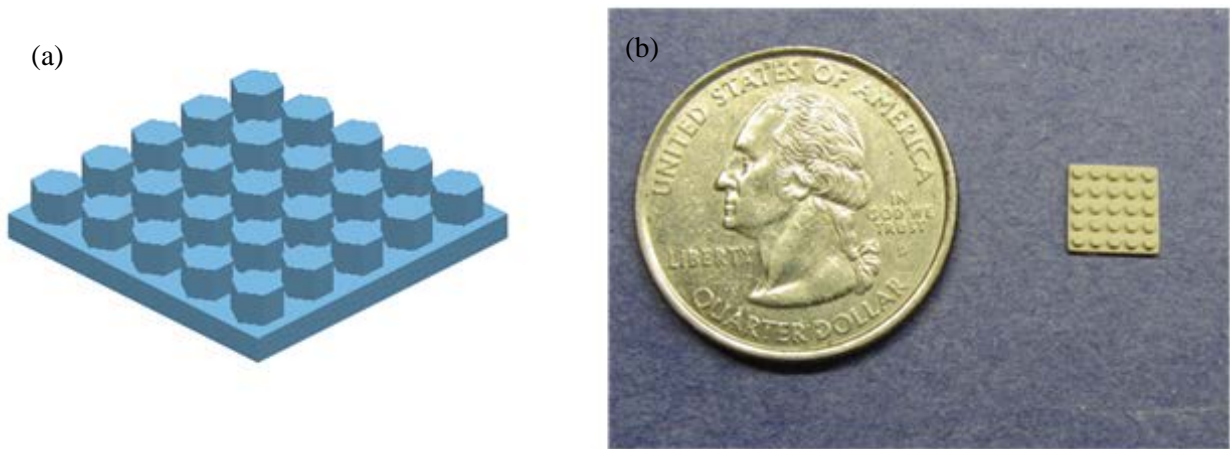


Figure 5.10 Fabrication result of a 0-3 PZT composite ultrasound transducer array with hexagon pillars (a) CAD model (b) Green part fabricated by our process

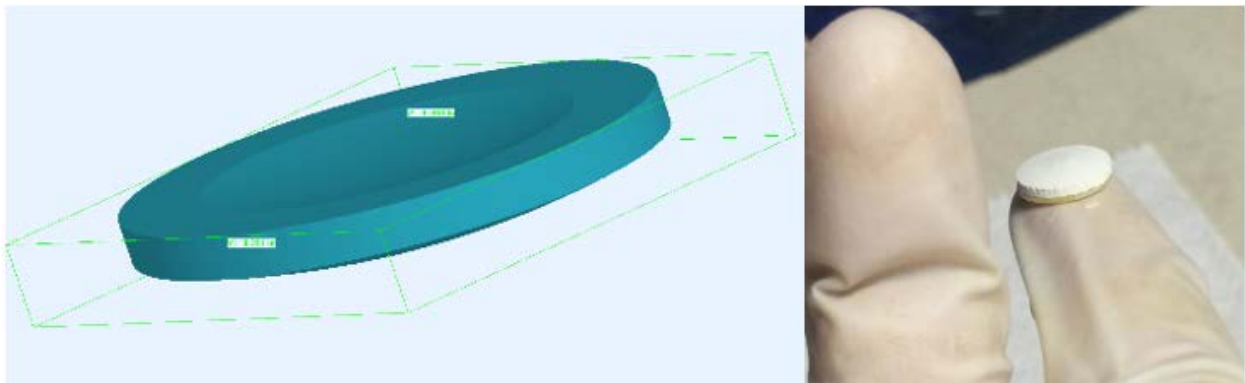


Figure 5.11 Concave BTO element fabricated by our process

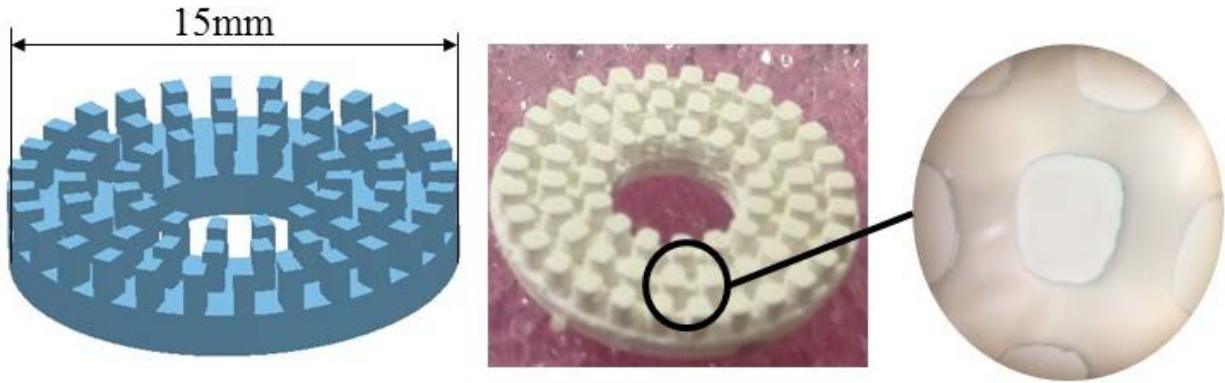


Figure 5.12 A 64 element BTO segment annular array fabricated by our process

With a light intensity of $\sim 31.6\text{mW/cm}^2$, suitable cure time is chosen for each powder at which a maximum cure depth and a minimum width overcure can be achieved. Based on the pressing speed curve for 3 micron BTO, a pressing speed v_p of 0.195mm/s was chosen in the process. All the selected parameters are listed in the table 5.2.

The CAD model of a 0-3 PZT composite ultrasound transducer array with 25 hexagon elements is shown in figure 5.10a. The size of the array is $6.5 \times 6.5 \times 1.0\text{mm}$, and the width of each pillar is 0.85mm . A concave ultrasound transducer element and an annular transducer array are fabricated with these parameter settings for BTO as shown in figure 5.11 and figure 5.12. The transducer array is designed to have 64 elements that can be dynamically excited to achieve desired ultrasonic imaging shapes. Each element is in a fan shape, with two edges intersecting at the center of the array.

5.3.4 Post Processing of BTO Green Parts

BTO green-parts fabricated by the AM process are a mixture of polymer and BTO particles. In the mixture, BTO particles are separated by polymers, which prevent efficient transmission of compression stress between the BTO particles when an external force is added. In order for the fabricated component to obtain piezoelectric properties, the polymer has to be removed and the left-behind parts need sintering to fuse BTO particles together. The debinding process is conducted first

to burn out the polymer in the samples. Following the debinding process, the sintering process is performed to convert the debinded BTO green-parts into fully dense ceramic components with desired piezoelectric properties. In this section the heat treatment procedures of the debinding and sintering processes are discussed. The material properties, especially piezoelectric properties, of sintered BTO components are measured and presented in section 5.3.5.

The temperature curves of both debinding and sintering processes of BTO green parts are shown in figure 5.13:

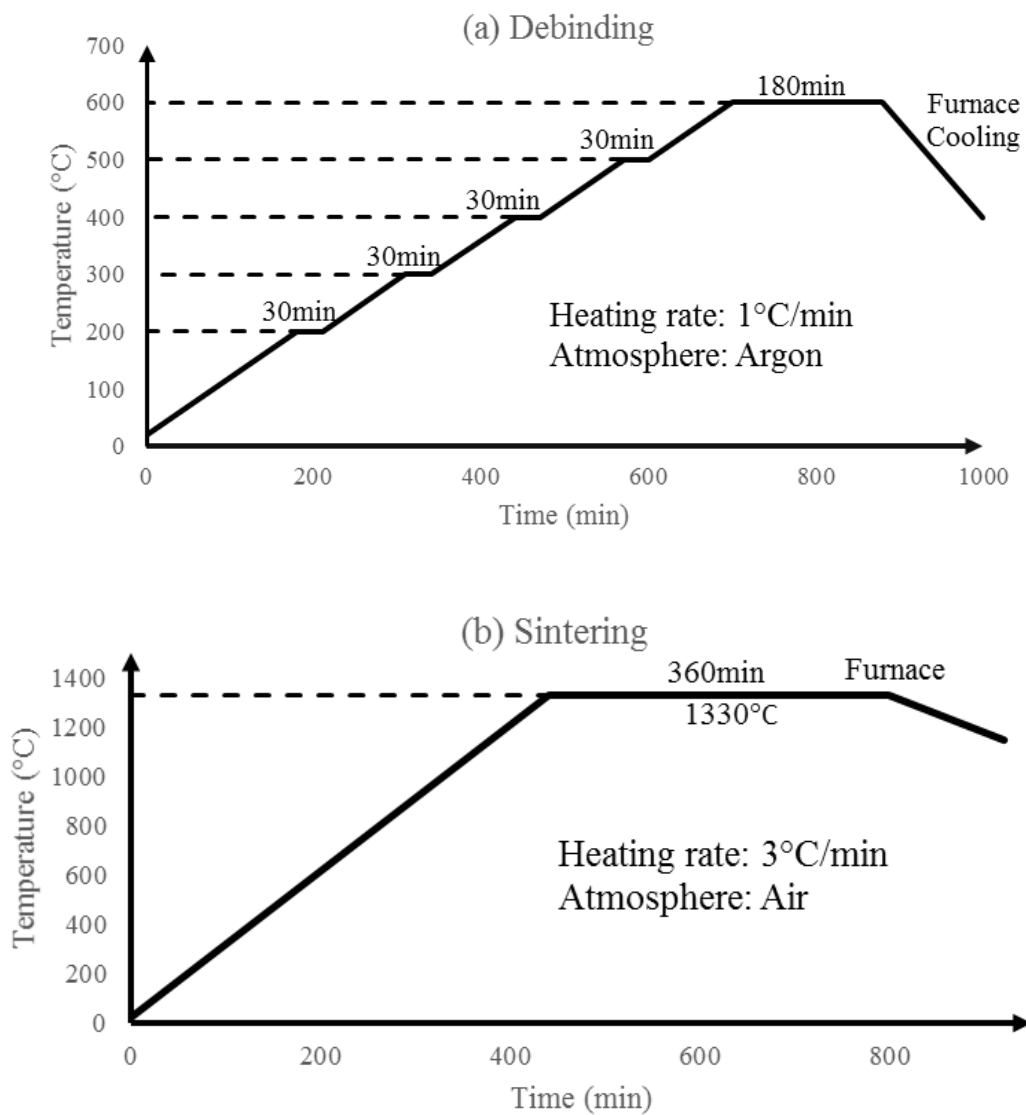


Figure 5.13 Temperature schedules for debinding and sintering of BTO green parts

(1) In the debinding process (refer to figure 5.13a), an argon furnace is used to fire the fabricated green parts. A batch of green parts can be heated at the same time in the furnace. The temperature rises from the room temperature at a rate of 1°C/min, and is held at 200°C, 300°C, 400°C and 500°C for 30 minutes, respectively. The polymer composition in the samples is fully pyrolyzed after the temperature were held at 600°C for three hours. During the debinding process, we use carefully designed conditions, including Argon atmosphere, low heating rate, and 30-minute dwell time at different temperatures, to slow down the chemical reaction and consequently avoid part damage due to the vapors that are generated in the pyrolysis of polymer.

(2) After green parts are debinded in the argon furnace, the sintering process (refer to figure 5.13b) is carried out in a regular furnace under a higher temperature (1330°C) with a dwell time of 6 hours. The ramp up rate in the sintering process is set to 3°C/min. We tested different sintering temperatures within 1200-1500°C, and finally choose 1330°C as the sintering temperature for BTO parts. The fabricated green parts of concave transducer element (refer to figure 5.14) and segment annular transducer array (refer to figure 5.15) are debinded and sintered using the aforementioned heating procedures. The sintered components are shown in figure 5.14bc and figure 5.15b. For the segment annular transducer array, the shrinkage during the debinding and sintering processes is about 26.7% along the *X* and *Y* axes and about 34.3% along the *Z* axis. The density of the sintered component is 5.64g/cm³, or ~93.7% of bulk BTO material (density 6.02g/cm³), measured by standard density test method ASTM B962-15.

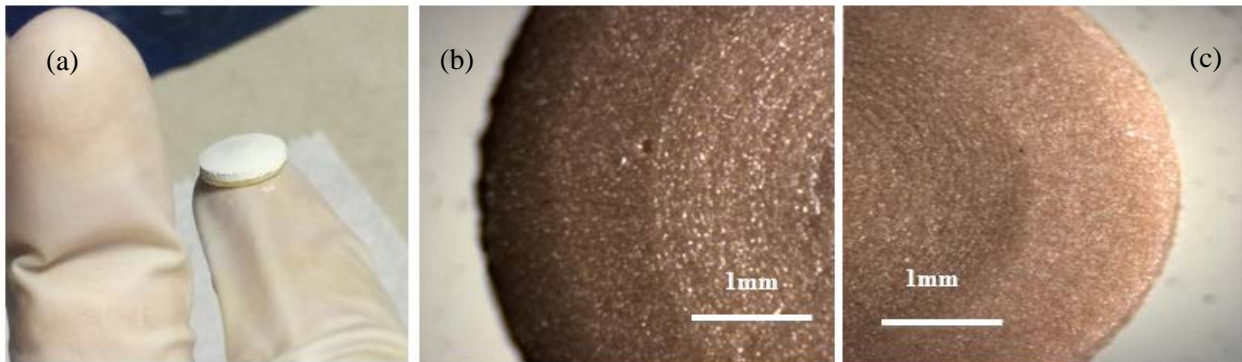


Figure 5.14 The concave transducer element: (a) green part; (b)(c) after sintering

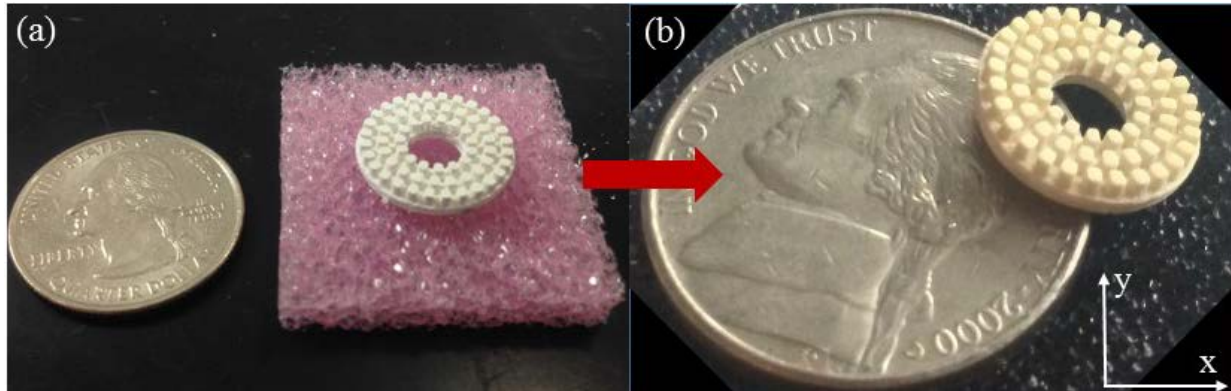


Figure 5.15 The segment annular transducer array: (a) greenpart ; and (b) after sintering

5.3.5 Testing Results of Sintered Samples

5.3.5.1 Material Property Measurements

In order to characterize the piezoelectric properties of sintered materials, a series of samples in a cylindrical shape (diameter 10mm, thickness 3mm) were fabricated and post-processed. The debinded and sintered samples were first analyzed using SEM. Figure 5.16a shows the sample surface after the debinding process, and figure 5.16b characterizes the surface of a sample after 6 hours sintering. It can be seen that polymers were burned out after the debinding process, which consequently left a lot of pores inside the samples and made the sample become fragile. After the aforementioned sintering process, however, the sample becomes much denser, as shown in figure 5.16b.

The structure of the samples was also examined using a Rigaku X-Ray diffractometer (Rigaku Corporation, Tokyo, Japan). As shown in figure 5.17, the fabricated material has a relatively well-crystallized perovskite phase and is suitable for multi-ferroic applications such as ultrasound transducers.

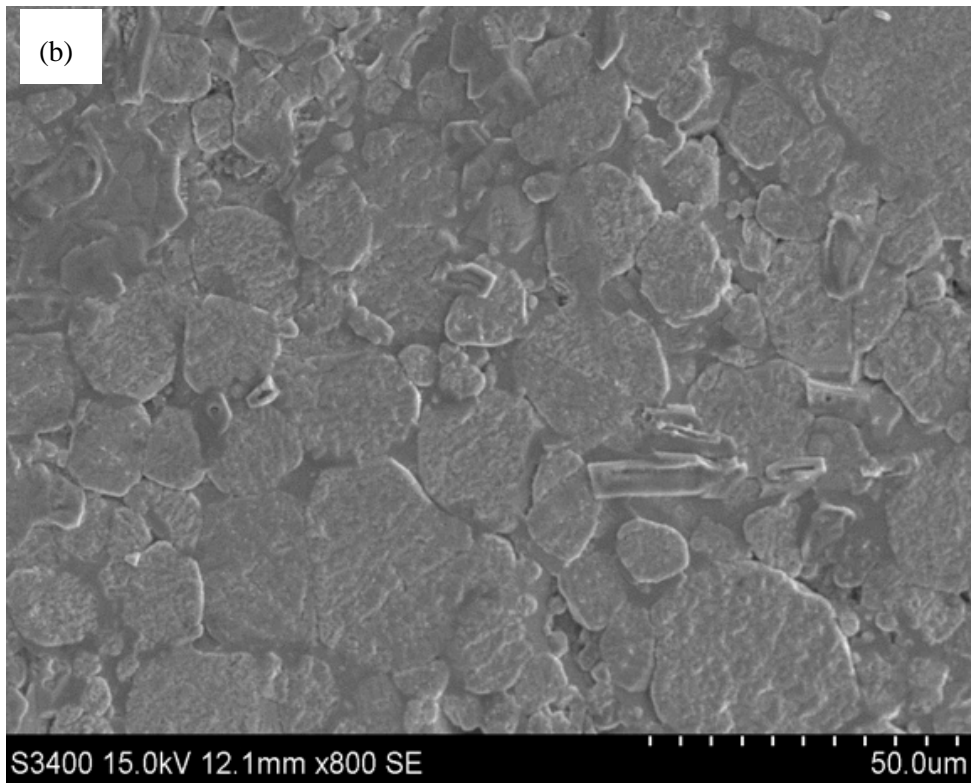
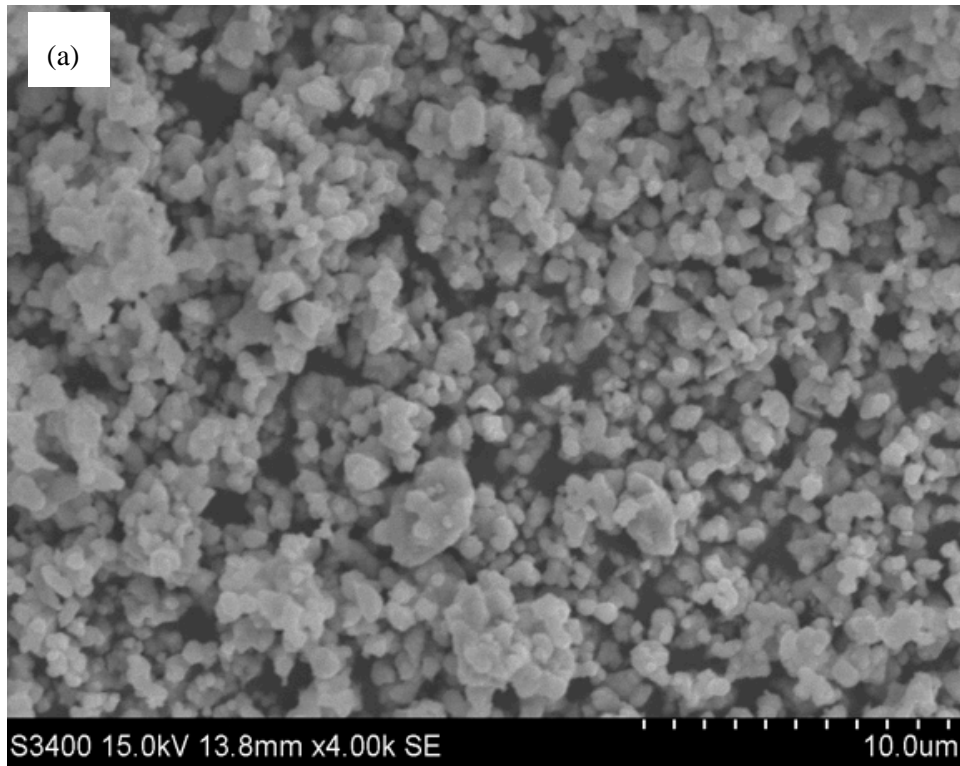


Figure 5.16 Scanning electron microscope images: (a) after debinding; (b) after sintering

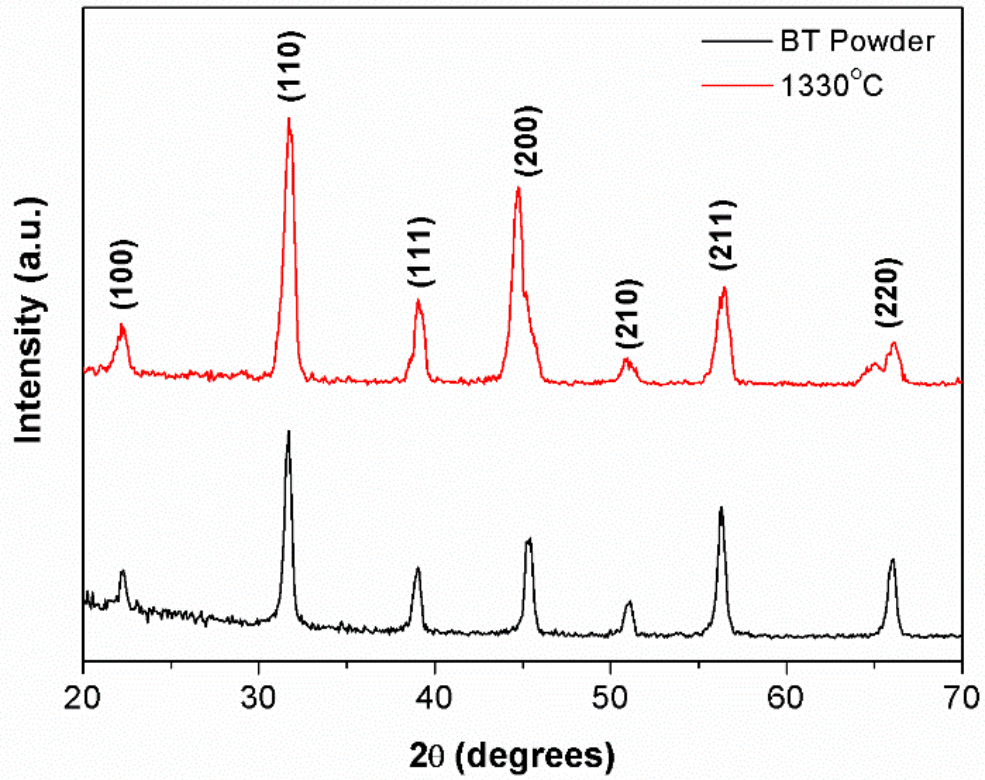


Figure 5.17 The X-Ray diffractometer patterns of BTO powders and sintered samples

Table 5.3 Measured properties of BTO samples fabricated by our process compared with bulk BTO material

| Piezoelectric and Dielectric properties | Printed BTO | Bulk BTO(Pardo, 2011; Kim, 1998; Bechmann, 1956) |
|-------------------------------------------------------|-------------|--------------------------------------------------|
| Curie Temperature T (°C) | 122 | 120 |
| Electromechanical coupling factor K_t | 0.474 | 0.35 |
| Piezoelectric constant d_{33} (pC N ⁻¹) | 160 | 190 |
| Dielectric constant ϵ (1kHz) | 1350 | 1700 |
| Dielectric loss tangent $\tan\delta$ (1kHz) | 0.018 | 0.03 |

To understand the performance of the developed AM process on fabricating BTO components, the dielectric and ferroelectric properties of the sintered samples were measured. Circular Cr/Au electrodes with a diameter of 10 mm were first deposited by sputtering onto the sintered BTO samples as top electrodes. The dielectric properties were then measured using an Agilent 4294A impedance analyzer. The values of dielectric constant ϵ and dielectric loss $\tan \sigma$ of the samples at 1 kHz are 1350 and 0.018 respectively. The measured piezoelectric constant (d_{33}) of the fabricated samples is around 160pC/N. The measured electromechanical coupling coefficient (K_t) is around 0.474. The measured properties were compared with those of bulk BTO material in Table 5.3. As can be seen in the table, both curie temperature and electromechanical coupling factor of the printed BTO component are close to the real values of BTO material. The piezoelectric constant is smaller than the true value but is enough for the component to display piezoelectricity. Both dielectric constant and dielectric loss tangent are influenced by the existing pores in the sintered parts and could be further improved by increasing the final density. Furthermore, it should be noted that the properties of the final materials largely rely on the sintering conditions, such as temperature and dwell time. In figure 5.18, the measured properties of samples sintered at different temperatures were compared, including density, piezoelectric constant d_{33} , dielectric constant and loss tangent. It can be seen that the 1330°C sample owns the best overall properties. In addition, our experiments also indicate that the properties of samples sintered under a shorter dwell time (e.g. 4 hours) are not as good as the ones sintered for 6 hours. The interested reader is referred to (Song, 2017).

Polarization field (P–E) hysteresis properties were also evaluated using a radiant precision materials analyzer (Radiant Technologies, Albuquerque, NM). Figure 19 shows the ferroelectric hysteresis (P-E loop) of the sintered samples under different electric fields. It can be observed that the P-E loop exhibits good symmetry, which suggests satisfactory ferroelectricity of the fabricated samples. The remnant polarization (P_r) are $2.2\mu\text{C}/\text{cm}^2$, $2.4\mu\text{C}/\text{cm}^2$ and $7.0\mu\text{C}/\text{cm}^2$, respectively, when the electric fields are 10kV/cm, 20kV/cm and 30kV/cm.

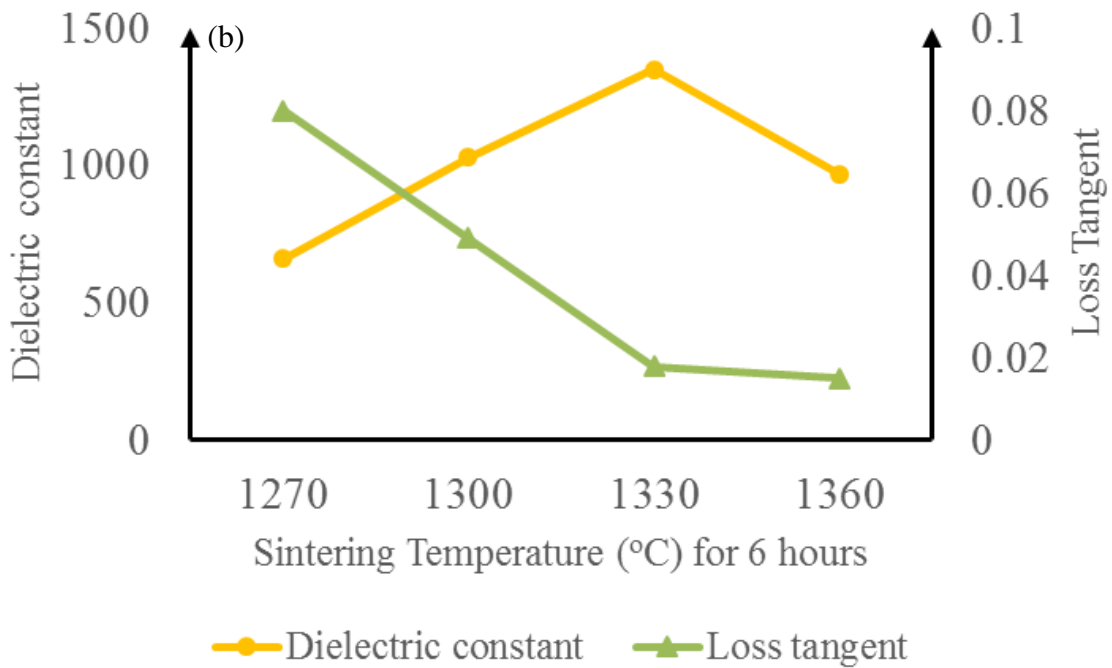
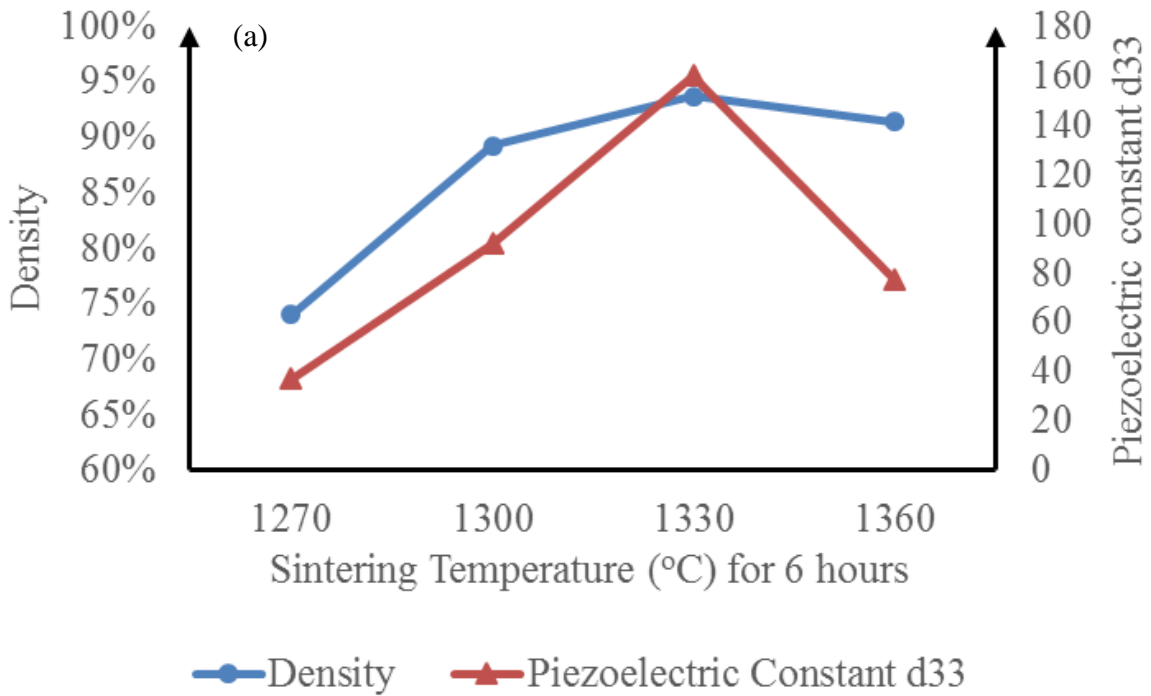


Figure 5.18 Property measurement of samples sintered at different temperature (a) Density and piezoelectric constant (b) dielectric constant and loss tangent

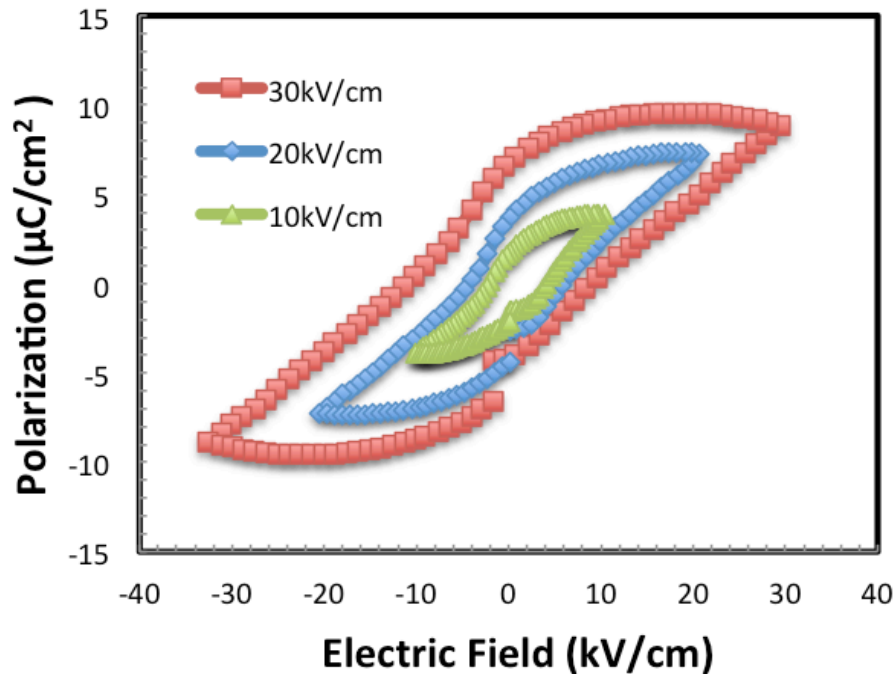


Figure 5.19 Polarization–electric field hysteresis loop of sintered BTO samples

5.3.5.2 Ultrasound Transducer Fabrication and Testing

To further demonstrate the developed AM process, a simple ultrasound transducer was designed and fabricated by using the sintered concave BTO transducer element (figure 5.14) as the piezo layer. The structure of the transducer is shown in figure 20ab.

Poling of the BTO sample was conducted by applying a $2\text{V}/\mu\text{m}$ polarization voltage field on the transducer at 120°C for 30 min. The acoustic performance of the transducer was measured through a pulse-echo test in a deionized water bath at room temperature. In the pulse-echo test (refer to figure 5.20c), the transducer is excited by broadband negative pulses emitted from a pulser/receiver unit (Panametrics PR5900, Olympus NDT Inc., Waltham, MA) and generates ultrasonic signal in the degassed water. This ultrasonic signal is transmitted in the water, and finally reflected by a quartz. After the echo signal is received by the transducer, it will be converted into electrical signal, which will consequently be received by the same pulser/receiver unit. Figure 5.21 shows the received echo signal reflected by a quartz at a distance of about 5mm away from the transducer.

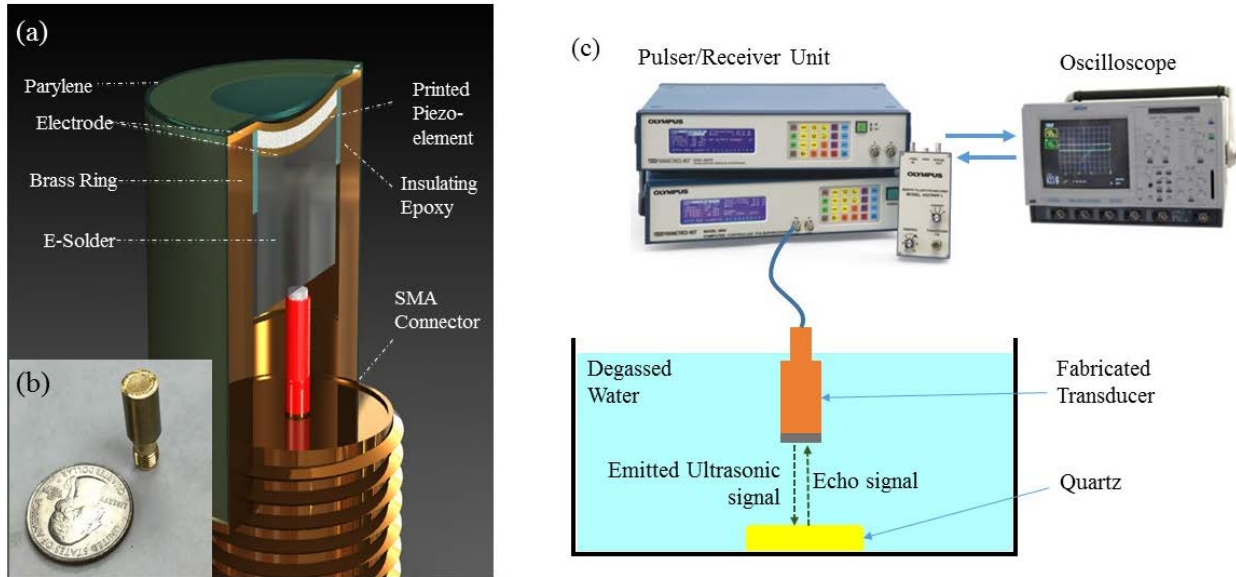


Figure 5.20 Application of a BTO sample in an ultrasound transducer: (a) Schematic diagram of the ultrasound transducer; (b) the transducer assembled with the fabricated BTO sample; (c) pulse-echo test of the fabricated transducer

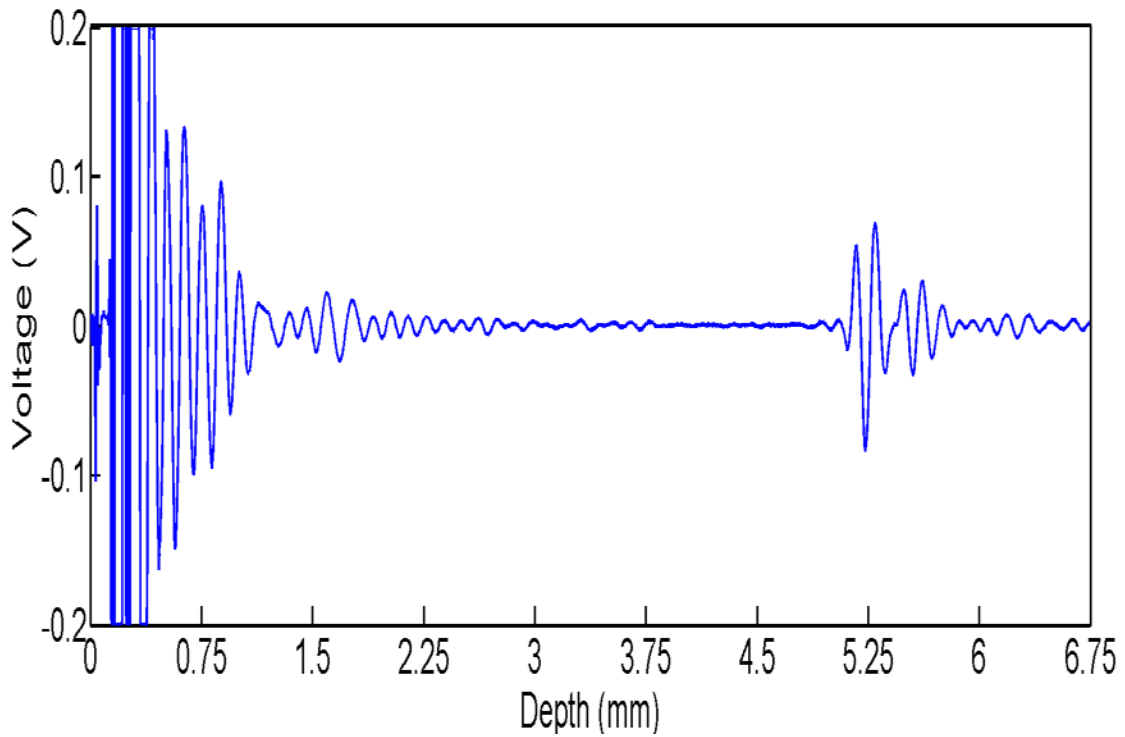


Figure 5.21 Initial pulse and echo generated by the printed focused transducer

The echo electrical signal is then digitized by a 500MHz oscilloscope (LC534, LeCroy Corp., Chestnut Ridge, NY). Figure 5.22a shows the time-domain echo signal and its frequency spectrum. Echo response with an amplitude of 0.3V ($\pm 0.15V$) can be seen from 19.8 μ s to 21 μ s, which indicates the fabricated transducer can effectively achieve the conversion between ultrasonic signal and electrical signal. Center frequency (F_c) of the transducer can be calculated from frequency F_l and F_h at the magnitude of -6 dB in the frequency spectrum as: $F_c = \frac{F_l + F_h}{2} = 6.28\text{MHz}$. The bandwidth (BW) of the transducer can be calculated as: $BW = \frac{(F_h - F_l)}{F_c} \times 100\% = 41.28\%$. According to the center frequency 6.28MHz and bandwidth 41.28%, it can be suggested that the BTO piezo based transducer that was fabricated by the AM process has a good potential for clinic ultrasonic imaging.

Comparing with a flat piezoelectric element, a concave element can focus ultrasound signal at its focus point, at which the strongest signal and the best resolution can be obtained. This property has been proved by our experiment, as shown in figure 5.22b. At the focused location of 15.5mm, the tested sample has the minimum lateral resolution (i.e. $\sim 770\mu\text{m}$) and the maximum echo signal strength (i.e. $\sim 0.301V$).

The principle purpose of the printed 6.28MHz ultrasound transducer is for ultrasound imaging. Figure 5.23 shows an ultrasound microscopy image of a pig eyeball using the fabricated transducer. From the picture one can clearly see the inner structure of the eyeball, including the cornea, its constituent layers, and the anterior and posterior chambers.

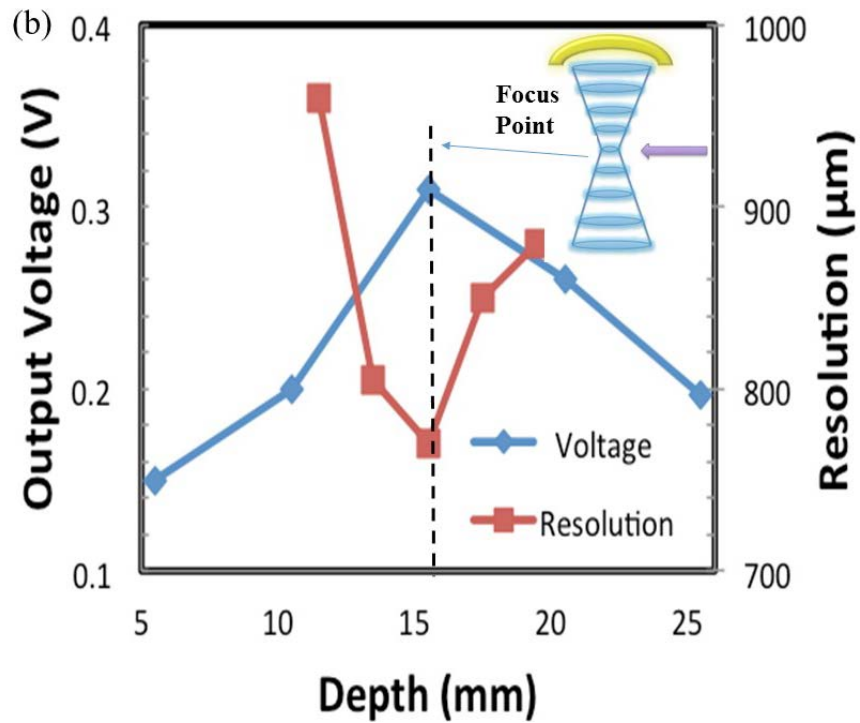
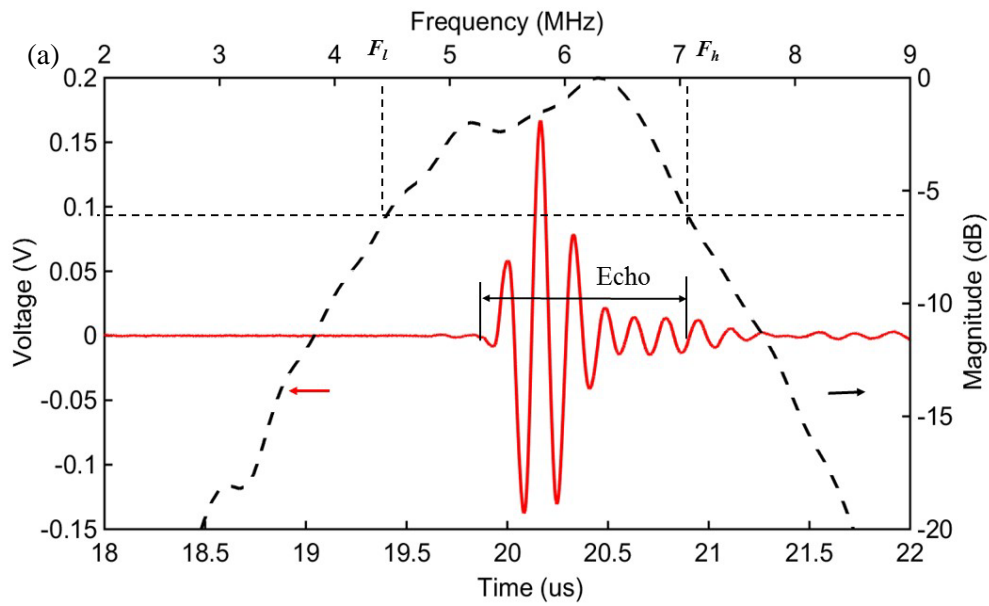


Figure 5.22 (a) Time-domain response and frequency spectrum of echo signal of the fabricated transducer; (b) Voltage and lateral resolution as the function of depth between the transducer and the target

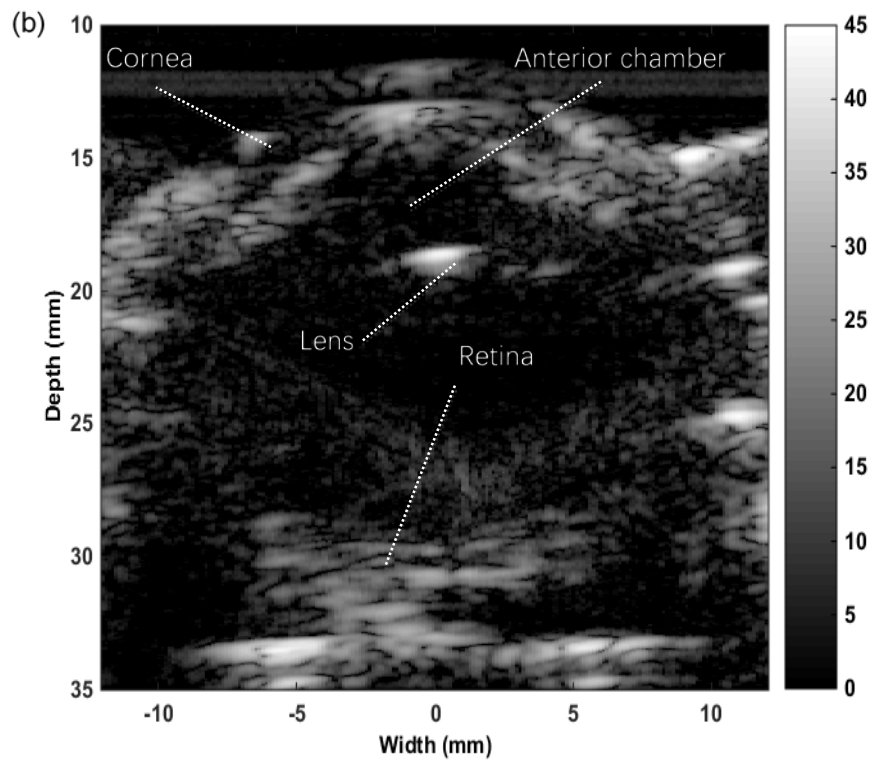
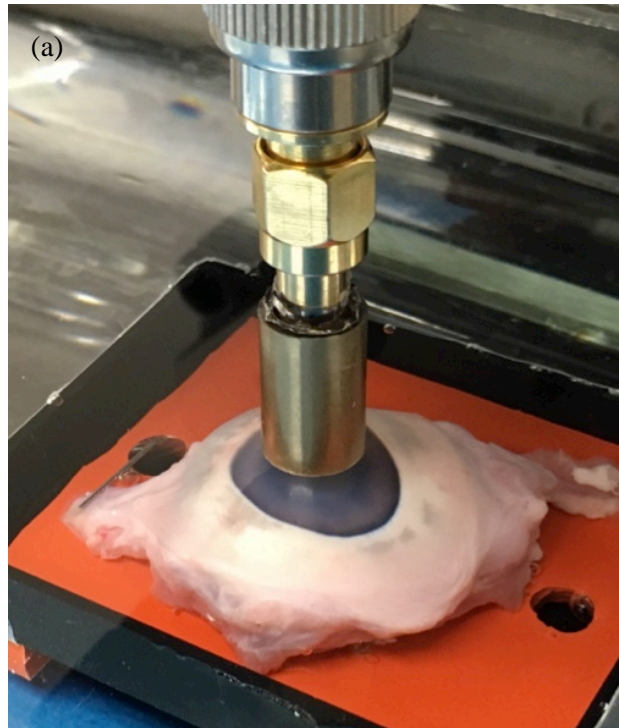


Figure 5.23 (a) The 6.28MHz ultrasonic scan through porcine eyeball using the printing focused transducer. (b) Ultrasonic imaging of porcine eyeball

5.4 Summary

In the chapter, the tape-casting-integrated projection-based SLA process was applied in the fabrication of ceramic components, including alumina and piezoelectric components. The developed process overcomes the problems of high viscosity and low photosensitivity associated with high solid loading slurry by using a slurry recoating method and a sliding motion design. The debinding and sintering processes have been studied for the alumina and BTO green parts. The debinding process is only dependent on the polymers in the green parts. Therefore, the temperature profiles in both types of materials are the same, except that the debinding of alumina is conducted in a vacuum furnace and that of BTO in an argon furnace. The reason that we used a different furnace to process BTO samples is that they have a weaker inter-layer bonding force than alumina, due to a smaller cure depth of BTO material, and the vacuum degree of the vacuum furnace used in our process is not high enough to prevent crack and delamination of a green part during its debinding.

After debinding and sintering, the final alumina part has a density of 93.2% of true alumina density with a dimensional shrinkage of ~22.7%. The final BTO annular transducer array has a density of 93.7% with a dimensional shrinkage of ~26.7%. Measured dielectric and piezoelectric properties of the final BTO samples suggest great potentials of the developed AM process in fabricating piezoelectric components that can be applied in functional devices such as ultrasound transducers. The new fabrication process would enable the development of novel piezoelectric sensors and actuators through the use of 3d printed BTO components in much more complex shapes.

Chapter 6 Post Processing for Porous Structure Fabrication

6.1 Introduction

Porous structure, also known as foam structure, is defined as a multi-scale structure which has a lot of interconnected micro pores randomly distributed inside a relatively big dimension of volume. These interconnected micro pores introduce many benefits to the structure, such as low density, low thermal conductivity, high surface area and efficient stress transmission. By making use of these properties, porous structures have a wide variety of industrial application such as oil absorption (Choi, 2011; Zhang, 2013), heating/electromagnetic/sound shielding (Chen, 2013a; Yang, 2005), sensing and energy harvesting (Marselli, 1999; Dai, 2012; Cha, 2011; Kara, 2003; Boumchedda, 2007; Lin, 2011), tissue engineering (Hutmacher, 2000; Rodriguez, 2012) and sandwich structure (Daniel, 2011; Hung, 2014; Patrick, 2012), as described in figure 6.1.

Due to their considerably wide range of usage, plenty of research papers have been reported on novel processing technologies to fabricate foam structures with desired porosity. The most common approaches of making foam structures include templating method (Chen, 2013b; Shastri, 2000; Lee, 2005) and foaming agent-based method (Choi, 2011; Chen, 2013a; Marselli, 1999; Ramay, 2003; Fukasawa, 2001; Liao, 2002; Mikos, 1994; Hou, 2003; McCall, 2014; Lin, 2013; Dey, 2011; Bai, 2014). The templating method builds a foam structure from an existing porous template. The template is then removed by dissolving the entire structure in a certain type of solution. The foaming agent-based method is the most widely used approach for the preparation of foam structures with high porosity and is usually employed to process polymer and ceramic materials. In the foaming agent-based method, a specific type of foaming agent is mixed with the matrix materials and a green part is fabricated from the mixture. The green part is then post-processed to remove the foaming agent in the volume, such that interconnected pores can be generated in place of

foaming agent. Foaming agent varies in different research, but generally employs heat-decomposable or soluble particles. For example, Choi et al.(Choi, 2011) and McCall (McCall, 2014) use commercially available sugar as foaming agent to make highly porous polymer composite. In their method, free sugar is added directly to uncured polymer composite. After a thin layer is cured from the mixture, the sugar particles are removed by soaking the cured composite layer in hot water, leaving a three-Dimensional (3D) isotropic network of air channels in the polymer composite. Both templating and foaming agent methods can achieve high porosity in the final components. However, these methods can only deal with simple porous structures, such as a thin layer, and have limited capability of fabricating complex 3D geometries.

Vigorous research studies have been conducted to directly make novel porous structures by Additive Manufacturing (AM) technologies, but the porosity that can be achieved by AM processes is still limited by their relatively small resolution in the fabrication of multi-scale features. For example, for Stereolithography (SLA) process, it is extremely difficult to fabricate a macro-scale component with a large number of micro-scale pores, due to the large overcure in both depth and width (Song, 2012).

In this research, we presented a SLA-based sugar foaming method to fabricate complex 3D porous structures. In our method, micro sugar particles, as foaming agent, are mixed with photosensitive resin or composites and thus form a viscous mixture of sugar and resin/composites. A desired geometry is then fabricated from the mixture with the presented slurry-based SLA process. Similar to ceramic fabrication, the fabricated component is called *green part*. The resin or composite is called *body material*. To obtain micro pores in the green part, a boiling process is performed afterwards. In the boiling process, the green part is soaked in hot water for a certain amount of time. The sugar particles inside the green part will gradually dissolve in the hot water until a porous polymeric or composite structure is obtained. To facilitate sugar removal in the hot water, special patterns are designed on the fabricated parts with thin yet strong features.

The remainder of this chapter is organized as follows. The green part fabrication process is described in the section 6.2. Process parameters such as solid loading, blade coating height and curing time are

analyzed in section 6.3. Section 6.4 discusses the minimum thin feature that can be fabricated by the presented process and demonstrates some pattern designs to support the thin features. Section 6.5 analyzes the application of this method in the fabrication of porous scaffolds in tissue engineering.

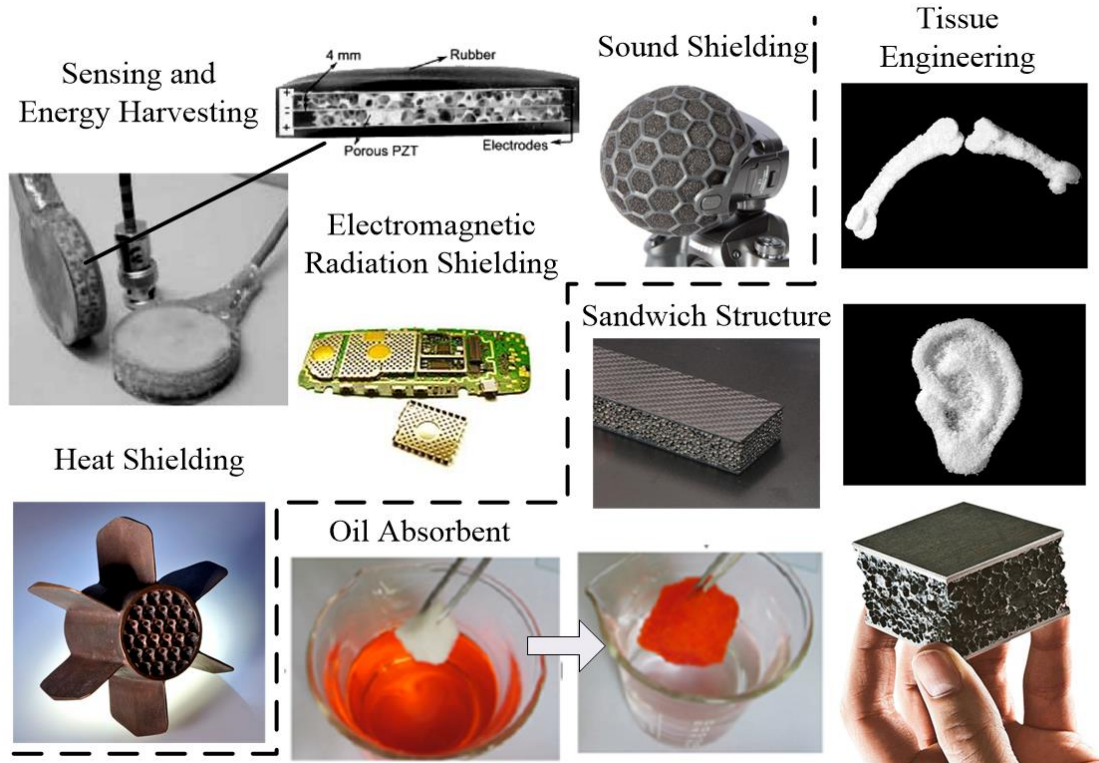


Figure 6.1 Applications of various foam structures

6.2 Process description

In the fabrication process of porous structures using slurry-based SLA, sugar particles serve as foam agent. The sugar used in the process is bakery sugar, purchased from King Arthur Flour. The size of each particle is around $\sim 150\mu\text{m}$, which can dissolve quickly and completely in water. The photosensitive resin (EnvisionTEC SI500) is used as the matrix material in the experiments. The resin has a viscosity of 180cP and a density of $1.1\text{g}/\text{cm}^3$ under the room temperature (EnvisionTec, 2012). The resin-sugar mixture is prepared in the following steps: The sugar is first deagglomerated using a mortar and pestle. A certain weight ratio of sugar is added into resin and mixed uniformly with a stirring rod for 30 minutes.

The addition of sugar into the resin will lead to dramatic increase in the viscosity. As discussed in chapter 1, current SLA processes require the viscosity of the material to be smaller than 3000mPa•s. A larger viscosity will make the refill of the material extremely difficult, such that new layers cannot be fabricated successfully. Therefore, it is necessary to use the slurry-based SLA process to fabricate the viscous mixture.

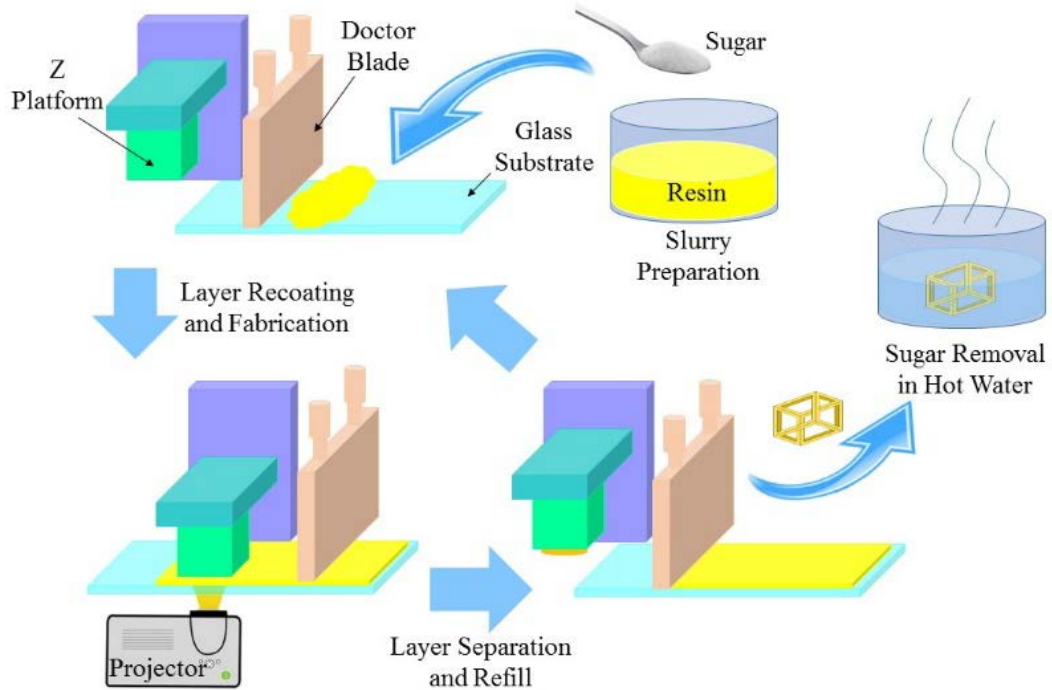


Figure 6.2 Schematics of the dynamic sugar templating method based on slurry-based SLA

As depicted in figure 6.2, when a fabrication cycle of one layer begins, a few amount of resin-sugar mixture is dispensed onto the glass substrate behind the doctor blade. A green part can be consequently built layer by layer by following the procedure described in chapter 3.5. After a green part is finished, it is soaked in boiling water for a certain amount of time to remove the sugar, and a 3D porous structure can thus be obtained.

6.3 Main process parameters

In this section, we discuss main process parameters associated with the green part fabrication in the SLA-based sugar foaming method. The fabrication of a green part is greatly influenced by the process parameters, such as solid loading of sugar in the mixture, doctor blade height, and curing time used in the SLA process. The effect of each parameter on the process as well as their design methods are presented as follows.

A tape casting process is conducted to coat the resin-sugar mixture into a slurry layer. The recoated slurry layer is required to be thin and uniform, such that enough light can penetrate through the material to solidify the layer and the layer can ultimately bond tightly with the previous layers. Furthermore, after a layer of resin-sugar mixture is recoated on the glass substrate, the Z platform moves down to press the recoated layer into a desired layer thickness. When the thickness of the recoated slurry layer is large, it will break small features on the part that has been fabricated more easily during the pressing process. To avoid the damage of small features, a smaller thickness of layer recoating is preferred. Doctor blade height is a parameter that determines the thickness of the recoated layer. It is suggested in chapter 4.2 that the doctor blade height should be two times bigger than the recoated layer thickness.

In order to obtain a component with higher porosity, a higher solid loading of sugar is desired for the resin-sugar mixture. However, more sugar gives rise to an increase in the viscosity of the mixture and makes the layer recoating more difficult, especially when the height of the doctor blade is small. To identify the optimal solid loading and blade height for the resin-sugar mixture, we investigated the slurry recoating under different combinations of sugar ratio and blade height, as shown in table 6.1. Four different solid loadings are chosen from 40wt% to 70wt%. The blade height is set to 0.2mm, 0.4mm, 0.6mm and 0.8mm respectively. The same amount of material was dispensed for each combination of solid loading and blade height and the glass substrate moves underneath the doctor blade with the same speed. As can be seen in the table, a blade height of 0.2mm is too small to achieve a uniform layer recoating of any solid loading used in our tests. As the blade height increases, the recoated layer gets thicker but the uniformity gets

improved. Although a bigger solid loading (e.g. 70wt%) is desired to yield higher porosity, it can't be coated with the doctor blade successfully (refer to solid loading 60wt% and 70wt% in table 6.1). Among all the combinations of sugar ratio and doctor blade height, 50wt% and 0.4mm are the optimal settings with the biggest sugar percentage and the smallest recoated layer thickness. In the following experiments, 50wt% and 0.4mm are chosen as the solid loading and doctor blade height, with which a thin and uniform layer can be recoated.

Table 6.1 Slurry coating with different blade height and solid loadings

| Sugar ratio/ Blade height(mm) | 40% | 50% | 60% | 70% |
|-------------------------------------|-------------------------------------------------------------------------------------|-------------------------------------------------------------------------------------|--------------------------------------------------------------------------------------|---------------------------------------------------------------------------------------|
| 0.2 |  |  |  |  |
| 0.4 |  |  |  |  |
| 0.6 |  |  |  |  |
| 0.8 |  |  |  |  |

In order to decide the layer thickness for slicing the Computer-Aided Design (CAD) model, curing characteristics of the resin-sugar mixture with different weight ratios are studied, as depicted in figure 6.3.

In the experiments, enough slurry with different weight ratios was uniformly spread on the glass substrate. An image of a circle with a diameter of 10mm was projected onto the bottom of the substrate for a certain amount of time from 1s to 5s to cure the spread slurry. The thickness of the cured layer was measured with a micro caliper and is recorded as cure depth of the tested material under the given cure time. The measured thickness (or cure depth) of different materials with respect to different cure time was plotted in the figure 6.3.

It can be seen in figure 6.3 that the pure resin has the smallest cure depth, comparing with the resin-sugar mixture. For the same material, cure depth increases with the curing time, since more light energy is exposed under a longer cure time. As the solid loading of sugar in the mixture increase, the cure depth becomes bigger. This is because the amount of energy that is lost when light pass through a sugar particle is smaller than the energy that is absorbed when the light cures the same volume of resin. Hence the light can go deeper into the slurry with more sugar particles, resulting in a bigger cure depth of the mixture with a bigger solid loading.

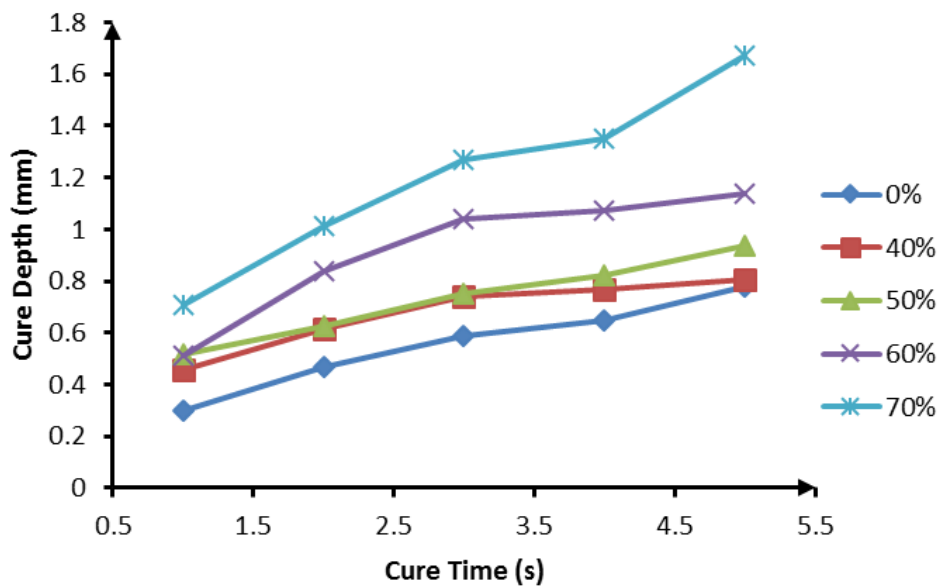


Figure 6.3 Cure depth with different cure time for different solid loadings

6.4 Sugar removal

After the part is fabricated by the presented process, it contains both sugar and body material. In next step, a boiling process should be used to dissolve the sugar in hot water and generate pores in place of the sugar particles inside the part. In order to remove the sugar particles efficiently, the printed features should be thin enough; otherwise some of the sugar particles would be trapped in the body and could not be removed during the boiling process. In this section, we will discuss design of porous structures with the optimal feature size, which can be built by the process.

We use a cylindrical shell structure (refer to figure 6.4a) and pure resin to study the minimum feature that can be fabricated by our process. The outer diameter of the shape is 8mm. The height of the model is 3mm. The thickness of the shell changes from 0.2mm to 0.6mm. All the fabrication results are shown in figure 6.4b. It can be seen in the figure that both shell structures at the thickness of 0.4mm and 0.6mm can be made, while some portions of the fabricated shells at the thickness of 0.2mm and 0.3mm got broken, as shown in the last image of figure 6.4b. That is because the parts with the shell thickness of 0.2mm and 0.3mm were too weak to survive when they moved inside the viscous slurry. The experiment suggests that the minimum feature that can be fabricated by our process without any damage is around 0.4mm. However, since the particle size is around 150 μ m, a smaller feature thickness (e.g. 0.2mm) is desired to completely remove the sugar. To avoid the damage of thinner features below 0.4mm during the fabrication, we designed different patterns to support the weak structures, as shown in figure 6.5.

The thickness of the outer shells of the three parts in figure 6.5 is 0.2mm. The shells have the same diameter as the one in figure 6.4a, but were inserted three different types of pattern designs inside. The pattern structure can support the thin features and retain the shape of the shell during the fabrication.

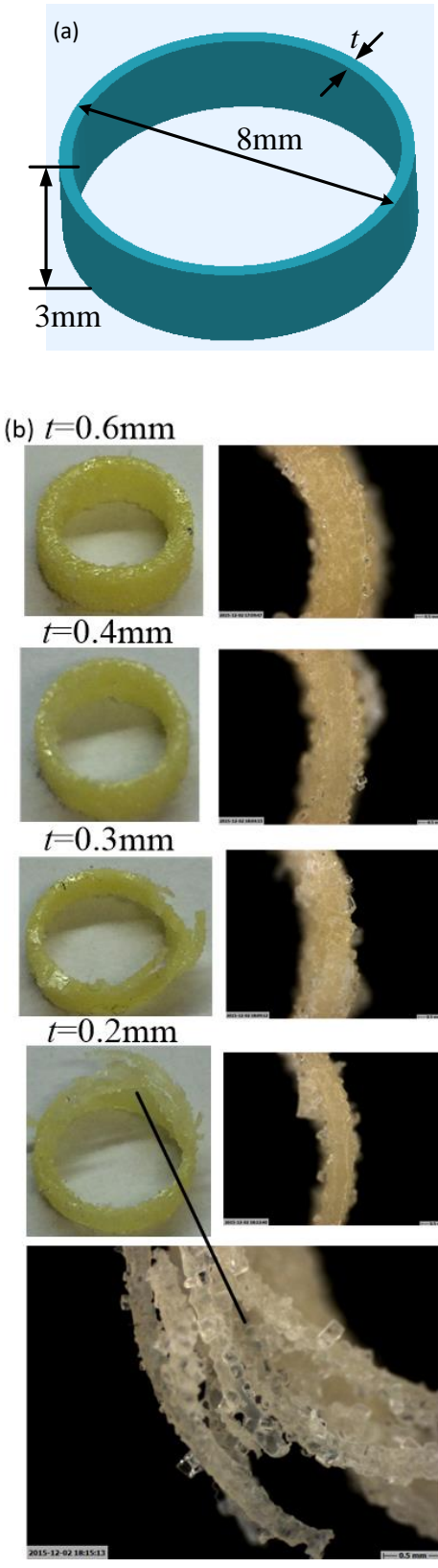


Figure 6.4 Cylinder shell structures with different thickness

To demonstrate the sugar removal process, we used the first pattern design in figure 6.5 and fabricated three samples with a shell thickness of 0.2mm, 0.3mm and 0.4mm respectively. All the fabricated parts were cleaned with alcohol in an ultrasonic cleaning machine for 10 minutes. The cleaned components were then dried in the air for 1 hour. After that, all the three samples were put in boiling water to remove the sugar particles for 2 hours. The weight of each sample was measured before (w_1) and after (w_2) the boiling. Assume the weight ratio of the sugar in the mixture is Φ , the density of the sugar and resin is ρ_s and ρ_r respectively. Then the porosity φ can be calculated as

$$\varphi = \frac{(w_1 - w_2) \cdot \rho_s}{w_1 \cdot \Phi \cdot \rho_s + w_1 \cdot (1 - \Phi) \cdot \rho_r} \quad (6.1)$$

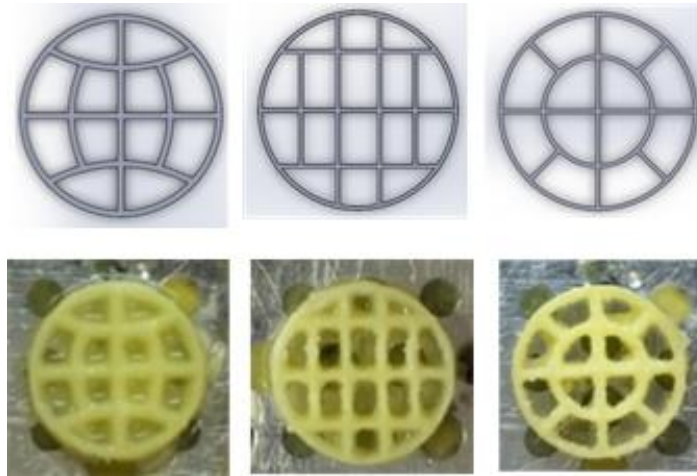


Figure 6.5 Different support patterns for thin features

The measured weights of each sample before and after the boiling are listed in table 6.2. The porosity after 2 hours' boiling is calculated using equation (6.1). The density of the sugar we used in the calculation is 1.587 g/cm^3 . As shown in table 6.2, the achieved porosity is approximately 58%. Although the weight change may contain loss of the polymer portion in the sample during the water boiling and will thus introduce errors in the calculated porosity, the result could still suggest an increase of porosity in the final parts. Similar ratios of weight loss in the three samples also suggest the weight loss of polymer should be small. The pores that were generated after the removal of the sugar are shown in the figure 6.7b.

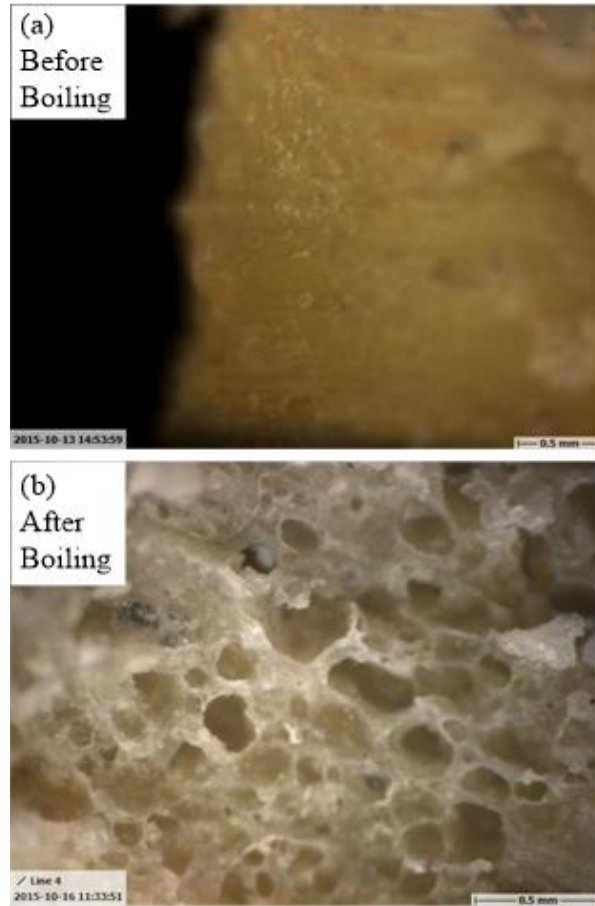


Figure 6.6 Microscope image after sugar removal

Table 6.2 Sample weight changes after boiling

| Sample Thickness (mm) | Weight before boiling w_1 (g) | Weight after boiling w_2 (g) | Porosity after 2h |
|-----------------------|---------------------------------|--------------------------------|-------------------|
| 0.2 | 0.057 | 0.029 | 58.0% |
| 0.3 | 0.088 | 0.051 | 49.7% |
| 0.4 | 0.122 | 0.064 | 56.15% |

6.5 Test cases

An important application of our method is to increase the porosity of scaffolds fabricated by stereolithography process in tissue engineering. Tissue engineering emerged in the early 1990s to conduct tissue/organ repair by transplanting a biofactor (cells, genes and/or proteins) within a porous degradable material known as a scaffold (Hollister, 2005). Numerous research studies have indicated that more tissue ingrowth and new bone formation in vivo occurred in areas with higher porosity (Karageorgious, 2005). Although SLA process has been used in the fabrication of porous scaffolds (Gauvin, 2012; Cooke, 2003), the porosity that can be achieved is limited by the resolution of the process.

A scaffold design is given in figure 6.8. The edge length of pores is a and the width of a strut in the scaffold is b . The thickness of a single layer of the scaffold is set to b , and the distance between two scaffold layers is a . Assume the number of pores along all directions is n . Theoretically the porosity φ of the scaffold can be calculated as:

$$\varphi = \frac{a^3 n^3 + 3a^2 b n^2 (n+1)}{(n \cdot a + n \cdot b + b)^3} \quad (6.2)$$

When fabricated by our tape casting integrated slurry-based SLA process in a bottom-up projection manner, the actual pores will be smaller than the desired size both in XY plane and along Z direction, due to the width and depth overcure of the light. For simplicity, we assume the overcure in the XY plane is proportional to the length of a feature with a ratio of η_{xy} , and the overcure along Z, which occurs at the overhung features, is proportional to the thickness of the overhung feature with a ratio of η_z , as depicted in the figure 8. Then in the actual structure fabricated by our process, strut width will increase from b to $b(1 + \eta_{xy})$, and the edge length of each pore will decrease from a to $(a - b \eta_{xy})$. The thickness of the first layer of the scaffold keeps constant at b , but all the other layers increase from b to $b(1 + \eta_z)$ and the distance between two neighboring layers decrease from a to $(a - b \eta_z)$. Then the actual porosity of the scaffold fabricated by our process can be calculated as:

$$\varphi = \frac{(a-b\eta_{xy})^2(bn^2+bn^3+an^3)+2(a-b\eta_z)(a-b\eta_{xy})b(1+\eta_{xy})n^2(n+1)}{(n \cdot a+n \cdot b+b+b\eta_{xy})^2(n \cdot a+n \cdot b+b)} \quad (6.3)$$

Pore size used in scaffolds is typically designed in the range of 100-600 μ m in order to optima for bone-related outcomes (Karageorgious, 2005). Then the following constraints should be satisfied for the designed scaffold:

$$a - b\eta_{xy} \in [100,600]\mu m$$

$$a - b\eta_z \in [100,600]\mu m$$

$$\eta_{xy}, \eta_z \in [0,1]$$

$$\eta_{xy} = f(b)$$

$$\eta_z = g(b)$$

The overcure in the SLA process gives rise to a lower porosity in the scaffold directly fabricated by the process. For example, in the case of a scaffold with designed pore size $a=300\mu$ m, designed strut width $b=300\mu$ m, $n=100$, and η_{xy} can be identified by an experiment as 30%, the actual porosity φ is calculated as 26.5% and a pore size of 200 μ m is achieved in the final part.

By using the sugar foaming method, we can further increase the porosity of the final scaffold. When the actual porosity that can be achieved by the SLA process is φ_a . As shown in the section 6.4, a porosity of $\varphi_{\text{sugar}}=50\%$ can be obtained using our sugar foaming method. Then after applying the sugar foaming method to the designed scaffold structure, the combined porosity in the final scaffold is:

$$\varphi_a + \varphi_{\text{sugar}} - \varphi_a\varphi_{\text{sugar}} \quad (6.4)$$

Then the incremental ratio δ of the final porosity with respect to the one directly fabricated through the SLA process is:

$$\delta = \frac{\varphi_{\text{sugar}}}{\varphi_a} - \varphi_{\text{sugar}} \quad (6.5)$$

When $\phi_{\text{sugar}} = 50\%$ and $\phi_a = 26.5\%$ as calculated in the above example, the ratio δ can be as high as 138.7%.

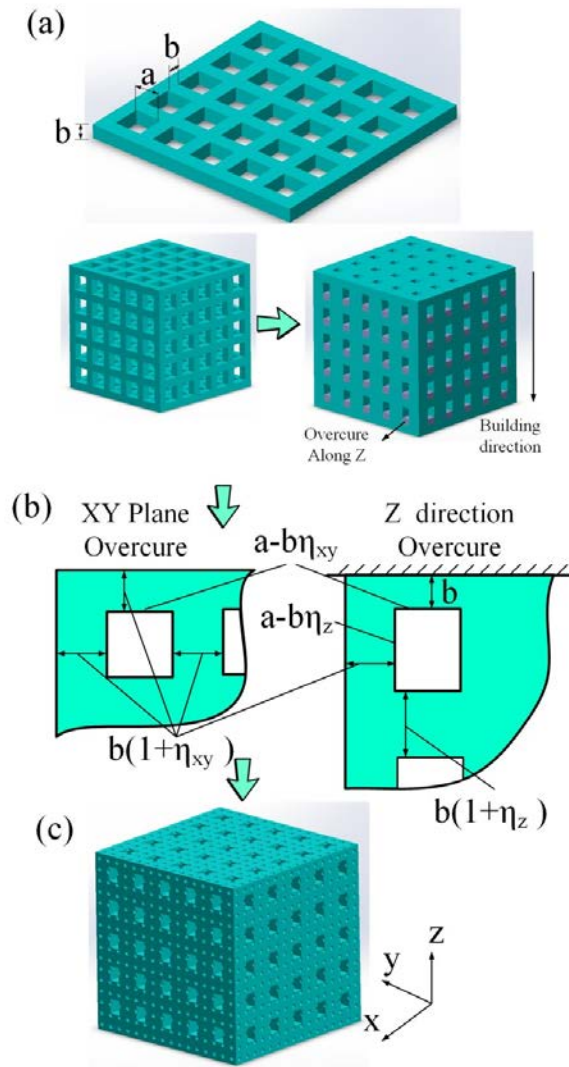


Figure 6.7 Increase porosity by the sugar foaming method

We used the 65wt% glass composite discussed in chapter 4.6 as an example to further demonstrate the sugar foaming method in the fabrication of composite material. The reason that we selected this composite is that it has a relatively large cure depth ($\sim 590\mu\text{m}$) compared with the particle size of sugar. The glass composite was mixed with sugar particles at a weight ratio of 40%. The layer thickness during the fabrication is selected as $200\mu\text{m}$. The green part was soaked in hot water (80°C) for about 40 minutes. Figure 6.9c and

6.9d show the microstructures of the green part and figure 6.9e and 6.9f are the structures after the post processing. The weight of the composite foam decreases from 1.004g to 0.783g after the boiling. The density of the glass composite is calculated as 1.472 g/cm^3 . From equation 6.1 we can compute the porosity of the final scaffold as 23%. A higher porosity may be obtained by increasing the sugar concentration and the boiling time.

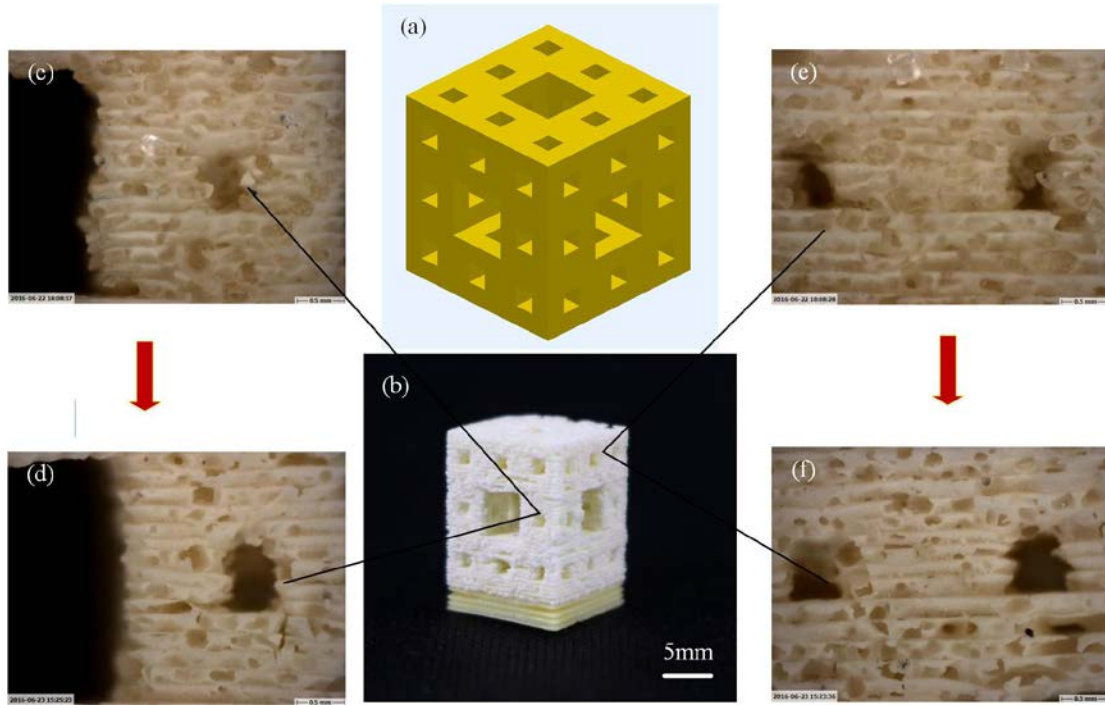


Figure 6.8 Glass composite foam structure fabrication by the slurry-based SLA

6.5 Summary

A sugar foaming method is used to post process the green parts fabricated by the slurry-based SLA and generate porous structures. The material is prepared by mixing sugar particles with photosensitive resin or composites. The mixture is then used in the tape-casting integrated slurry-based SLA process to produce 3D components. Different process parameters were discussed to allow for the fabrication of resin-sugar slurry, including solid loading, blade height, curing time, layer thickness, etc. In order to remove the sugar particles efficiently, a part is printed as thin features with specifically designed internal patterns as the support. The

sugar particles within the printed components are dissolved in boiling water, such that pores can be generated in the final part. Our experiment indicates a porosity of 50% can be achieved with the current process parameters. The application of this method in tissue engineering is discussed to increase the porosity of scaffolds that are fabricated by current SLA process.

Chapter 7 Conclusions and recommendations

Ceramic and composite components are materials of particular interest to engineers due to their unique physical properties. The development of additive manufacturing (AM) has led to technological advances in the fabrication processes of these materials. In this dissertation, particular emphasis is directed to slurry-based stereolithography (SLA) process, which offers the potential to reliably produce accurate ceramic and composite components through careful control of viscous slurry flow. We examined technique problems associated with this method in the fabrication of ceramic and composite materials and demonstrated its capability of building complex geometries with desired properties. In this chapter, we reviewed the research questions and hypothesis as presented in chapter 1. We also discussed main contributions of our work in the dissertation and gave recommendations for future research that could move the technology forward.

7.1 Answering the Research Questions and Testing Hypothesis

To verify two main hypotheses, we subdivided the two main research questions into three sub-questions and come up with a sub-hypothesis corresponding to each sub-question. Each hypothesis is tested in prior chapters as follows:

Hypothesis 1.1 *A slurry mixture without any dilute solvent added will help avoid large deformation and big shrinkage in the post processes.*

Hypothesis 1.2 *Recoated layer thickness is restricted by slurry viscosity, which can be reduced by increasing shear rate on the slurry.*

Hypothesis 1.3 *Separation force becomes less by using sliding mechanism than by direct pull-up.*

To verify hypothesis 1.1, the slurry formulation and its preparation method was presented in chapter 3.1. Several test cases were shown in chapter 4 and chapter 5, including composite capacitors, alumina components and piezo-electric elements. Both the composite components and the ceramic green parts indicate enough strength compared with the ones fabricated from diluted slurry.

To verify hypothesis 1.2, both curing and rheological characteristics of the slurries were studied in chapter 3.2 and 3.3. In particular, the relationship between solid loading (viscosity) and blade recoating were presented. A bottom-up projection based SLA process was integrated with tape casting process to facilitate the layer recoating of viscous slurry. Process parameters including doctor blade height, recoating speed, layer pressing speed, separation speed, etc., were discussed in chapter 4.

To verify hypothesis 1.3, the sliding mechanism was implemented in the tape-casting integrated SLA process. The sliding mechanism was described in chapter 3.5 and the related parameters (i.e. separation speed) were analyzed in chapter 4.3.

Hypothesis 2.1. The debinding process should be conducted slowly in order to avoid cracks and delamination, and the sintering process should be in an air atmosphere.

Hypothesis 2.2. Properties for both structural (e.g. strength and hardness) and functional (e.g. piezoelectricity) purposes can be achieved by debinding and sintering a green part fabricated by slurry-based SLA.

Hypothesis 2.3. Sugar foaming method can help increase the porosity of a foam structure fabricated by SLA.

To verify hypothesis 2.1, different debinding and sintering conditions were studied to achieve high density in the final parts without any crack and delamination. The debinding and sintering processes for alumina and barium titanate (BTO) were given in chapter 5.2 and 5.3. In particular, the piezoelectric properties of BTO components fabricated with different debinding and sintering conditions were tested and compared in chapter 5.3.5.

To verify hypothesis 2.2, both structural and functional ceramic materials were tested, including alumina and BTO. Their processing methods can be extended to many other ceramics, such as calcium phosphate, Lead zirconate titanate (PZT), zirconia, etc. A density of 93% or more was achieved in the final ceramic components.

To verify hypothesis 2.3, different process parameters were discussed to allow for the fabrication of resin-sugar slurry. Thin features with special internal patterns were designed in order to remove the sugar particles efficiently. A porosity of 50% was achieved with the current process parameters. The application of this method in tissue engineering is discussed to increase the porosity of scaffolds that can be achieved by current SLA processes.

7.2 Contributions and Intellectual Merit

Main contributions of our work can be summarized as follows:

- (1) Used bottom-up projection-based SLA to process viscous slurry materials. Integrated tape casting process into the system for layer recoating.
- (2) Solved the technical problems associated with the developed process in fabricating viscous slurries, including layer curing, layer recoating, layer detachment, etc.
- (3) Established analytical models for main process parameters and provided parameter design methods for the process. Applied the process in the fabrication of high dielectric capacitors.
- (4) Provided post processing methods for the fabrication of structural and functional ceramics, including alumina and barium titanate. Specifically, ultrasound transducer was fabricated using the presented methods.
- (5) Provided post processing methods for the fabrication of porous structures.

7.3 Recommendations for Future Work

Slurry-based AM process is a promising approach of fabricating ceramic and composite materials with desired physical properties. In future, more work can be done in the following aspects.

- (1) Surface finish and fabrication speed. Solid particles in the composite slurry diffuse the incident light outwards in all directions, and reduce the resolution at the boundary of a layer. A big cure time will yield gel around the boundary. The gel along the contour of a cured layer contributes to obvious “staircase effect” on the surface of green parts. Using a smaller cure time could avoid the gel, but can also reduce cure depth at the same time. In the next step, work can be done to improve the surface finish by optimizing the image projection and developing new fabrication strategies. In addition, in the current process, it takes around one minute to fabricate one layer. That is because both material dispensing and layer recoating are required for each single layer. Future work can also include improving the process to make it faster.
- (2) Quality control for slurry-based SLA. An issue with ceramic fabrication using slurry-based SLA method is its big shrinkage. Actually shape deformation happens in most AM processes. In future, geometric shape error control methods can be studied to optimize the final geometric accuracy.
- (3) Consolidation for functional ceramic fabrication. Compared with the piezoelectric components that are fabricated by the traditional manufacturing processes, the BTO components fabricated the AM process still have inferior piezoelectric properties. At this stage, the final part density is restricted by the maximum solid loading of BTO in photocurable resin that will allow light to pass through and be able to recoat. To further improve the piezoelectric properties, future work can 1) investigate different methods to increase the maximum solid loading of BTO slurry, such as using more powerful light energy, enhancing photosensitivity of BTO slurry, etc; 2) improve poling and electrode plating processes; and 3) study the benefits of using complex geometry in piezo component design to enhance transducers’ ultrasonic performance.

(4) Process-property-structure relationships. By adding solid fillers with diverse properties into liquid resin, it becomes possible to obtain green parts with desired functionality. Thanks to the benefits of additive manufacturing in fabricating complex geometries, special structures can now be designed to achieve customized properties and functions. Further work can be done to explore the relationships between special structures and properties. In addition, our process has great potentials in fabricating various fiber-based polymeric composites with enhanced physical properties, whose dependence on the fabrication process can be further studied in the future.

Reference

- [1] Abouliatim, Y., Chartier, T., Abelard, P., Chaput, C. and Delage, C., 2009. Optical characterization of stereolithography alumina suspensions using the Kubelka–Munk model. *Journal of the European Ceramic Society*, 29(5), pp.919-924.
- [2] Akhnak, M., Martinez, O., de Espinosa, F.M. and Ullate, L.G., 2002. Development of a segmented annular array transducer for acoustic imaging. *Ndt & E International*, 35(7), pp.427-431.
- [3] Aota, Y., Tanifuji, S., Oguma, H., Kameda, S., Nakase, H., Takagi, T. and Tsubouchi, K., 2007, October. P1H-4 FBAR Characteristics with AlN Film Using MOCVD Method and Ru/Ta Electrode. In *Ultrasonics Symposium*, 2007. IEEE (pp. 1425-1428). IEEE.
- [4] Bai, C.Y., Deng, X.Y., Li, J.B., Jin, Y.N., Jiang, W.K., Liu, Z.M. and Li, Y., 2014. Fabrication and properties of cordierite–mullite bonded porous SiC ceramics, *Ceramics International*, 40(4), pp.6225-6231.
- [5] Bakarich, S.E., Gorkin III, R., in het Panhuis, M. and Spinks, G.M., 2014. Three-dimensional printing fiber reinforced hydrogel composites. *ACS applied materials & interfaces*, 6(18), pp.15998-16006.
- [6] Bandyopadhyay, A., Panda, R.K., McNulty, T.F., Mohammadi, F., Danforth, S.C. and Safari, A., 1998. Piezoelectric ceramics and composites via rapid prototyping techniques. *Rapid Prototyping Journal*, 4(1), pp.37-49.
- [7] Bechmann, R., 1956. Elastic, piezoelectric, and dielectric constants of polarized barium titanate ceramics and some applications of the piezoelectric equations. *The Journal of the Acoustical Society of America*, 28(3), pp.347-350.
- [8] Becker, E., Ehrfeld, W., Haggmann, P., Maner, A. and Münchmeyer, D., 1986. Fabrication of microstructures with high aspect ratios and great structural heights by synchrotron radiation lithography, galvanofarming, and plastic moulding (LIGA process). *Microelectronic engineering*, 4(1), pp.35-56.

- [9] Bergmann, C., Lindner, M., Zhang, W., Koczur, K., Kirsten, A., Telle, R. and Fischer, H., 2010. 3D printing of bone substitute implants using calcium phosphate and bioactive glasses. *Journal of the European Ceramic Society*, 30(12), pp.2563-2567.
- [10] Bergström, L., 1996. Rheological properties of concentrated, nonaqueous silicon nitride suspensions. *Journal of the American Ceramic Society*, 79(12), pp: 3033-3040.
- [11] Bertsch, A., Bernhard, P., Vogt, C. and Renaud, P., 2000. Rapid prototyping of small size objects. *Rapid Prototyping Journal*, 6(4), pp.259-266.
- [12] Bertsch, A., Jiguet, S., Hofmann, H. and Renaud, P., 2004. Ceramic microcomponents by microstereolithography. In *Micro Electro Mechanical Systems, 2004. 17th IEEE International Conference on.(MEMS)* (pp. 725-728). IEEE.
- [13] Bhimasankaram, T., Suryanarayana, S.V. and Prasad, G., 1998. Piezoelectric polymer composite materials. *CURRENT SCIENCE-BANGALORE-*, 74, pp.967-976.
- [14] Bian, W., Li, D., Lian, Q., Li, X., Zhang, W., Wang, K. and Jin, Z., 2012. Fabrication of a bio-inspired beta-Tricalcium phosphate/collagen scaffold based on ceramic stereolithography and gel casting for osteochondral tissue engineering. *Rapid Prototyping Journal*, 18(1), pp.68-80.
- [15] Bitterlich, B., Lutz, C. and Roosen, A., 2002. Rheological characterization of water-based slurries for the tape casting process. *Ceramics international*, 28(6), pp.675-683.
- [16] Boumchedda, K., Hamadi, M. and Fantozzi, G., 2007. Properties of a hydrophone produced with porous PZT ceramic, *Journal of the European Ceramic Society*, 27(13), pp.4169–4171.
- [17] Bourell, D.L., Leu, M.C. and Rosen, D.W., 2009. Roadmap for additive manufacturing: identifying the future of freeform processing. *The University of Texas at Austin*, Austin, TX.
- [18] Brady, G.A. and Halloran, J.W., 1997. Stereolithography of ceramic suspensions. *Rapid Prototyping Journal*, 3(2), pp.61-65.
- [19] Cai, Y. and Jessop, J.L., 2004. Photopolymerization, Free Radical. *Encyclopedia Of Polymer Science and Technology*, 10, pp.807-837.
- [20] Cesarano III, J., King, B.H. and Denham, H.B., 1998. Recent developments in robocasting of ceramics

- and multimaterial deposition (No. SAND--98-2195C; CONF-980826--). *Sandia National Labs.*, Albuquerque, NM (United States).
- [21] Cha, S.N., Kim,S.M., Kim,H.J., Ku, J.Y., Sohn,J.I., Park,Y.J., Song,B.G., Jung,M.H., Lee,E.K., Choi,B.L., Park,J.J., Wang,Z.L., Kim,J.M. and Kim,K., 2011. Porous PVDF As Effective Sonic Wave Driven Nano-generators, *Nano Letter*, 11(12), pp. 5142–5147.
- [22] Chabok, H., Zhou, C., Chen, Y., Eskandarinzhad, A., Zhou, Q., Shung, K., 2012. Ultrasound transducer array fabrication based on additive manufacturing of piezocomposites. In: *Proceedings of the ASME 2012 international symposium on flexible automation*, pp.433-444.
- [23] Chartier, T., Hinczewski, C. and Corbel, S., 1999. UV curable systems for tape casting. *Journal of the European Ceramic Society*, 19(1), pp.67-74.
- [24] Chartier, T., Penarroya, R., Pagnoux, C. and Baumard, J.F., 1997. Tape casting using UV curable binders. *Journal of the European ceramic society*,17(6), pp.765-771.
- [25] Chen, Z.P., Xu,C., Ma,C.Q., Ren,W.C. and Chen,H.M., 2013a. Lightweight and Flexible Graphene Foam Composites for high-performance electromagnetic interference shielding, *Advanced Material*, 25(9), pp.1296–1300.
- [26] Chen, S.L., He,G.H., Hu,H., Jin,S.Q., Zhou,Y., He,Y.Y., He,S.J., Zhao,F. and Hou,H.Q., 2013b. Elastic carbon foam via direct carbonization of polymer for flexible electrodes and organic chemical absorption, *Energy & Environmental Science*, 6(8), pp.2435-2439.
- [27] Chen, Y., Zhou, C. and Lao, J., 2011. A layerless additive manufacturing process based on CNC accumulation. *Rapid Prototyping Journal*, 17(3), pp.218-227.
- [28] Cheng, Y.L. and Lee, M.L., 2009. Development of dynamic masking rapid prototyping system for application in tissue engineering. *Rapid Prototyping Journal*, 15(1), pp.29-41.
- [29] Cheverton, M, Singh, P., Smith, L.S. and Chan, K.P., 2012. Ceramic polymer additive manufacturing system for ultrasound transducer. In: *Proceedings of Solid Freeform Fabrication Symposium*, pp. 863-875.
- [30] Choi, J.W., Ha, Y.M., Lee, S.H. and Choi, K.H., 2006. Design of microstereolithography system based

- on dynamic image projection for fabrication of three-dimensional microstructures. *Journal of mechanical science and technology*, 20(12), pp.2094-2104.
- [31] Choi, J.W., Wicker, R., Lee, S.H., Choi, K.H., Ha, C.S. and Chung, I., 2009. Fabrication of 3D biocompatible/biodegradable micro-scaffolds using dynamic mask projection microstereolithography. *Journal of Materials Processing Technology*, 209(15), pp.5494-5503.
- [32] Choi, S.J., Kwon, T.H., Im, H., Moon, D.I., Baek, D.J., Seol, M.L., Duarte, J.P. and Choi, Y.K., 2011. A Polydimethylsiloxane (PDMS) Sponge for the Selective Absorption of Oil from Water, *ACS Appl. Mater. Interfaces*, 3(12), pp. 4552–4556.
- [33] Chou, Y.T., Ko, Y.T. and Yan, M.F., 1987. Fluid flow model for ceramic tape casting. *Journal of the American Ceramic Society*, 70(10).
- [34] Christ, S., Schnabel, M., Vorndran, E., Groll, J. and Gbureck, U., 2015. Fiber reinforcement during 3D printing. *Materials Letters*, 139, pp.165-168.
- [35] Chu, G.T., Brady, G.A., Miao, W. and Halloran, J.W., 1998. Ceramic SFF by direct and indirect stereolithography. In *MRS Proceedings* (Vol. 542, p. 119). Cambridge University Press.
- [36] Cochran, S., Abrar, A., Kirk, K.J., Zhang, D., Button, T.W., Su, B. and Meggs, C., 2004, August. Net-shape ceramic processing as a route to ultrafine scale 1-3 connectivity piezoelectric ceramic-polymer composite transducers. In *Ultrasonics Symposium, 2004 IEEE* (Vol. 3, pp. 1682-1685). IEEE.
- [37] Compton, B.G. and Lewis, J.A., 2014. 3D - printing of lightweight cellular composites. *Advanced Materials*, 26(34), pp.5930-5935.
- [38] Cooke, M.N., Fisher, J.P., Dean, D., Rimnac, C. and Mikos, A.G., 2003. Use of Stereolithography to Manufacture Critical-Sized 3D Biodegradable Scaffolds for Bone Ingrowth. *Journal of Biomedical Materials Research*. 64(2), pp. 65-69.
- [39] Dai, K., Ji, X., Xiang, Z.D., Zhang, W.Q., Tang, J.H. and Li, Z.M., 2012. Electrical Properties of an Ultralight Conductive carbon nanotube polymer composite foam. *Polymer-Plastics Technology and Engineering*, 51(3), pp.304–306.

- [40] Dang, Z.M., Yuan, J.K., Yao, S.H. and Liao, R.J., 2013. Flexible nanodielectric materials with high permittivity for power energy storage. *Advanced Materials*, 25(44), pp.6334-6365.
- [41] Daniel, I.M. and Cho, J.M., 2011. Characterization of Anisotropic Polymeric Foam under Static and Dynamic Loading. *Experimental Mechanics*, 51(8), pp.1395-1403.
- [42] de Hazan, Y., Thänert, M., Trunec, M. and Misak, J., 2012. Robotic deposition of 3d nanocomposite and ceramic fiber architectures via UV curable colloidal inks. *Journal of the European Ceramic Society*, 32(6), pp.1187-1198.
- [43] Deckers, J., Shahzad, K., Vleugels, J. and Kruth, J.P., 2012. Isostatic pressing assisted indirect selective laser sintering of alumina components. *Rapid Prototyping Journal*, 18(5), pp.409-419.
- [44] Deng, D., Chen, Y. and Zhou, C., 2012. Investigation on PEEK Fabrication Using Mask-image-projection-based Stereolithography. *Solid Freeform Fabrication Symposium*. Austin, Texas, pp. 606-616.
- [45] Dey, A., Kayal, N. and Chakrabarti, O., 2011. Preparation of porous SiC ceramics by an infiltration technique. *Ceramics International*, 37(1), pp.223-230.
- [46] Diamond & Related Materials Laboratory, n.d. Available at: <http://drm.kist.re.kr/cerapedia/process/images/jgl00303.gif> [Accessed May.17.2016]
- [47] Dufaud, O. and Corbel, S., 2002. Stereolithography of PZT ceramic suspensions. *Rapid Prototyping Journal*, 8(2), pp.83-90.
- [48] Dufaud, O., Gall, H.L. and Corbel, S., 2003. Stereolithography of lead zirconate titanate ceramics for MEMS applications. In: *Microtechnologies for the New Millennium 2003* (pp. 28-37). International Society for Optics and Photonics.
- [49] Ebert, J., Özkol, E., Zeichner, A., Uibel, K., Weiss, Ö., Koops, U., Telle, R. and Fischer, H., 2009. Direct inkjet printing of dental prostheses made of zirconia. *Journal of dental research*, 88(7), pp.673-676.
- [50] Eckel, Z.C., Zhou, C., Martin, J.H., Jacobsen, A.J., Carter, W.B. and Schaedler, T.A., 2016. Additive manufacturing of polymer-derived ceramics. *Science*, 351(6268), pp.58-62.

- [51] Elliott, A.M., Ivanova, O.S., Williams, C.B. and Campbell, T.A., 2013. Inkjet printing of quantum dots in photopolymer for use in additive manufacturing of nanocomposites. *Advanced Engineering Materials*, 15(10), pp.903-907.
- [52] Envisiontec SI500, 2012. Available from: <http://envisiontec.com/envisiontec/wp-content/uploads/MSDS-SI500.pdf>
- [53] Evans, R.S., Bourell, D.L., Beaman, J.J. and Campbell, M.I., 2005. Rapid manufacturing of silicon carbide composites. *Rapid Prototyping Journal*, 11(1), pp.37-40.
- [54] Farlow, R., Galbraith, W., Knowles, M. and Hayward, G., 2001. Micromachining of a piezocomposite transducer using a copper vapor laser. *Ultrasonics, Ferroelectrics, and Frequency Control, IEEE Transactions on*, 48(3), pp.639-640.
- [55] Farsari, M., Huang, S., Birch, P., Claret-Tournier, F., Young, R., Budgett, D., Bradfield, C. and Chatwin, C., 1999. Microfabrication by use of a spatial light modulator in the ultraviolet: experimental results. *Optics Letters*, 24(8), pp.549-550.
- [56] Feygin, M. and Pak, S.S., Helisys, Inc., 1999. Laminated object manufacturing apparatus and method. U.S. Patent 5,876,550.
- [57] Friedrich, K., Fakirov, S. and Zhang, Z. eds., 2005. *Polymer composites: from nano-to macro-scale*. Springer Science & Business Media.
- [58] Fukasawa, T., Ando, M., Ohji, T. and Kanzaki, S., 2001. Synthesis of Porous Ceramics with Complex Pore Structure by freeze-dry processing, *Journal of the American Ceramic Society*, 84(1), pp.230-232.
- [59] Gauvin, R., Chen, Y.C., Lee, J.W., Soman, P., Zorlutuna, P., Nichol, J.W., Bae, H., Chen, S. and Khademhosseini, A., 2012. Microfabrication of complex porous tissue engineering scaffolds using 3D projection stereolithography. *Biomaterials*, 33(15), pp.3824-3834.
- [60] Gay, D., 2014. *Composite materials: design and applications*. CRC press.
- [61] Gentilman, R.L., Fiore, D.F., Pham, H.T., French, K.W. and Bowen, L.J., 1994. Fabrication and properties of 1-3 PZT-polymer composites (No. CONF-931142--). American Ceramic Society,

Westerville, OH (United States).

- [62] Gentry, S.P. and Halloran, J.W., 2013. Depth and width of cured lines in photopolymerizable ceramic suspensions. *Journal of the European Ceramic Society*, 33(10), pp.1981-1988.
- [63] Gladman, A.S., Matsumoto, E.A., Nuzzo, R.G., Mahadevan, L. and Lewis, J.A., 2016. Biomimetic 4D printing. *Nature materials*.
- [64] Gomes, C.M., Rambo, C.R., De Oliveira, A.P.N., Hotza, D., Gouve[^]a, D., Travitzky, N. and Greil, P., 2009. Colloidal processing of glass–ceramics for laminated object manufacturing. *Journal of the American Ceramic Society*, 92(6), pp.1186-1191.
- [65] Griffith, M.L. and Halloran, J.W., 1996. Freeform fabrication of ceramics via stereolithography. *Journal of the American Ceramic Society*, 79(10), pp.2601-2608.
- [66] Griffith, M.L. and Halloran, J.W., 1997. Scattering of ultraviolet radiation in turbid suspensions. *Journal of applied physics*, 81(6), pp.2538-2546.
- [67] Guo, D., Li, L.T., Cai, K., Gui, Z.L. and Nan, C.W., 2004. Rapid prototyping of piezoelectric ceramics via selective laser sintering and gelcasting. *Journal of the American Ceramic Society*, 87(1), pp.17-22.
- [68] Gurauskis, J., Baudín, C. and Sánchez-Herencia, A.J., 2007. Tape casting of Y-TZP with low binder content. *Ceramics international*, 33(6), pp.1099-1103.
- [69] Haikutech, n.d. Available at: http://www.haikutech.com/App_Themes/Default/7A_steel-belt-tape-caster_S.jpg [Accessed May.17.2016]
- [70] Hatzenbichler, M., Geppert, M., Gruber, S., Ipp, E., Almedal, R. and Stampfl, J., 2012, February. DLP-based light engines for additive manufacturing of ceramic parts. In *SPIE MOEMS-MEMS* (pp. 82540E-82540E). International Society for Optics and Photonics.
- [71] Hinczewski, C., Corbel, S. and Chartier, T., 1998a. Ceramic suspensions suitable for stereolithography. *Journal of the European Ceramic Society*, 18(6), pp.583-590.
- [72] Hinczewski, C., Corbel, S. and Chartier, T., 1998b. Stereolithography for the fabrication of ceramic three-dimensional parts. *Rapid Prototyping Journal*, 4(3), pp.104-111.
- [73] Hirata, Y., Nakaishi, H., Numazawa, T. and Takada, H., 1997, October. Piezocomposite of fine PZT

- rods realized with synchrotron radiation lithography. In Ultrasonics Symposium, 1997. *Proceedings, 1997 IEEE* (Vol. 2, pp. 877-881). IEEE.
- [74] Hollister, S.J., 2005. Porous scaffold design for tissue engineering. *Nature materials*, 4(7), pp.518-524.
- [75] Hou, Q.P., Grijpma, D.W. and Feijen, J., 2003. Porous polymeric structures for tissue engineering prepared by a coagulation, compression moulding and salt leaching technique. *Biomaterials*, 24(11), pp.1937-1947.
- [76] Huang, T., Mason, M.S., Zhao, X., Hilmas, G.E. and Leu, M.C., 2009a. Aqueous-based freeze-form extrusion fabrication of alumina components. *Rapid Prototyping Journal*, 15(2), pp.88-95.
- [77] Huang, X., Jiang, P. and Xie, L., 2009b. Ferroelectric polymer/silver nanocomposites with high dielectric constant and high thermal conductivity. *Applied Physics Letters*, 95(24), p.242901.
- [78] Hull, C.W., Uvp, Inc., 1986. Apparatus for production of three-dimensional objects by stereolithography. U.S. Patent 4,575,330.
- [79] Hung, T.C., Huang, J.S., Wang, Y.W. and Lin, K.Y., 2014. Inorganic polymeric foam as a sound absorbing and insulating material. *Construction and Building Materials*, 50, pp.328-334.
- [80] Hutmacher, D.W., 2000. Scaffolds in tissue engineering bone and cartilage. *Biomaterials*, 21(24), pp. 2529-2543.
- [81] Inzana, J.A., Olvera, D., Fuller, S.M., Kelly, J.P., Graeve, O.A., Schwarz, E.M., Kates, S.L. and Awad, H.A., 2014. 3D printing of composite calcium phosphate and collagen scaffolds for bone regeneration. *Biomaterials*, 35(13), pp.4026-4034.
- [82] Jacobs F.P., 1992. *Rapid prototyping and manufacturing: fundamental of stereolithography*. Dearborn: Society of Manufacturing Engineer.
- [83] Jafari, M., Han, W., Mohammadi, F., Safari, A., Danforth, S.C. and Langrana, N., 2000. A novel system for fused deposition of advanced multiple ceramics. *Rapid Prototyping Journal*, 6(3), pp.161-175.
- [84] Jang, J.H., Wang, S., Pilgrim, S.M. and Schulze, W.A., 2000. Preparation and characterization of

- barium titanate suspensions for stereolithography. *Journal of the American Ceramic Society*, 83(7), pp.1804-1806.
- [85] Joshi, S.C., Lam, Y.C., Boey, F.Y.C. and Tok, A.I.Y., 2002. Power law fluids and Bingham plastics flow models for ceramic tape casting. *Journal of Materials Processing Technology*, 120(1), pp.215-225.
- [86] Kara, H., Ramesh,R., Stevens,R. and Bowen,C.R., 2003. Porous PZT Ceramics for receiving transducers. *IEEE Transactions On Ultrasonics, Ferroelectrics, and Frequency Control*, 50(3), pp.289-296.
- [87] Karageorgious,V. and Kaplan ,D., 2005. Porosity of 3D Biomaterial Scaffolds and Osteogenesis. *Biomaterials*, 26(27), pp.5474-5491.
- [88] Karalekas, D. and Antoniou, K., 2004. Composite rapid prototyping: overcoming the drawback of poor mechanical properties. *Journal of materials processing technology*, 153, pp.526-530.
- [89] Kenzari, S., Bonina, D., Dubois, J.M. and Fournée, V., 2012. Quasicrystal–polymer composites for selective laser sintering technology. *Materials & Design*, 35, pp.691-695.
- [90] Kim, B. J., Park,T. G. and Kim, M. H. 1998. Temperature and frequency dependence of dielectric properties of (Ba, Sr, Mg) TiO₃ ceramic capacitors. *Journal of the Korean Physical Society*, 32: pp.289-291.
- [91] Klosterman, D., Chartoff, R., Agarwala, M., Fiscus, I., Murphy, J., Cullen, S. and Yeazell, M., 1999. Direct Fabrication of Polymer Composite Structures with Curved LOM. *Solid Freeform Fabrication Symposium*.
- [92] Kokkinis, D., Schaffner, M. and Studart, A.R., 2015. Multimaterial magnetically assisted 3D printing of composite materials. *Nature communications*, 6.
- [93] Krieger, I.M. and Dougherty, T.J., 1959. A mechanism for non - Newtonian flow in suspensions of rigid spheres. *Transactions of The Society of Rheology (1957-1977)*, 3(1), pp.137-152.
- [94] Kumar, A.V., Dutta, A. and Fay, J.E., 2004. Electrophotographic printing of part and binder

- powders. *Rapid Prototyping Journal*, 10(1), pp.7-13.
- [95] Kumar, S., Hofmann, M., Steinmann, B., Foster, E.J. and Weder, C., 2012. Reinforcement of stereolithographic resins for rapid prototyping with cellulose nanocrystals. *ACS applied materials & interfaces*, 4(10), pp.5399-5407.
- [96] Le Ferrand, H., Bouville, F., Niebel, T.P. and Studart, A.R., 2015. Magnetically assisted slip casting of bioinspired heterogeneous composites. *Nature materials*, 14(11), pp.1172-1179.
- [97] Lebel, L.L., Aissa, B., Khakani, M.A.E. and Therriault, D., 2010. Ultraviolet - Assisted Direct-Write Fabrication of Carbon Nanotube/Polymer Nanocomposite Microcoils. *Advanced Materials*, 22(5), pp.592-596.
- [98] Lee, D., Lee, J., Kim, J.B., Kim, J., Na, H.B., Kim, B., Shin, C.H., Kwak, J.H., Dohnalkova, A., Grate, J.W., Hyeon, T. and Kim, H.S., 2005. Simple Fabrication of a Highly Sensitive and Fast Glucose Biosensor. *Advanced Materials*, 17(23), pp.2828-2833.
- [99] Lee, J.H. 2002, Design and synthesis of biocompatible ceramic/polymer composites via stereolithography, ProQuest Dissertations Publishing.
- [100] Lee, J.S., Hong, J.M., Jung, J.W., Shim, J.H., Oh, J.H. and Cho, D.W., 2014. 3D printing of composite tissue with complex shape applied to ear regeneration. *Biofabrication*, 6(2), p.024103.
- [101] Leigh, S.J., Bradley, R.J., Purssell, C.P., Billson, D.R. and Hutchins, D.A., 2012. A simple, low-cost conductive composite material for 3D printing of electronic sensors. *PloS one*, 7(11), p.e49365.
- [102] Lewis, J.A., 2000. Colloidal processing of ceramics. *Journal of the American Ceramic Society*, 83(10), pp.2341-2359.
- [103] Lewis, J.A., 2006a. Direct ink writing of 3D functional materials. *Advanced Functional Materials*, 16(17), pp.2193-2204.
- [104] Lewis, J.A., Blackman, K.A., Ogden, A.L., Payne, J.A. and Francis, L.F., 1996. Rheological property and stress development during drying of tape - cast ceramic layers. *Journal of the American Ceramic Society*, 79(12), pp.3225-3234.

- [105] Lewis, J.A., Smay, J.E., Stuecker, J. and Cesarano, J., 2006b. Direct ink writing of three - dimensional ceramic structures. *Journal of the American Ceramic Society*, 89(12), pp.3599-3609.
- [106] Liao, C.J., Chen, C.F., Chen, J.H., Chiang, S.F., Lin, Y.J. and Chang, K.Y., 2002. Fabrication of porous biodegradable polymer scaffolds using a solvent merging/particulate leaching method, *Journal of biomedical materials research*, 59(4), pp.676-681.
- [107] Lin, C.T., Liao, L.D., Liu, Y.H., Wang, I.J., Lin, B.S. and Chang, J.Y., 2011. Novel Dry Polymer Foam Electrodes for Long-Term EEG measurement, *IEEE Transaction On Biomedical Engineering*, 58(5), pp. 1200-1207.
- [108] Lin, Q.L., Luo, B., Qu, L., Fang, C.Q. and Chen, Z.M., 2013. Direct preparation of carbon foam by pyrolysis of cyanate ester resin at ambient pressure. *Journal of analytical and applied pyrolysis*, 104, pp.714-717.
- [109] Lipke, D.W., Zhang, Y., Liu, Y., Church, B.C. and Sandhage, K.H., 2010. Near net-shape/net-dimension ZrC/W-based composites with complex geometries via rapid prototyping and displacive compensation of porosity. *Journal of the European Ceramic Society*, 30(11), pp.2265-2277.
- [110] Liu, H. and Mo, J., 2010. Study on Nanosilica Reinforced Stereolithography Resin. *Journal of Reinforced Plastics and Composites*, 29(6), pp.909-920.
- [111] Liu, R., Harasiewicz, K.A. and Foster, F.S., 2001. Interdigital pair bonding for high frequency (20-50 MHz) ultrasonic composite transducers. *Ultrasonics, Ferroelectrics, and Frequency Control, IEEE Transactions on*, 48(1), pp.299-306.
- [112] Lous, G.M., Cornejo, I.A., McNulty, T.F., Safari, A. and Danforth, S.C., 2000. Fabrication of piezoelectric ceramic/polymer composite transducers using fused deposition of ceramics. *Journal of the American Ceramic Society*, 83(1), pp.124-28.
- [113] Love, L.J., Kunc, V., Rios, O., Duty, C.E., Elliott, A.M., Post, B.K., Smith, R.J. and Blue, C.A., 2014. The importance of carbon fiber to polymer additive manufacturing. *Journal of Materials Research*, 29(17), pp.1893-1898.

- [114] Lu, J., Moon, K.S., and Wong, C.P., 2008. Silver/polymer nanocomposite as a high-k polymer matrix for dielectric composites with improved dielectric performance. *Journal of Materials Chemistry*, 18, pp. 4821–4826
- [115] Lu, X., Wang, G., Zhai, T., Yu, M., Xie, S., Ling, Y., Liang, C., Tong, Y. and Li, Y., 2012. Stabilized TiN nanowire arrays for high-performance and flexible supercapacitors. *Nano letters*, 12(10), pp.5376-5381.
- [116] Lu, Y., Mapili, G., Suhali, G., Chen, S. and Roy, K., 2006. A digital micro - mirror device - based system for the microfabrication of complex, spatially patterned tissue engineering scaffolds. *Journal of Biomedical Materials Research Part A*, 77(2), pp.396-405.
- [117] Lukacs, M., Sayer, M., Lockwood, G. and Foster, S., 1999. Laser micromachined high frequency ultrasonic arrays. In Ultrasonics Symposium, 1999. *Proceedings. 1999 IEEE* (Vol. 2, pp. 1209-1212). IEEE.
- [118] Marselli, S., Pavia, V., Galassi, C., Rocari, E., Craciun, F., and Guidarelli, G., 1999. Porous piezoelectric ceramic hydrophone, *J. Acoust. Soc. Am.* 106 (2), pp.733-738.
- [119] Matsuzaki, R., Ueda, M., Namiki, M., Jeong, T.K., Asahara, H., Horiguchi, K., Nakamura, T., Todoroki, A. and Hirano, Y., 2016. Three-dimensional printing of continuous-fiber composites by in-nozzle impregnation. *Scientific reports*, 6.
- [120] McCall, W.R., Kim, K., Heath, C., Pierre, G.L. and Sirbuly, D.J., 2014. Piezoelectric Nanoparticle–Polymer Composite Foams. *ACS Appl. Mater. Interfaces*, 6(22), pp.19504-19509.
- [121] McNulty, T.F., Mohammadi, F., Bandyopadhyay, A., Shanefield, D.J., Danforth, S.C. and Safari, A., 1998. Development of a binder formulation for fused deposition of ceramics. *Rapid Prototyping Journal*, 4(4), pp.144-150.
- [122] Melchels, F.P., Feijen, J. and Grijpma, D.W., 2009. A poly (D, L-lactide) resin for the preparation of tissue engineering scaffolds by stereolithography. *Biomaterials*, 30(23), pp.3801-3809.
- [123] Melcher, R., Martins, S., Travitzky, N. and Greil, P., 2006. Fabrication of Al₂O₃-based composites

- by indirect 3D-printing. *Materials Letters*, 60(4), pp.572-575.
- [124] Mikeska, K.R. and Cannon, W.R., 1988. Non-aqueous dispersion properties of pure barium titanate for tape casting. *Colloids and Surfaces*, 29(3), pp.305-321.
- [125] Mikolajek, M., Friederich, A., Kohler, C., Rosen, M., Rathjen, A., Krüger, K. and Binder, J.R., 2015. Direct inkjet printing of dielectric ceramic/polymer composite thick films. *Advanced Engineering Materials*, 17(9), pp.1294-1301.
- [126] Mikos, A.G., Thorson, A.J., Czerwonka, L.A., Bao, Y., Langer, R., Winslow, D.N. and Vincati, J.P., 1994. Preparation and characterization of poly(l-lactic acid) foams. *Polymer*, 35(5), pp.1068-1077.
- [127] Mistler, R.E. and Twiname, E.R., 2000. *Tape Casting: Theory and Practice*, John Wiley & Sons, New York.
- [128] Monneret, S., Loubere, V. and Corbel, S., 1999, March. Microstereolithography using a dynamic mask generator and a noncoherent visible light source. In *Design, Test, and Microfabrication of MEMS/MOEMS* (pp. 553-561). International Society for Optics and Photonics.
- [129] Morissette, S.L., Lewis, J.A., Cesarano, J., Dimos, D.B. and Baer, T., 2000. Solid freeform fabrication of aqueous alumina–poly (vinyl alcohol) gelcasting suspensions. *Journal of the American Ceramic Society*, 83(10), pp.2409-2416.
- [130] Mott, M. and Evans, J.R., 2001. Solid freeforming of silicon carbide by inkjet printing using a polymeric precursor. *Journal of the American Ceramic Society*, 84(2), pp.307-13.
- [131] Mühler, T., Gomes, C.M., Heinrich, J. and Günster, J., 2015. Slurry - Based Additive Manufacturing of Ceramics. *International Journal of Applied Ceramic Technology*, 12(1), pp.18-25.
- [132] Ning, F., Cong, W., Qiu, J., Wei, J. and Wang, S., 2015. Additive manufacturing of carbon fiber reinforced thermoplastic composites using fused deposition modeling. *Composites Part B: Engineering*, 80, pp.369-378.
- [133] Olhero, S.M. and Ferreira, J.M.F., 2005. Rheological characterisation of water-based AlN slurries for the tape casting process. *Journal of materials processing technology*, 169(2), pp.206-213.

- [134] Paik, U., Hackley, V.A., Choi, S.C. and Jung, Y.G., 1998. The effect of electrostatic repulsive forces on the stability of BaTiO₃ particles suspended in non-aqueous media. *Colloids and Surfaces A: Physicochemical and Engineering Aspects*, 135(1), pp.77-88.
- [135] Pan, Y., Zhao, X., Zhou, C. and Chen, Y., 2012a. Smooth surface fabrication in mask projection based stereolithography. *Journal of Manufacturing Processes*, 14(4), pp.460-470.
- [136] Pan, Y., Zhou, C. and Chen, Y., 2012b. A fast mask projection stereolithography process for fabricating digital models in minutes. *Journal of Manufacturing Science and Engineering*, 134(5), p.051011.
- [137] Panda, M., Srinivas, V. and Thakur, A.K., 2008. Surface and interfacial effect of filler particle on electrical properties of polyvinylidene fluoride/nickel composites. *Applied Physics Letters*, 93(24), p.242908.
- [138] Pardo, L. and Ricote, J. eds., 2011. *Multifunctional polycrystalline ferroelectric materials: processing and properties* (Vol. 140). Springer Science & Business Media.
- [139] Park, I.B., Ha, Y.M. and Lee, S.H., 2011. Dithering method for improving the surface quality of a microstructure in projection microstereolithography. *The International Journal of Advanced Manufacturing Technology*, 52(5-8), pp.545-553.
- [140] Pascall, A.J., Qian, F., Wang, G., Worsley, M.A., Li, Y. and Kuntz, J.D., 2014. Light - Directed Electrophoretic Deposition: A New Additive Manufacturing Technique for Arbitrarily Patterned 3D Composites. *Advanced Materials*, 26(14), pp.2252-2256.
- [141] Patrick, J.F., Sottos, N.R. and White, S.R., 2012. Microvascular based self-healing polymeric foam. *Polymer*, 53(19), pp.4231-4240.
- [142] Postiglione, G., Natale, G., Griffini, G., Levi, M. and Turri, S., 2015. Conductive 3D microstructures by direct 3D printing of polymer/carbon nanotube nanocomposites via liquid deposition modeling. *Composites Part A: Applied Science and Manufacturing*, 76, pp.110-114.
- [143] Rahimabady, M., Yao, K., Arabnejad, S., Lu, L., Shim, V.P. and Chet, D.C.W., 2012. Intermolecular

- interactions and high dielectric energy storage density in poly (vinylidene fluoride-hexafluoropropylene)/poly (vinylidene fluoride) blend thin films. *Applied Physics Letters*, 100(25), p.252907.
- [144] Ramajo, L.A., Reboredo, M.M. and Castro, M.S., 2007. Characterisation of epoxy/BaTiO₃ composites processed by dipping for integral capacitor films (ICF). *Journal of Materials Science*, 42(10), pp.3685-3691.
- [145] Ramay, H.R. and Zhang, M., 2003. Preparation of porous hydroxyapatite scaffolds by combination of the gel-casting and polymer sponge methods. *Biomaterials*, 24(19), pp.3293-3302.
- [146] Richerson, D., Richerson, D.W. and Lee, W.E., 2005. *Modern ceramic engineering: properties, processing, and use in design*. CRC press.
- [147] Rodriguez, J.N., Yu, Y.J., Miller, M.W., Wilson, T.S., Hartman, J., Clubb, F.J., Gentry, B. and Maitland, D.J., 2012. Opacification of shape memory polymer foam designed for treatment of intracranial aneurysms. *Annals of biomedical engineering*, 40(4), pp.883-897.
- [148] Safari, A. and Janas, V.F., 1997. Processing of fine-scale piezoelectric ceramic/polymer composites for transducer applications. *Ferroelectrics*, 196(1), pp.187-190.
- [149] Safari, A., Allahverdi, M. and Akdogan, E.K., 2006. Solid freeform fabrication of piezoelectric sensors and actuators. *Journal of materials science*, 41(1), pp.177-198.
- [150] Scheithauer, U., Bergner, A., Schwarzer, E., Richter, H.J. and Moritz, T., 2014. Studies on thermoplastic 3D printing of steel–zirconia composites. *Journal of Materials Research*, 29(17), pp.1931-1940.
- [151] Scheithauer, U., Schwarzer, E., Richter, H.J. and Moritz, T., 2015. Thermoplastic 3D Printing—An Additive Manufacturing Method for Producing Dense Ceramics. *International Journal of Applied Ceramic Technology*, 12(1), pp.26-31.
- [152] Schwentenwein, M. and Homa, J., 2015. Additive Manufacturing of Dense Alumina Ceramics. *International Journal of Applied Ceramic Technology*, 12(1), pp.1-7.
- [153] Serra, T., Planell, J.A. and Navarro, M., 2013. High-resolution PLA-based composite scaffolds via 3-

- D printing technology. *Acta biomaterialia*, 9(3), pp.5521-5530.
- [154] Shahzad, K., Deckers, J., Kruth, J.P. and Vleugels, J., 2013. Additive manufacturing of alumina parts by indirect selective laser sintering and post processing. *Journal of Materials Processing Technology*, 213(9), pp.1484-1494.
- [155] Shahzad, K., Deckers, J., Zhang, Z., Kruth, J.P. and Vleugels, J., 2014. Additive manufacturing of zirconia parts by indirect selective laser sintering. *Journal of the European Ceramic Society*, 34(1), pp.81-89.
- [156] Shastri, V.P., Martin, I. and Langer, R., 2000. Macroporous polymer foams by hydrocarbon templating. *PNAS*, 29(5), pp.1970-1975.
- [157] Shofner, M.L., Lozano, K., Rodríguez - Macías, F.J. and Barrera, E.V., 2003. Nanofiber - reinforced polymers prepared by fused deposition modeling. *Journal of applied polymer science*, 89(11), pp.3081-3090.
- [158] Shung, K.K., 2015. *Diagnostic ultrasound: Imaging and blood flow measurements*. CRC press.
- [159] Smith, W.A. and Auld, B.A., 1991. Modeling 1-3 composite piezoelectrics: thickness-mode oscillations. *Ultrasonics, Ferroelectrics, and Frequency Control, IEEE Transactions on*, 38(1), pp.40-47.
- [160] Smith, W.A., 1986, June. Composite piezoelectric materials for medical ultrasonic imaging transducers-a review. In *Applications of Ferroelectrics. 1986 Sixth IEEE International Symposium on* (pp. 249-256). IEEE.
- [161] Song, X. and Chen, Y., 2012. Joint Design for 3-D Printing Non-Assembly Mechanisms. *ASME 2012 International Design Engineering Technical Conferences and Computers and Information in Engineering Conference*. pp. 619-631.
- [162] Song, X., Chen, Y., Lee, T.W., Wu, S. and Cheng, L., 2015. Ceramic fabrication using Mask-Image-Projection-based Stereolithography integrated with tape-casting. *Journal of Manufacturing Processes*, 20, pp.456-464.

- [163] Song, X., Chen, Z., Lei, L., Shung, K., Zhou, Q., Chen, Y., 2017. Piezoelectric Component Fabrication Using Projection-based Stereolithography of Barium Titanate Ceramic Suspensions. *Rapid Prototyping Journal*. 23(1). In press.
- [164] Song, Y., Liu, X. and Chen, J. 2004. The maximum solid loading and viscosity estimation of ultra-fine BaTiO₃ aqueous suspensions. *Colloids and Surfaces A: Physicochemical and Engineering Aspects*, 247(1-3), pp.27-34.
- [165] Standard F2792-12a, 2009. Available from:
http://www.astm.org/FULL_TEXT/F2792/HTML/F2792.htm
- [166] Subramanian, K., Vail, N., Barlow, J. and Marcus, H., 1995. Selective laser sintering of alumina with polymer binders. *Rapid Prototyping Journal*, 1(2), pp.24-35.
- [167] Sun, C. and Zhang, X., 2002. The influences of the material properties on ceramic micro-stereolithography. *Sensors and Actuators A: Physical*, 101(3), pp.364-370.
- [168] Sun, C., Fang, N., Wu, D.M. and Zhang, X., 2005. Projection micro-stereolithography using digital micro-mirror dynamic mask. *Sensors and Actuators A: Physical*, 121(1), pp.113-120.
- [169] Suwanprateeb, J., Sanngam, R., Suvannapruk, W. and Panyathanmaporn, T., 2009. Mechanical and in vitro performance of apatite–wollastonite glass ceramic reinforced hydroxyapatite composite fabricated by 3D-printing. *Journal of Materials Science: Materials in Medicine*, 20(6), pp.1281-1289.
- [170] Taboas, J.M., Maddox, R.D., Krebsbach, P.H. and Hollister, S.J., 2003. Indirect solid free form fabrication of local and global porous, biomimetic and composite 3D polymer-ceramic scaffolds. *Biomaterials*, 24(1), pp.181-194.
- [171] Tang, H.H. and Liu, F.H., 2005. Ceramic laser gelling. *Journal of the European Ceramic Society*, 25(5), pp.627-632.
- [172] Tang, H.H. and Yen, H.C., 2015. Slurry-based additive manufacturing of ceramic parts by selective laser burn-out. *Journal of the European Ceramic Society*, 35(3), pp.981-987.
- [173] Tekinalp, H.L., Kunc, V., Velez-Garcia, G.M., Duty, C.E., Love, L.J., Naskar, A.K., Blue, C.A. and Ozcan, S., 2014. Highly oriented carbon fiber–polymer composites via additive

- manufacturing. *Composites Science and Technology*, 105, pp.144-150.
- [174] Tesavibul, P., Felzmann, R., Gruber, S., Liska, R., Thompson, I., Boccaccini, A.R. and Stampfl, J., 2012. Processing of 45S5 Bioglass® by lithography-based additive manufacturing. *Materials Letters*, 74, pp.81-84.
- [175] Thomenius, K., R. A. Fisher, D. M. Mills, R. G. Wodnicki, C. R. Hazard, L. S. Smith, 2005. Mosaic Arrays Using Micromachined Ultrasound Transducers, US Patent No.: 6,865,140.
- [176] Tian, X., Li, D. and Heinrich, J.G., 2012. Rapid prototyping of porcelain products by layer-wise slurry deposition (LSD) and direct laser sintering. *Rapid Prototyping Journal*, 18(5), pp.362-373.
- [177] Tok, A.I., Boey, F.Y. and Lam, Y.C., 2000. Non-Newtonian fluid flow model for ceramic tape casting. *Materials Science and Engineering: A*, 280(2), pp.282-288.
- [178] Tomeckova, V. and Halloran, J.W., 2010a. Predictive models for the photopolymerization of ceramic suspensions. *Journal of the European Ceramic Society*, 30(14), pp.2833-2840.
- [179] Tomeckova, V. and Halloran, J.W., 2010b. Cure depth for photopolymerization of ceramic suspensions. *Journal of the European Ceramic Society*, 30(15), pp.3023-3033.
- [180] Torabi, P., Petros, M. and Khoshnevis, B., 2014. Selective inhibition sintering: the process for consumer metal additive manufacturing. *3D Printing and Additive Manufacturing*, 1(3), pp.152-155.
- [181] Travitzky, N., Bonet, A., Dermeik, B., Fey, T., Filbert - Demut, I., Schlier, L., Schlordt, T. and Greil, P., 2014. Additive Manufacturing of Ceramic - Based Materials. *Advanced Engineering Materials*, 16(6), pp.729-754.
- [182] Tumbleston, J.R., Shirvanyants, D., Ermoshkin, N., Januszewicz, R., Johnson, A.R., Kelly, D., Chen, K., Pinschmidt, R., Rolland, J.P., Ermoshkin, A. and Samulski, E.T., 2015. Continuous liquid interface production of 3D objects. *Science*, 347(6228), pp.1349-1352.
- [183] Ventura, S., Narang, S., Guerit, P., Liu, S., Twait, D., Khandelwal, P., Cohen, E. and Fish, R., 2000. Freeform Fabrication of Functional Silicon Nitride Components by Direct Photo Shaping. In: *MRS Proceedings*, 625(81).

- [184] Waetjen, A.M., Polsakiewicz, D.A., Kuhl, I., Telle, R. and Fischer, H., 2009. Slurry deposition by airbrush for selective laser sintering of ceramic components. *Journal of the European Ceramic Society*, 29(1), pp.1-6.
- [185] Wang, G., Lu, X., Ling, Y., Zhai, T., Wang, H., Tong, Y. and Li, Y., 2012. LiCl/PVA gel electrolyte stabilizes vanadium oxide nanowire electrodes for pseudocapacitors. *ACS nano*, 6(11), pp.10296-10302.
- [186] Wang, J. and Shaw, L.L., 2005. Rheological and extrusion behavior of dental porcelain slurries for rapid prototyping applications. *Materials Science and Engineering: A*, 397(1), pp.314-321.
- [187] Wiki PZT. Available at: https://en.wikipedia.org/wiki/Lead_zirconate_titanate#cite_note-1 [Accessed May.23.2016]
- [188] Wilkes, J., Hagedorn, Y.C., Meiners, W. and Wissenbach, K., 2013. Additive manufacturing of ZrO₂-Al₂O₃ ceramic components by selective laser melting. *Rapid Prototyping Journal*, 19(1), pp.51-57.
- [189] Yang, Y., Chen, Z., Song, X., Zhu, B., Hsiai, T., Wu, P.I., Xiong, R., Shi, J., Chen, Y., Zhou, Q. and Shung, K.K., 2016. Three dimensional printing of high dielectric capacitor using projection based stereolithography method. *Nano Energy*, 22, pp.414-421.
- [190] Yang, Y.L., Goopta, M.C., Dudley, K.L. and Lawrence, R.W., 2005. Conductive carbon nanofiber-polymer foam structures. *Advanced Material*, 17(16), pp.1999-2003.
- [191] Yen, H.C., 2015. Experimental studying on development of slurry-layer casting system for additive manufacturing of ceramics. *The International Journal of Advanced Manufacturing Technology*, 77(5-8), pp.915-925.
- [192] Yin, X., Travitzky, N. and Greil, P., 2007. Three - Dimensional Printing of Nanolaminated Ti₃AlC₂ Toughened TiAl₃-Al₂O₃ Composites. *Journal of the American Ceramic Society*, 90(7), pp.2128-2134.
- [193] Zak, G., Chan, A.Y.F., Park, C.B. and Benhabib, B., 1996. Viscosity analysis of photopolymer and glass-fibre composites for rapid layered manufacturing. *Rapid Prototyping Journal*, 2(3), pp.16-23.

- [194] Zanchetta, E., Cattaldo, M., Franchin, G., Schwentenwein, M., Homa, J., Brusatin, G. and Colombo, P., 2016. Stereolithography of SiOC Ceramic Microcomponents. *Advanced Materials*, 28(2), pp.370-376.
- [195] Zhang, A.J., Chen, M.J., Du, C., Guo, H.Z., Bai, H. and Li, L., 2013. Poly(dimethylsiloxane) Oil Absorbent with a Three-Dimensionally Interconnected Porous Structure and Swellable Skeleton. *ACS Appl. Mater. Interfaces*, 5(20), pp. 10201–10206.
- [196] Zhou, C., Chen, Y. and Waltz, R.A., 2009. Optimized mask image projection for solid freeform fabrication. *Journal of Manufacturing Science and Engineering*, 131(6), p.061004.
- [197] Zhou, C., Chen, Y., Yang, Z. and Khoshnevis, B., 2013. Digital material fabrication using mask-image-projection-based stereolithography. *Rapid Prototyping Journal*, 19(3), pp.153-165.
- [198] Zhou, W., Li, D. and Wang, H., 2010. A novel aqueous ceramic suspension for ceramic stereolithography. *Rapid Prototyping Journal*, 16(1), pp.29-35.
- [199] Zocca, A., Colombo, P., Gomes, C.M. and Günster, J., 2015. Additive Manufacturing of Ceramics: Issues, Potentialities, and Opportunities. *Journal of the American Ceramic Society*, 98(7), pp.1983-2001.
- [200] Zupancic, A., Lapasin, R. and Kristoffersson, A., 1998. Influence of particle concentration on rheological properties of aqueous α -Al₂O₃ suspensions. *Journal of the European Ceramic Society*, 18(5), pp.467-477.